



**NATIONAL TECHNICAL UNIVERSITY OF ATHENS**  
SCHOOL OF MECHANICAL ENGINEERING  
SECTION OF FLUIDS  
LABORATORY OF THERMAL TURBOMACHINES

## **Design of disks in thermal turbomachines**

Diploma Thesis  
Agapi Bakogianni

Supervisor  
Nikolaos Aretakis, Associate Professor NTUA

Athens  
October 2021



**NATIONAL TECHNICAL UNIVERSITY OF ATHENS**  
**SCHOOL OF MECHANICAL ENGINEERING**  
**SECTION OF FLUIDS**  
**LABORATORY OF THERMAL TURBOMACHINES**

**Abstract**

**Design of disks in thermal turbomachines**

This diploma thesis is concerned with the design of thermal turbomachinery disks. Design process starts from an initial disk geometry and produces a new geometry of less weight which meets all the required geometry and stress constraints. In particular, numerical tools are developed in PROOSIS useful for the optimization of a disk.

For the purpose of this thesis the geometry of NASA's/GE E3 engine is used for reference. The dimensions of the disks were extracted by the digitization of engine drawings from the bibliography. Important values about the blades were read from tables and used to calculate their weights, centers of gravity and eventually the loads exerted on the disk.

Optimization requires stress calculation in order to ensure the satisfaction of the stress criteria. Prior to stress calculation a temperature profile needs to be calculated and be put as an input to stress calculation so that the thermal stresses can be evaluated. Thus, the tools that were developed before the optimization are a temperature profile calculating function and a stress calculating function. The functions described above are based in one-dimensional models, plane stress is assumed. The stress calculating function can handle temperature gradient, if chosen to exist, isotropic and anisotropic materials and can change the material properties according to the temperature at every node. In order to validate the results, the same simulations are run using both PROOSIS functions and Solidworks three-dimensional finite element analysis (FEA). Solidworks thermal study calculates the temperature profile. Solidworks static study calculates the stresses given the loads, it is possible to import the results of a thermal study into a static study to take thermal stresses into consideration. The comparison of the temperature radial distribution can be done individually using an arbitrary turbine disk geometry. Subsequently, the verification of the stresses is done in three load cases. Load cases a and b are simulated at room temperature for the disk geometries of the three first stages of NASA's E3 engine high pressure compressor. Load case c, examines the contribution of temperature gradient and uses the same arbitrary turbine disk geometry that was used in the temperature validation. The results of the two methods have in every case sufficiently small differences. Thus, the time consuming FEA method can be replaced by the one-dimensional methods implemented in the developed PROOSIS functions. This makes these functions suitable for an optimization problem where the stresses should be calculated multiple times.

The goal of optimization is to reduce the mass with respect to the limitations and engine design variables. Therefore, it also requires a disk mass calculating function. This function

uses an analytical formula to calculate the weight by the disk geometry. The weight results are validated with Solidworks evaluation tool. The variables of the optimization are always some of the disk dimensions. The constraints consist of stress limitations and geometric limitations which frame dimensions and link them with each other. Simplex method is used for the minimization of weight. At every iteration temperature, stresses and weight calculating functions are called for the updated geometry. Since it is a method that requires only the value of the objective function, a penalty value is added to the objective function upon the violation of any constraint. The reduction of weight is equivalent to the increase of stresses, so the objective function is constructed in a way that its minimization leads to stresses maximization. The objective function is not necessarily continuous but this uses Simplex method ability to handle non-continuous functions. The optimization consists of three cases, each with its own variables and constraints, according to three bibliographical sources: Lolis, Gasturb, Armand. Each of these three methods is used for optimizing the disks of the first three stages of NASA's E3 engine high pressure compressor. Additionally, a verification with Gasturb Details 5 Software is executed. The default web disk geometry of the program was used as an initialization. The same geometry, boundary conditions, temperature distributions, variables and constraints were used at both GasTurb Details 5 and PROOSIS. The studies were run and the results were close.

## **Acknowledgements**

I would like to thank my Diploma Thesis supervisor, Associate Professor Nikolaos Aretakis, who introduced me to the field of aircraft engines which had been always fascinating me. He also provided me with a very interesting subject and consulted me and supported me throughout the whole project.

Also, I would like to express my big gratitude to Mr. Ioannis Kolias, who is currently on his PhD and was always available to offer his valuable help. He provided me with many codes that I used in my thesis and introduced me to programming in PROOSIS Software, which was new to me.

# Contents

<b>Contents</b>	<b>5</b>
1. Introduction	13
2. Disk and blades geometry description and parametrization	15
2.1 Ring Type Disk	16
2.2 Web Disk Type	17
2.3 Hyperbolic Disk Type	18
2.4 Dead weight calculation	19
3 Temperature profile calculation	23
3.1 Introduction to temperature calculation	23
3.2 Analytical solution of Fourier's law	23
3.3 Numerical solution of variable thickness expression of Fourier's law	25
3.4 Implementation in PROOSIS	28
3.5 Validation with Solidworks	30
3.5.1 Brief description of FEA thermal analysis	30
3.5.2 Solidworks solution	31
3.5.3 Comparison of the results	33
4 Stress Analysis	35
4.1 Introduction to stress analysis	35
4.2 Equations of stress analysis	36
4.3 Discretization of the analytical equations	39
4.3.1 Stresses equation	39
4.3.2 Stress Boundary Conditions	44
4.3.3 Stresses Final solution procedure	45
4.4 Stress calculation implementation in PROOSIS	48
5 Stresses validation with Solidworks	50
5.1 Introduction to stress validation	50
5.2 Brief Description of Finite Element Analysis (FEA)	50
5.3 Validation Process	51
5.3.1 Boundary conditions and formulation of load cases	51
5.3.2 Solidworks settings	53
5.3.3 Mesh Independence	54
5.3.4 Results Comparison	56
5.3.5 Conclusions	59

6. Optimization.....	61
6.1 Introduction .....	61
6.2 Mass Calculating function .....	61
6.3 Optimization problem construction .....	63
6.4 Implementation of optimization in PROOSIS .....	64
6.5 E3 HPC 1 <sup>st</sup> stage optimization .....	65
6.6 E3 HPC 2 <sup>nd</sup> stage optimization .....	67
6.6.1 Lolis approach .....	68
6.6.2 Gasturb approach.....	70
6.6.3 Armand approach .....	71
6.6.4 Table of optimization results for 2 <sup>nd</sup> stage .....	73
6.7 E3 3 <sup>rd</sup> stage optimization.....	73
6.7.1 Lolis approach .....	74
6.7.2 Gasturb approach.....	76
6.7.3 Armand approach.....	77
6.7.4 Table of optimization results for 3 <sup>rd</sup> stage.....	79
6.8 Verification with “Gasturb Details 5” .....	79
6.8.1 Stress validation .....	79
6.8.2 Optimization verification.....	80
7. Summary, conclusions and future suggestions .....	85
References .....	86
8 Εκτεταμένη περίληψη (Ελληνικά) .....	87
8.1 Εισαγωγή.....	88
8.2 Υπολογισμοί για το dead weight .....	92
8.3 Υπολογισμός θερμοκρασιακού προφίλ .....	93
8.4 Υπολογισμός των τάσεων.....	96
8.5 Πιστοποίηση των αποτελεσμάτων των τάσεων .....	99
8.6 Βελτιστοποίηση.....	105
8.6.1 Βελτιστοποίηση 1 <sup>ης</sup> βαθμίδας HPC E3 .....	107
8.6.2 Βελτιστοποίηση 2 <sup>ης</sup> βαθμίδας HPC E3 .....	109
8.6.3 Βελτιστοποίηση 3 <sup>ης</sup> βαθμίδας HPC E3 .....	111
8.7 Ανακεφαλαίωση ,συμπεράσματα και προτάσεις .....	115

# List of figures

Figure 1 : Section view o NASA/GE E3 engine HPC [4].....	13
Figure 2: This figure illustrates a web disk-blades assembly. The yellow part is the live weight of the disk and the blue one is the disk posts. The blades are the white parts and are attached to the disk by their positions between the posts [5] .....	15
Figure 3: Cross section of ring disk type. The live dead is discretized linearly into 6 radial stations. Every radial station shares the same thickness which is equal to the rim thickness. Above of the live weight there is the dead weight, from which the post and the airfoil are visible.[3].....	16
Figure 4: Web Type Disk. Starting from the bore we have successively, the inner rim, the inner shoulder, the web, the outer shoulder and the outer rim. The rims have constant thickness and the web is the thinnest part of the disk [3] .....	17
Figure 5: Hyperbolic Type Disk. Starting from the bore we have successively the constant thickness inner rim, the inner web, the outer web, the shoulder and the constant thickness outer rim. [3] .....	18
Figure 6 Blade root geometry. The blade root consists of the fir tree (blue area), the neck whose existence is optional (yellow area) and the blade platform (orange area) [5] .....	19
Figure 7: The grey part is the disk. The area $A_h$ is at every radial station the section between the disk volume and the blue cylindrical surface. The blue surface has radius equal to the radial station.....	26
Figure 8 : Temperature profile calculation function <code>calcDiskT()</code> Workflow Diagram when the numerical calculation type is chosen.....	29
Figure 9: Workflow of tridiagonal system solving function <code>AxEqB_TDMA()</code> .....	30
Figure 10: Cross section of the test disk modeled in Solidworks for the temperature validation. The dimensions are described in Table .....	31
Figure 11: Half cross section of the disk described in Table 1.....	32
Figure 12: Solidworks thermal study results. The study is described in Table 1. ....	32
Figure 13: The blue points are sensors on the thermal study test disk in order to obtain the radial temperature profile.....	32
Figure 14: Comparison of the results of Solidworks and one-dimensional analytical solution of constant thickness Fourier's heat conduction law (method described in 3.2). The studies were conducted on the disk described at Table 1.....	33
Figure 15: Comparison of the results of Solidworks and PROOSIS implementation of thickness inclusive Fourier's heat conduction law (method described in 3.3) . The studies were conducted on the disk described at Table 1. ....	33
Figure 16: Percentage differences between temperatures calculated with Solidworks and PROOSIS at the same radial stations. The two compared temperature profiles are the ones shown in Figure 13. ....	34
Figure 17 The disk is divided into elements [1] .....	35
Figure 18: The disk is radially discretized into $n$ stations; the first station is always the bore and the last station is the rim. There, the boundary conditions are applied. The discretization is executed with the use of 2 intervals $[0,1]$ and $[1,2]$ between three successive theoretical radial stations $0,1,2$ or $(i-1), i, (i+1)$ in the disk. ....	39
Figure 19: Workflow of the stress calculating function <code>calcDiskS_FV()</code> .....	49

Figure 20 : Section view of 1st stage of HPC in E3. The blue points are sensors of stress.	53
Figure 21: Section view of 2nd stage of HPC in E3. The blue points are sensors of stress.	53
Figure 22: Section view of 3rd stage of HPC in E3. The blue points are sensors of stress.	53
Figure 23 Inertial relief setting.	54
Figure 24: Mesh independence chart for stage 1 disk of HPC NASA/GE E3. Element size of 7 mm is chosen.	54
Figure 25: Mesh independence chart for stage 2 disk of HPC NASA/GE E3. Element size of 6 mm is chosen.	55
Figure 26: Mesh independence chart for stage 2 disk of HPC NASA/GE E3. Element size of 6 mm is chosen.	55
Figure 27: Stress curves comparison for NASA/GE E3 HPC ,Stage 1, Load case a): zero bore stress,zero rim stress,no temperature gradient	56
Figure 28: Stress curves comparison for NASA/GE E3 HPC, Stage 1, Load case b): zero bore stress, non-zero rim stress, no temperature gradient.	56
Figure 29: Stress curves comparison for NASA/GE E3 HPC, Stage 2, Load case a): zero bore stress,zero rim stress,no temperature gradient	57
Figure 30: Stress curves comparison for NASA/GE E3 HPC, Stage 2, Load case b): zero bore stress, non-zero rim stress, no temperature gradient.	57
Figure 31: Stress curves comparison for NASA/GE E3 HPC, Stage 3, Load case a): zero bore stress,zero rim stress,no temperature gradient	58
Figure 32: Stress curves comparison for NASA/GE E3 HPC, Stage 3, Load case b): zero bore stress, non-zero rim stress, no temperature gradient.	58
Figure 33: Comparison of the radial and tangential stresses as calculated by Solidworks and PROOSIS analyses on the disk described at Table 1 with temperature gradient, centrifugal load, rim load and zero bore load (Load case c).	59
Figure 34: Workflow of weight calculation function WKG_diskW_ARMAND_MOD.	62
Figure 35: The Workflow of optimization experiment	65
Figure 36: Stresses at the initial disk of the 1 <sup>st</sup> stage of E3 HPC. Von Mises stress calculated at 100% speed and tangential stress calculated at 120% speed , compared with their maximum limits yield strength/1.1 and 0.9*ultimate strength.	66
Figure 37: Stresses at the optimal geometry of 1st stage disk of HPC E3. It is shown that the maximum stress criterion has reached its limits.	66
Figure 38 : Convergence of the stress ratios for 1 <sup>st</sup> stage disk.	67
Figure 39: Weight convergence of the 1st stage disk.	67
Figure 40: Initial and optimum 1 <sup>st</sup> stage disk semi-contours for comparison. It is obvious that the disk weight is reduced since the bore radius is increased.	67
Figure 41: HPC E3 2nd stage initial stresses indicate that they can be further increased.	68
Figure 42: Stresses at the optimal geometry of 2 <sup>nd</sup> stage disk of HPC E3 according to Lolis. The stresses have reached their limits	69
Figure 43: Comparison of 2nd stage HPC E3 initial and optimal geometry according to Lolis. It is obvious that the new disk geometry is of lower weight.	69
Figure 44: Weight convergence for 2nd stage disk ,Lolis approach	69
Figure 45: Stress convergence for 2nd stage disk Lolis approach	69



Figure 46: Stresses at the optimal geometry of 2 <sup>nd</sup> stage disk of HPC E3 according to Gasturb. The stresses have reached their limits .....	70
Figure 47: Comparison of 2nd stage HPC E3 initial and optimal geometry according to Gasturb. It is obvious that the new disk geometry is of lower weight.....	71
Figure 48: Weight convergence for 2nd stage disk Gasturb approach .....	71
Figure 49: Stresses convergence for 2nd stage disk Gasturb approach .....	71
Figure 50: Stresses at the optimal geometry of 2 <sup>nd</sup> stage disk of HPC E3 according to Armand. The stresses have reached their limits .....	72
Figure 51: Comparison of 2nd stage HPC E3 initial and optimal geometry according to Armand. It is obvious that the new disk geometry is of lower weight.....	72
Figure 52: Weight convergence of 2nd stage disk Armand approach.....	72
Figure 53: Stresses convergence of 2nd stage disk Armand approach .....	72
Figure 54: HPC E3 3 <sup>rd</sup> stage initial stresses indicate that they can be further increased. ....	74
Figure 55: Stresses at the optimal geometry of 3 <sup>rd</sup> stage disk of HPC E3 according to Lolis. The stresses have reached their limits .....	75
Figure 56: Comparison of 3 <sup>rd</sup> stage HPC E3 initial and optimal geometry according to Lolis. It is obvious that the new disk geometry is of lower weight. ....	75
Figure 57: Weight convergence for 3rd stage disk Lolis approach.....	75
Figure 58: Weight convergence for 3rd stage disk Lolis approach.....	75
Figure 59: Stresses at the optimal geometry of 3 <sup>rd</sup> stage disk of HPC E3 according to Gasturb. The stresses have reached their limits .....	76
Figure 60: Comparison of 3 <sup>rd</sup> stage HPC E3 initial and optimal geometry according to Gasturb. It is obvious that the new disk geometry is of lower weight.....	77
Figure 61: Weight convergence for 3rd stage disk Gasturb approach .....	77
Figure 62: Stresses convergence for 3rd stage disk Gasturb approach.....	77
Figure 63: Stresses at the optimal geometry of 3 <sup>rd</sup> stage disk of HPC E3 according to Armand. The stresses have reached their limits. ....	78
Figure 64: Comparison of 3 <sup>rd</sup> stage HPC E3 initial and optimal geometry according to Armand. It is obvious that the new disk geometry is of lower weight.....	78
Figure 65: Weight convergence for 3rd stage disk Armand approach.....	78
Figure 66: Stresses convergence for 3rd stage disk Armand approach.....	78
Figure 67: Comparison of stress results from Gasturb Details 5 and PROOSIS. The disk analyzed is the Demo disk that opens with Gasturb Software as a default.....	80
Figure 68: Demo Disk semi-contour .....	81

# List of tables

Table 1: Dimensions,material and boundary conditioin of thermal study disk.....	31
Table 2 E3 Disks Information .....	50
Table 3 The load cases .....	51
Table 4 Rim stress calculations .....	51
Table 5: Load case a description.....	52
Table 6: Load case b description .....	52
Table 7: Load case c description.....	52
Table 8: The von mises stress errors(%) for every validation case.....	59
Table 9: Results of 1st stage HPC E3 optimization.....	66
Table 10 : Summarization of the results of 2 <sup>nd</sup> stage of HPC E3 optimization.....	73
Table 11 : Summarization of the results of HPC E3 3 <sup>rd</sup> stage optimization.....	79
Table 12 : Gasturb Demo disk geometry .....	80
Table 13: Demo disk rim load calculation.....	81
Table 14: comparison of optimization results from Gasturb Details 5 and PROOSIS ...	83

# Nomenclature

C	Hooke's Law stiffness coefficients
E	Elastic modulus
A	Stress coefficient
B	Stress coefficient
D	Stress coefficient
$\nu_{0r}=\nu$	Poisson's ratio
r	Radius at station
t	Disk thickness at station
z	Axial direction
T	Temperature at station
u	Radial displacement
a	Thermal expansion coefficient
$\epsilon,\gamma$	Normal and shear strains
$\rho$	Density
$\sigma,\tau$	Normal and shear stresses
$\omega$	Rotor angular velocity
$F_\theta$	Force in tangential direction
$F_r$	Force in radial direction
$\sigma_\theta$	Tangential stress
$\sigma_r$	Radial stress
k	Material thermal conductivity
$\dot{q}$	Energy generation rate per unit volume of the medium
$c_p$	Specific heat capacity
$A_h$	Area of the cross section through which the heat flows inside the disk
$Z_{1,i}$	Coefficient of $T_{i-1}$
$Z_{2,i}$	Coefficient of $T_i$

$Z_{3,i}$	Coefficient of $T_{i+1}$
$\bar{\sigma}_{r10}$	Average radial stress in interval [0,1]
$\bar{\sigma}_{r21}$	Average radial stress in interval [1,2]
$\bar{\sigma}_{\theta 10}$	Average tangential stress in interval [0,1]
$\bar{\sigma}_{\theta 21}$	Average tangential stress in interval [1,2]
$RHS$	Right hand side
$r_{root}$	Radius of the root of the airfoil
$r_{neck,o}$	Outer radius of the neck of the blade
$r_{neck,i}$	Inner radius of the neck of the blade
$r_{post,o}$	Outer radius of the post of the blade
$r_{post,i}$	Inner radius of the post of the blade
$c_{b,mean}$	Mean airfoil chord
$t_b$	Mean airfoil thickness
$m_{af}$	Airfoil mass
$r_{cg,af}$	Radius at the center of mass of the airfoil
$\rho_b$	Density of blade material
$m_{srd}$	Mass of blade shroud
$r_{cg,srd}$	Radius of the center of mass of the shroud
$h_{root}$	Height of blade root
$h_{firtree}$	Height of blade fir tree
$h_{firtree,max}$	Maximum possible height of blade fir tree
$t_{platform}$	Thickness of blade platform
$m_{platform}$	Mass of blade platform
$m_{firtree}$	Mass of blade fir tree
$m_{post}$	Mass of blade post
$m_{neck}$	Mass of blade neck
$r_{cg,platform}$	Radius at the center of mass of blade platform
$r_{cg,firtree}$	Radius at the center of mass of blade fir tree
$r_{cg,post}$	Radius at the center of mass of blade post
$r_{cg,neck}$	Radius at the center of mass of blade neck
$n_b$	Number of blades supported by the disk
$m_b$	Mass of a blade
$r_{cg}$	Radius of the center of gravity of the blades
FEM	Finite Element Method
F	Vector of forces at the boundary nodes in FEM
$K_{global}$	Global matrix of elasticity
$u_{FEM}$	Vector of DOFs/Displacements in FEM
dsf	Disk shape factor
HPC	High Pressure Compressor
LPT	Low Pressure Turbine
$\sigma_{rr}(SOLID)$	Radial stress as computed by Solidworks software
$\sigma_{tt}(SOLID)$	Tangential stress as computed by Solidworks software
$\sigma_{rr}(PROOSIS)$	Radial stress as computed by PROOSIS algorithm
$\sigma_{tt}(PROOSIS)$	Tangential stress as computed by PROOSIS algorithm
Superscripts and subscripts	
b	blade or dead weight
cg	center of gravity

m	mechanical stress component
T	thermal stress component
r	radial direction
$\theta$	tangential direction
bore	Bore station, the live disk station nearest to the axis of revolution
rim	Rim station, the live disk station farthest from the axis of revolution
0	First station of three point discretization
1	Second station of three point discretization
2	Third station of three point discretization

# 1. Introduction

The disks of a thermal turbomachine are vital components because they support the rotating blades and connect them to the shaft. After the design of the blades an equally efficient and reliable design of the disks should follow. The mechanical endurance of the disks especially at the high temperature environment of the turbine is crucial. Figure 1 illustrates a section view of the High-Pressure Compressor of NASA/GE E3 engine where the disks, their geometry and connection can be seen:

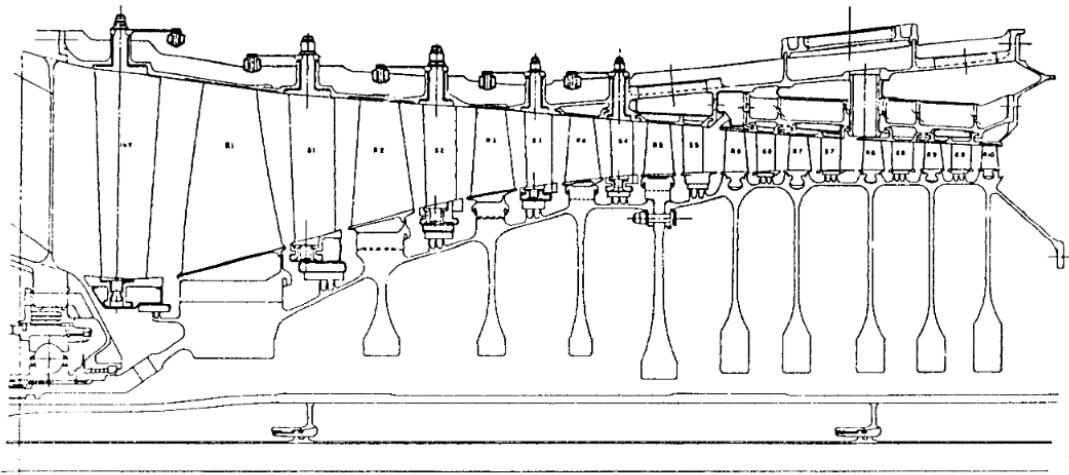


Figure 1 : Section view o NASA/GE E3 engine HPC [4]

Many researchers have engaged in the design and optimization of thermal turbomachine disks.

Lolis does not develop a method for temperature calculation and uses an empirical curve for the radial temperature distribution. Stress calculations are based on in-plane stress analysis. The disk geometry is fully defined by the radii and thicknesses in six radial stations. Stress criteria are limits upon the Von Mises stress and the average tangential stress of the disk. Additional constraints are the geometrical ones. Disk dimension correlations are applied to lower the number of design variables. For ring type disks, the design variable is one, so Newton-Raphson method is used for optimization. For the two other cases, web and hyperbolic type, 4 design variables are used and the optimization method is a gradient-based non-linear sequential quadratic. [9]

Joachim Kurzke has developed a Software called “Gasturb Details 5” in which an initial disk geometry can be inserted and optimized. The temperature radial distribution is considered linear and the stresses are calculated based on in plane models. The stress criteria involve the Von Mises stress and average tangential stress and are user defined. The users can also choose the design variables and the value that they want minimized or maximized. Two methods can be used for optimization, an adaptive random method

search strategy or a gradient based method. There are correlations between the disk dimensions, which should be valid in the initial geometry as well as the optimal.[5]

Armand calculates the stresses using in plane stress analysis. The radial temperature distribution is modeled by an up to 5<sup>th</sup> degree polynomial, the coefficients of which are user defined. His method does not apply correlations between the dimensions and thus uses more variables than the previous methods. The geometrical constraints are also very simple since they only require the radii at six radial stations to be in an ascending order. The constricted stresses are the same as in the previously described methods. The used optimization method is the sequence of unconstrained minimizations technique (SUMT) [1].

In the Tong approach in plane stress modeling is used as well. The resulting differential equations for the stresses are solved by a self-adaptive numerical iteration scheme. At every iteration, the step size is self-adjusted (increases or decreases) based on the differences in the design margin between the current and previous iterations. The design margin is based on the stress criteria which are considered the same as in the previous methods. The temperature distribution is calculated by the analytical solution of one-dimensional Fourier's law assuming constant disk thickness.[3]

Gutzwiller implements an in-plane stress modeling which handles anisotropic materials as well as isotropic. The average tangential stress is limited. The weight optimization is executed by a genetic algorithm [2].

In this thesis, the temperature radial distribution is calculated by the solution of the disk thickness inclusive one-dimensional Fourier heat conduction law. The temperature profile results match with the FEA thermal analysis results. The stress calculation process is the same as in [2] since this method includes anisotropic materials. The stress results are also validated by comparison with FEA results. Three cases of optimization were examined and their results were presented, each one with its own variables and geometrical constraints according to Lolis, Gasturb and Armand respectively. Stress criteria are common in all the three cases. Von Mises stress and the average tangential stress are constrained. The optimization method is the Nelder-Mead Simplex.

## 2. Disk and blades geometry description and parametrization

The disk-blades assembly can be divided into two sections according to their functionality, the live weight and the dead weight. The live weight is the part that is considered to offer support to the dead weight and therefore is structurally examined in this thesis. It is loaded by its own centrifugal loads and the ones of the dead weight. The dead weight comprises of the disk posts and the blades. The posts are the part of the disk that offers connection with the blades. The live weight can take different shapes, there are three main types of shapes used in the bibliography: ring type, web type and hyperbolic type. In HPC of E3 engine the first stage disk is ring type, the second hyperbolic type and the third web type. Figure 2 illustrates the assembly of the blades to a web type disk and the dividing line between the live and dead weight. The yellow part is the live weight of the disk, the blue parts are the posts and the white parts are the blades. The connection between the disk and the blades is loose, there is also a cavity between the blade and the rim radius of the disk. Attachment is accomplished by the two complementary shapes of the blade root and the post of the disk, which restrict the movement of the blade in the radial direction.

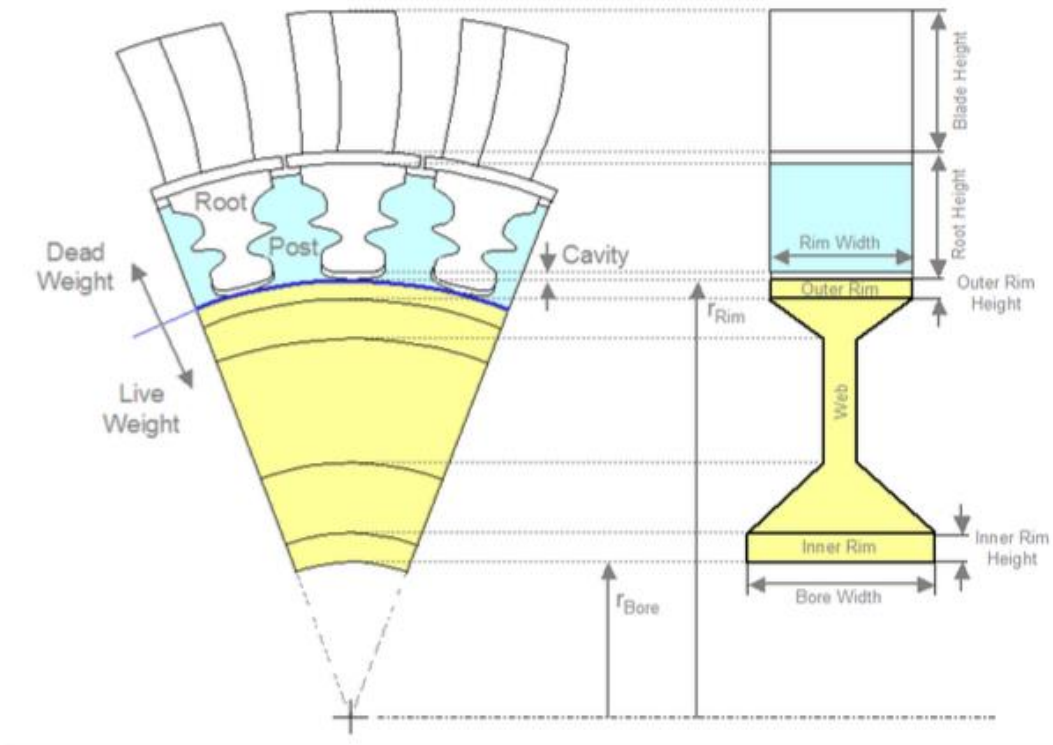


Figure 2: This figure illustrates a web disk-blades assembly. The yellow part is the live weight of the disk and the blue one is the disk posts. The blades are the white parts and are attached to the disk by their positions between the posts [5]

All the disk types are configured with six radial stations measured from the axis of revolution

$$r_1, r_2, r_3, r_4, r_5, r_6$$

and six thicknesses at the same stations

$$t_1, t_2, t_3, t_4, t_5, t_6$$

## 2.1 Ring Type Disk

The ring type geometry can be fully described with two radial stations ( $r_{bore}$ ,  $r_{rim}$ ) and one thickness variable ( $t_{rim}$ ) which is considered constant throughout the disk. We choose to express the ring geometry the same way as other disk types for consistency, therefore it should be applied that:

$$t_1 = t_2 = t_3 = t_4 = t_5 = t_6 = t_{rim}$$

$$r_1 = r_{bore}, r_6 = r_{rim}$$

$$r_i = r_1 + (i - 1) \cdot \frac{r_6 - r_1}{5} \text{ for } i = 1, \dots, 6$$

The radii are linearly distributed. Figure 3 illustrates a typical sketch of a ring type cross section.

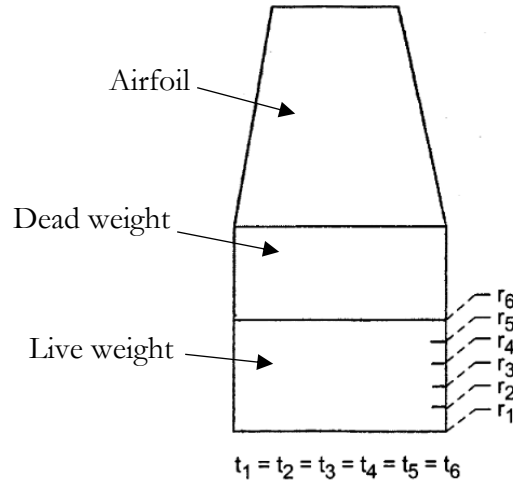


Figure 3: Cross section of ring disk type. The live dead is discretized linearly into 6 radial stations. Every radial station shares the same thickness which is equal to the rim thickness. Above of the live weight there is the dead weight, from which the post and the airfoil are visible.[3]



## 2.2 Web Disk Type

Web disk type geometry is illustrated in Figure 4. Starting from the bore, between radial stations 1 and 2 is the inner rim part which has constant thickness, between 2 and 3 is the inner shoulder, between 3 and 4 lies the web which is the thinnest part of the disk. Between stations 4 and 5 is the outer shoulder and finally the constant thickness outer rim at stations 5-6. Generally, the following are applied:

$$t_1 = t_2, t_3 = t_4, t_5 = t_6$$

$$t_3 < t_2, t_4 < t_5$$

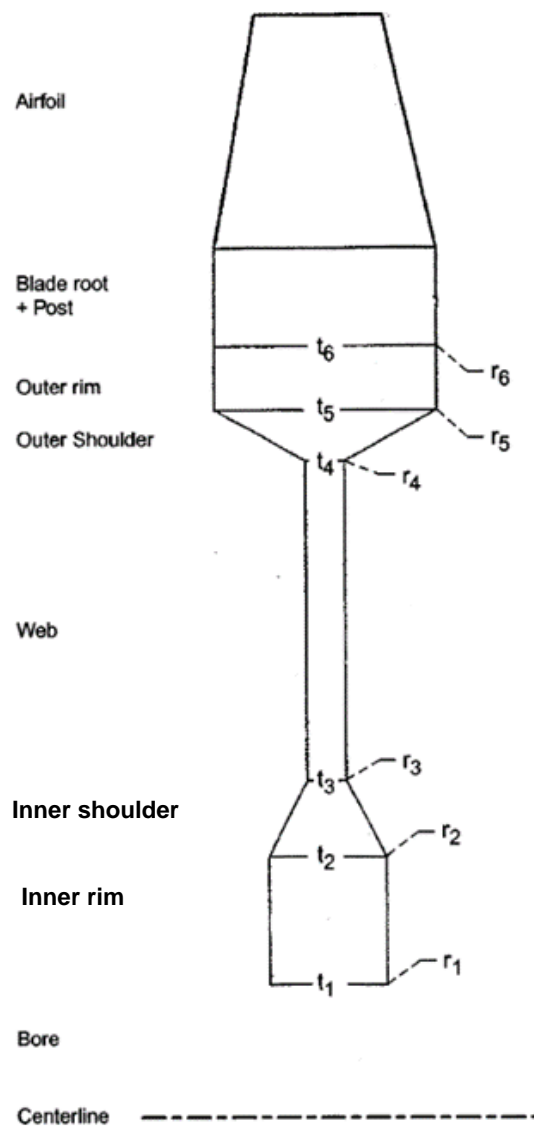


Figure 4: Web Type Disk. Starting from the bore we have successively, the inner rim, the inner shoulder, the web, the outer shoulder and the outer rim. The rims have constant thickness and the web is the thinnest part of the disk [3]

## 2.3 Hyperbolic Disk Type

Figure 5 illustrates a cross section of a hyperbolic disk. Starting from the bore we meet successively the constant thickness inner rim, the inner web, the outer web, the shoulder and the constant thickness outer rim. The hyperbolic geometry differs from the web one between the radial stations 2 and 3 where the inner shoulder is replaced by a curved convergent geometry called inner web. In that space the contour is described by the following equation where the thickness at any point  $i$  between 2-3 is expressed with its radial distance [2]:

$$t_i = t_2 + (t_3 - t_2) \left( \frac{r_i - r_2}{r_3 - r_2} \right)^{dsf}$$

Where  $dsf < 1$  is the disk shape factor and is user defined. If taken equal to 1 the relation is linear.

The following relations apply for the hyperbolic type:

$$t_1 = t_2, t_5 = t_6$$

$$t_3 < t_2, t_4 < t_5$$

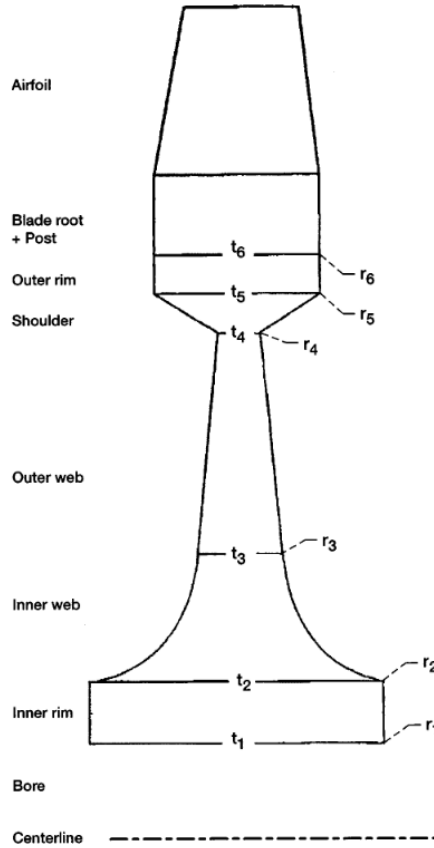


Figure 5: Hyperbolic Type Disk. Starting from the bore we have successively the constant thickness inner rim, the inner web, the outer web, the shoulder and the constant thickness outer rim. [3]

## 2.4 Dead weight calculation

In this subchapter useful formulas for the disk rim load calculation are stated. In particular, starting from the airfoil main dimensions and the disk rim radius, the mass and center of gravity of the disk dead weight can be found. Consequently, the rim load is equal to the centrifugal force of the dead weight.

The whole blade comprises of the airfoil and the blade root.

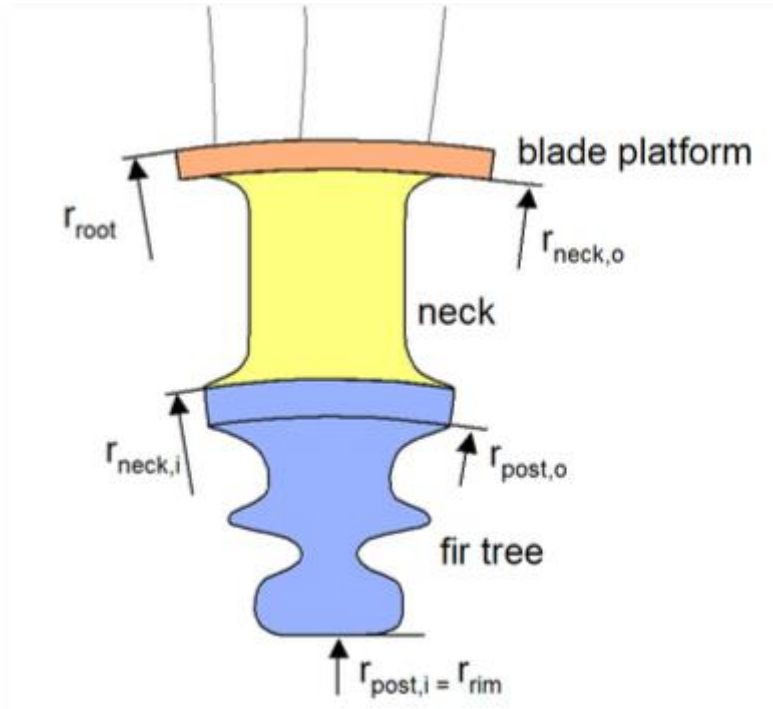


Figure 6 Blade root geometry. The blade root consists of the fir tree (blue area), the neck whose existence is optional (yellow area) and the blade platform (orange area) [5]

The airfoils masses are calculated according to [5]:

The axial cord is equal to the rim width  $t_{rim}$ . Mean blade chord is:

$$c_{b,mean} = \frac{t_{rim}}{\cos(a_{stagger})}$$

The mean blade material thickness is:

$$t_b = c_{b,mean} \cdot \left(\frac{t}{c}\right)_{b,mean}$$

The mass of one airfoil is:

$$m_{af} = \rho_b \cdot (r_{tip} - r_{root}) \cdot t_b \cdot c_{b,mean}$$

The center of gravity is not in the middle radius because of the blade taper. It is:

$$r_{cg,af} = 0.4r_{tip} + 0.6r_{root}$$

If there are blade shrouds, it is assumed that their thickness is 5% of  $t_{rim}$ . Their mass is:

$$m_{srd} = \rho_b \cdot 0.05 \cdot t_{rim}^2 \cdot \frac{2\pi r_{b,tip}}{n_b}$$

The center of gravity of the shroud is at the radius:

$$r_{cg,srd} = r_{tip} + 0.05t_{rim}$$

The formula above takes into consideration the tip fences, the shroud is not a simple plate.

Blade root masses and post masses are calculated as described below [5].

The blade root includes the blade platform, the neck and the fir tree. The neck exists only if the total height of the blade root is bigger than the sum of blade platform thickness and the fir tree height. The total height of the blade root is:

$$h_{root} = r_{root} - r_{rim}$$

The blade platform thickness is taken as 5% of the rim width

$$t_{platform} = 0.05t_{rim}$$

The fir tree height is:

$$h_{fir\ tree} = r_{neck,i} - r_{rim}$$

Also,  $h_{fir\ tree}$  should not be greater than the blade platform width. Thus:

$$h_{fir\ tree,max} = \frac{2\pi r_{root}}{n_b}$$

The inner radius of the neck is written:

$$r_{neck,i} = r_{rim} + h_{fir\ tree,max}$$

If  $r_{neck,i} > r_{root} - t_{platform}$  then neck does not exist and we set:

$$r_{neck,i} = r_{root} - t_{platform}$$

Then:

$$h_{fir\ tree} = r_{root} - t_{platform} - r_{rim}$$

After parametrizing the geometry of the blade, we can calculate masses. The mass of the blade platform is:

$$m_{platform} = \rho_b \cdot 0.05 \cdot t_{rim}^2 \cdot \frac{2\pi r_{root}}{n_b}$$

The fir tree mass is:

$$m_{firtree} = \frac{\rho_b t_{rim} \pi (r_{neck,i}^2 - r_{rim}^2)}{2n_b}$$

The posts extend to radius  $r_{post,o}$  which is:

$$r_{post,o} = r_{rim} + 0.8(r_{neck,i} - r_{rim})$$

Then the mass of the post is:

$$m_{post} = \frac{\rho t_{rim} \pi (r_{post,o}^2 - r_{rim}^2)}{2n_b}$$

If neck exists it is assumed that its thickness is twice the thickness of the blade. Its mass is:

$$m_{neck} = 2\rho_b t_b t_{rim} (r_{neck,o} - r_{neck,i})$$

The centers of gravity of the platform, fir tree, post and neck are assumed to be at their respective mean radii:

$$r_{cg,platform} = \frac{r_{root} + r_{neck,o}}{2}$$

$$r_{cg,firtree} = \frac{r_{neck,i} + r_{rim}}{2}$$

$$r_{cg,post} = \frac{r_{post,o} + r_{rim}}{2}$$

$$r_{cg,neck} = \frac{r_{neck,o} + r_{neck,i}}{2}$$

The total dead mass per blade is:

$$m_b = m_{af} + m_{srd} + m_{platform} + m_{neck} + m_{firtree} + m_{post} \quad (1)$$

The radius of center of mass of the total dead weight is calculated as:

$$r_{cg} = (m_{af} r_{cg,af} + m_{srd} r_{cg,shr} + m_{platform} r_{cg,platform} + m_{neck} r_{cg,neck} + m_{firtree} r_{cg,firtree} + m_{post} r_{cg,post}) / m_b \quad (2)$$

The rim stresses are calculated according to:

$$\sigma_{r,rim} = \frac{n_b m_b r_{cg}}{2\pi r_{rim} t_{rim}} \omega^2 \quad (3)$$

## 3 Temperature profile calculation

### 3.1 Introduction to temperature calculation

In this chapter, two methods for the temperature profile calculation are described. The first is a one-dimensional analytical solution of Fourier's heat conduction law which takes into account only the radial distance and assumes constant disk thickness. This method is considered by some investigators for simplicity, see [3]. The second is the numerical solution of another expression of Fourier's law which takes into account the area through which heat flows and thus the variation of disk thickness at every radius. After the implementation in PROOSIS and the comparison of both method results with Solidworks FEA it can be concluded that the second numerical solution gives a temperature curve form close to reality and very accurate results.

### 3.2 Analytical solution of Fourier's law

The general form of heat conduction law in cylindrical coordinates is [6]:

$$\frac{\partial^2 T}{\partial r^2} + \frac{1}{r} \frac{\partial T}{\partial r} + \frac{1}{r^2} \frac{\partial^2 T}{\partial \theta^2} + \frac{\partial^2 T}{\partial z^2} + \frac{\dot{q}}{k} = \frac{\rho c_p}{k} \frac{\partial T}{\partial t} \quad (4)$$

The problem is axisymmetric and steady. Therefore, we consider  $\frac{\partial T}{\partial \theta} = 0$ ,  $\frac{\partial T}{\partial t} = 0$  respectively. Since there is no heat generated inside the disk, we have  $\dot{q} = 0$ .

If the problem is considered one dimensional it also applies that:  $\frac{\partial T}{\partial z} = 0$ . Then equation (4) can be written:

$$\frac{d^2 T}{dr^2} + \frac{1}{r} \frac{dT}{dr} = 0 \quad (5)$$

For casting equation (5) into a non-dimensional form we set:

$$T^* = \frac{T}{T_{rim}}, \quad r^* = \frac{r}{r_{rim}} \quad (6)$$

Then:

$$\frac{dT}{dr} = \frac{d(T_{max} T^*)}{d(r_{rim} r^*)} = \frac{T_{max}}{r_{rim}} \frac{dT^*}{dr^*} \quad (7)$$

$$\frac{d^2 T}{dr^2} = \frac{d}{dr} \left( \frac{dT}{dr} \right) = \frac{d}{d(r_{rim} r^*)} \left( \frac{T_{max}}{r_{rim}} \frac{dT^*}{dr^*} \right) = \frac{T_{max}}{r_{rim}^2} \frac{d^2 T^*}{dr^{*2}} \quad (8)$$

Substituting (6),(7) and (8) into (5) we get:

$$\frac{T_{max}}{r_{rim}^2} \frac{d^2 T^*}{dr^{*2}} + \frac{1}{r_{rim} r^*} \frac{T_{max}}{r_{rim}} \frac{dT^*}{dr^*} = 0 \Rightarrow$$

$$\frac{T_{max}}{r_{rim}^2} \frac{d^2 T^*}{dr^{*2}} + \frac{1}{r^*} \frac{T_{max}}{r_{rim}^2} \frac{dT^*}{dr^*} = 0 \Rightarrow \quad (9)$$

$$\frac{d^2 T^*}{dr^{*2}} + \frac{1}{r^*} \frac{dT^*}{dr^*} = 0$$

We conclude that the undimensioned equation is the same as the initial one.

Equation (5) if multiplied by  $r^2$  is converted into:

$$r^2 \frac{d^2 T}{dr^2} + r \frac{dT}{dr} = 0 \quad (10)$$

Equation (10) is a Cauchy-Euler type differential equation, so we set  $r = e^s, s = \ln r$

Thus:

$$\frac{dT}{dr} = \frac{dT}{ds} \frac{ds}{dr} = \frac{dT}{ds} \frac{1}{r}$$

$$\begin{aligned} \frac{d^2 T}{dr^2} &= \frac{d}{dr} \left( \frac{dT}{ds} \frac{1}{r} \right) = \frac{d}{ds} \left( \frac{dT}{ds} \frac{1}{r} \right) \frac{ds}{dr} = \frac{d}{ds} \left( \frac{dT}{ds} e^{-s} \right) \frac{ds}{dr} = \\ &= \left( \frac{d^2 T}{ds^2} e^{-s} - \frac{dT}{ds} e^{-s} \right) \frac{1}{r} = \left( \frac{d^2 T}{ds^2} - \frac{dT}{ds} \right) \frac{1}{r^2} \end{aligned}$$

Substituting in (10) gives:

$$r^2 \left( \frac{d^2 T}{ds^2} - \frac{dT}{ds} \right) \frac{1}{r^2} + r \frac{dT}{ds} \frac{1}{r} = 0$$

$$\frac{d^2 T}{ds^2} - \frac{dT}{ds} + \frac{dT}{ds} = 0$$

$$\frac{d^2 T}{ds^2} = 0 \Rightarrow$$

$$T = c_1 s + c_2 \Rightarrow$$

$$T(r) = c_1 \ln r + c_2 \quad (11)$$



Similarly:

$$T^*(r) = c_1 \ln r^* + c_2 \quad (12)$$

We apply the boundary conditions:

$$\begin{aligned} r_{rim}^* = \frac{r_{rim}}{r_{rim}} = 1, \quad T_{rim}^* = \frac{T_{rim}}{T_{rim}} = 1 \\ T_{rim}^* = c_1 \ln r_{rim}^* + c_2 \Rightarrow c_2 = 1 \end{aligned} \quad (13)$$

$$\begin{aligned} r_{bore}^* = \frac{r_{bore}}{r_{rim}}, \quad T_{bore}^* = \frac{T_{bore}}{T_{rim}} \\ c_1 \ln r_{bore}^* + 1 = T_{bore}^* \Rightarrow c_1 = \frac{\frac{T_{bore}}{T_{rim}} - 1}{\ln r_{bore} - \ln r_{rim}} \end{aligned} \quad (14)$$

Substituting (13) and (14) in (12) gives the analytical expression of the temperature radial distribution for the one-dimensional heat conduction:

$$T^*(r^*) = \frac{\frac{T_{bore}}{T_{rim}} - 1}{\ln r_{bore} - \ln r_{rim}} \ln r^* + 1 \quad (15)$$

Or

$$T(r) = \frac{T_{bore} - T_{rim}}{\ln r_{bore} - \ln r_{rim}} \ln \frac{r}{r_{rim}} + T_{rim} \quad (16)$$

### 3.3 Numerical solution of variable thickness inclusive Fourier's law

The distribution expressed in equation (16) does not take into account the thickness of the disk at every radial station. In order to do that we should use an alternative form of Fourier heat conduction law in cylindrical coordinates [7]:

$$\frac{1}{A_h} \frac{\partial}{\partial r} \left( k A_h \frac{\partial T}{\partial r} \right) + \dot{q} = \rho c_p \frac{\partial T}{\partial t} \quad (17)$$

Where  $A_h$  , is the area through which the heat flows at every radial station. This area is at every radial station the cross section of the disk with a cylindrical surface of the same radius as the station. Figure 7 illustrates area  $A_h$ .

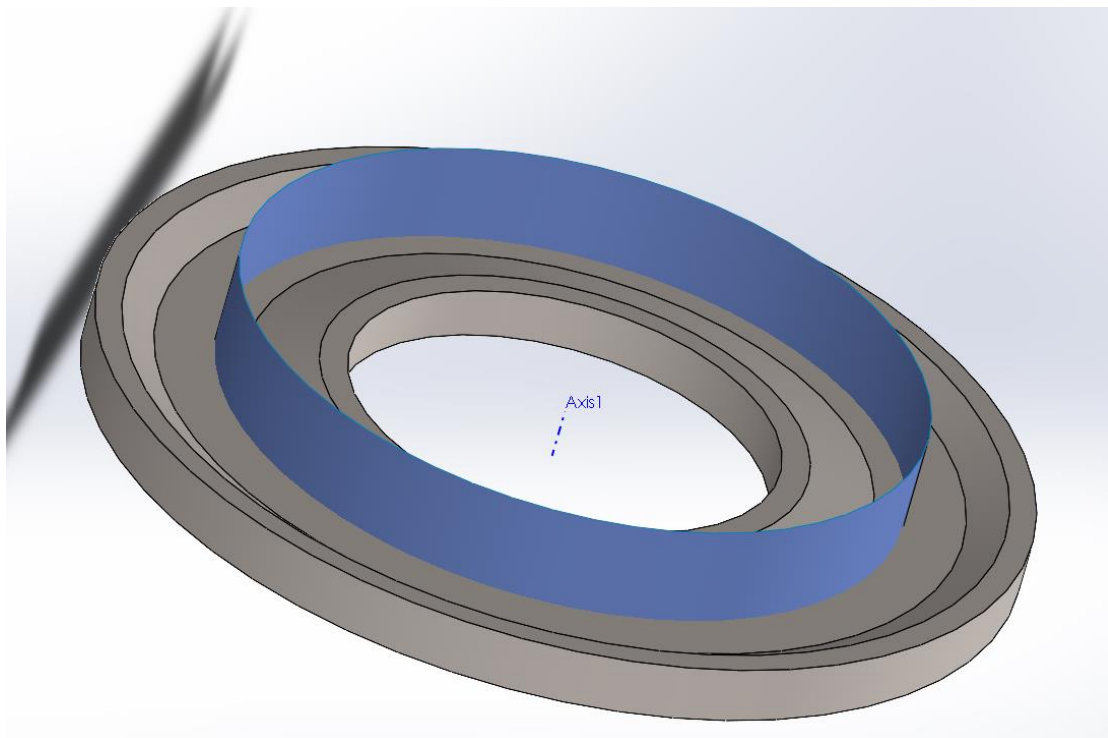


Figure 7: The grey part is the disk. The area  $A_h$  is at every radial station the section between the disk volume and the blue cylindrical surface. The blue surface has radius equal to the radial station.

For a steady state problem and no heat generation equation (17) turns into:

$$\begin{aligned} \frac{1}{A_h} \frac{d}{dr} \left( k A_h \frac{dT}{dr} \right) &= 0 \\ \frac{k}{A_h} \left( \frac{dA_h}{dr} \frac{dT}{dr} + A_h \frac{d^2T}{dr^2} \right) &= 0 \\ \frac{d^2T}{dr^2} + \frac{1}{A_h} \frac{dA_h}{dr} \frac{dT}{dr} &= 0 \end{aligned} \tag{18}$$

Equation (18) is second order differential equation which is solved numerically. For this reason, Eq. (18) is discretized using a finite difference scheme, where all derivatives are discretized using second order central differences, Equations (19)-(21):

$$\left. \frac{dT}{dr} \right|_i = \frac{T_{i+1} - T_{i-1}}{2\Delta r} + O(\Delta r^2) \tag{19}$$

$$\left. \frac{d^2 T}{dr^2} \right|_i = \frac{T_{i-1} - 2T_i + T_{i+1}}{\Delta r^2} + O(\Delta r^2) \quad (20)$$

$$\left. \frac{dA_h}{dr} \right|_i = \frac{A_{h,i+1} - A_{h,i-1}}{2\Delta r} + O(\Delta r^2) \quad (21)$$

The area through which the heat flows is cylindrical and is calculated as:

$$A_{h,i} = 2\pi r_i t_i \quad (22)$$

Substituting:

$$\begin{aligned} \frac{T_{i-1} - 2T_i + T_{i+1}}{\Delta r^2} + \frac{1}{2\pi r_i t_i} \frac{A_{h,i+1} - A_{h,i-1}}{2\Delta r} \frac{T_{i+1} - T_{i-1}}{2\Delta r} &= 0 \\ \left( \frac{1}{\Delta r^2} - \frac{1}{2\pi r_i t_i} \frac{A_{h,i+1} - A_{h,i-1}}{4\Delta r^2} \right) T_{i-1} - \frac{2}{\Delta r^2} T_i & \\ + \left( \frac{1}{\Delta r^2} + \frac{1}{2\pi r_i t_i} \frac{A_{h,i+1} - A_{h,i-1}}{4\Delta r^2} \right) T_{i+1} &= 0 \\ Z_{1,i} T_{i-1} + Z_{2,i} T_i + Z_{3,i} T_{i+1} &= 0 \end{aligned} \quad (23)$$

Where the coefficients of the temperatures are:

$$\begin{aligned} Z_{1,i} &= \frac{1}{\Delta r^2} - \frac{1}{2\pi r_i t_i} \frac{A_{h,i+1} - A_{h,i-1}}{4\Delta r^2} \\ Z_{2,i} &= -\frac{2}{\Delta r^2} \\ Z_{3,i} &= \frac{1}{\Delta r^2} + \frac{1}{2\pi r_i t_i} \frac{A_{h,i+1} - A_{h,i-1}}{4\Delta r^2} \end{aligned} \quad (24)$$

The boundary conditions are:

$$T_1 = T_{bore}$$

$$T_n = T_{rim}$$

Using the temperature coefficients, a square matrix (nxn) can be constructed and a linear system of equations is formed in Equation (25). The system is of tridiagonal form and it is solved by elimination of sub-diagonal vector and successive backward substitution. [10]

$$\begin{bmatrix}
1 & 0 & 0 & 0 & 0 & 0 & 0 \\
Z_{1,2} & Z_{2,2} & Z_{3,2} & 0 & 0 & 0 & 0 \\
0 & Z_{1,3} & Z_{2,3} & Z_{3,3} & 0 & 0 & 0 \\
0 & 0 & \dots & \dots & \dots & 0 & 0 \\
0 & 0 & 0 & Z_{1,n-2} & Z_{2,n-2} & Z_{3,n-2} & 0 \\
0 & 0 & 0 & 0 & Z_{1,n-1} & Z_{2,n-1} & Z_{3,n-1} \\
0 & 0 & 0 & 0 & 0 & 0 & 1
\end{bmatrix}
\begin{bmatrix}
T_1 \\
T_2 \\
T_3 \\
\vdots \\
T_{n-2} \\
T_{n-1} \\
T_n
\end{bmatrix}
=
\begin{bmatrix}
T_{bore} \\
0 \\
0 \\
\vdots \\
0 \\
0 \\
T_{rim}
\end{bmatrix}
\quad (25)$$

The solution of the system is the vector of the temperatures at every radial station. The temperatures are independent from the stresses, so they can be calculated prior to stress analysis and then be used for the calculation of the stresses.

### 3.4 Implementation in PROOSIS

The temperature profile calculation is implemented in PROOSIS with the function `calcDiskT()`

The arguments of the function are:

<b>istg:</b>	The number of the stage. It is used for naming the file with the results
<b>compINSTANCE_NAME:</b>	The name of the engine. It is used for naming the file with the results
<b>iswitch:</b>	The temperature distribution type option. By changing this option the temperature profile can be calculated either by the one dimensional method described in 2.2 or by the method described in 2.3 or be considered constant and equal to the rim or room temperature or even be put already calculated as an input from a source.
<b>Nd:</b>	The number of nodes
<b>Rroot:</b>	The blade airfoil root radius
<b>Troot:</b>	The blade airfoil root temperature
<b>R[Nd]:</b>	The array of the discretized radius of the disk
<b>t[Nd]:</b>	The array of the discretized thickness of the disk

<b>Trim:</b>	The boundary rim temperature
<b>TbRTrPct_in:</b>	The ratio $(T_{\text{bore}}/T_{\text{rim}})*100$
<b>T_in[Nd]:</b>	The array of the input temperature distribution, if any
<b>printFuncRpts:</b>	Is a Boolean variable. If it is TRUE it prints the results into a file

The outputs of the function is:

<b>T[Nd]:</b>	The array of the temperatures calculated in every radial station.
---------------	---

In Figure 8 the workflow of `calcDiskT()` is illustrated for the most complex and accurate case, the numerical solution of Fourier's law

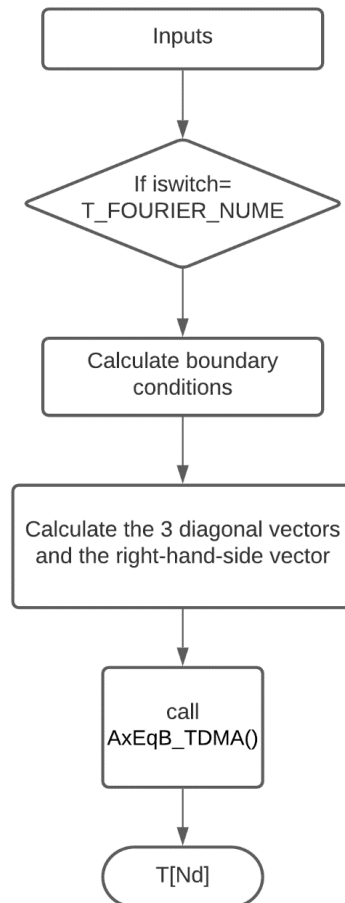


Figure 8 : Temperature profile calculation function `calcDiskT()` Workflow Diagram when the numerical calculation type is chosen

The function `AxEqB_TDMA` is called to solve the tridiagonal system. For this function the inputs are:

**N** : System Dimension  
**AV[N]**: System diagonal vector  
**BV[N]**: System sub-diagonal vector  
**CV[N]**: System super-diagonal vector  
**FV[N]**: System right-hand-side vector

The output is the solution **T[Nd]**

The workflow of `AxEqB_TDMA` is illustrated in Figure 9

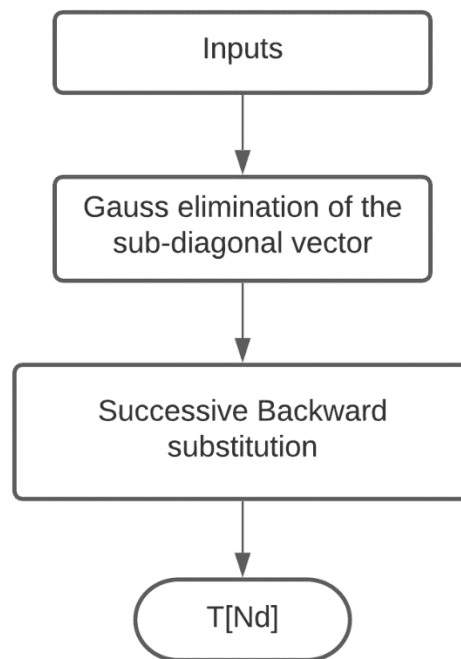


Figure 9: Workflow of tridiagonal system solving function `AxEqB_TDMA()`

## 3.5 Validation with Solidworks

### 3.5.1 Brief description of FEA thermal analysis

Solidworks provides a three-dimensional thermal analysis with FEA. the part is divided (meshed) into tetrahedrons. For a steady state heat conduction simulation, each of the 4 tetrahedron nodes has its own temperature which is unknown. All the unknowns are collected inside the **T** vector. Also, each element has a known conductivity matrix  $K_{cond}$  formed by the heat conduction properties of the material. If conductivity matrices of all elements are combined properly, with respect to the common nodes between bordering

elements, a global matrix of conductivity is formed. Vector  $f$  is calculated from the boundary conditions. The solution of the equation below gives the full temperature distribution:

$$[f] = [K_{cond}] \cdot [T]$$

### 3.5.2 Solidworks solution

For the validation of the temperature profile a test turbine disk of arbitrary geometry is modeled in Solidworks as shown in Figure 10: Cross section of the test disk modeled in Solidworks for the temperature validation. The dimensions are described in TableFigure 10.

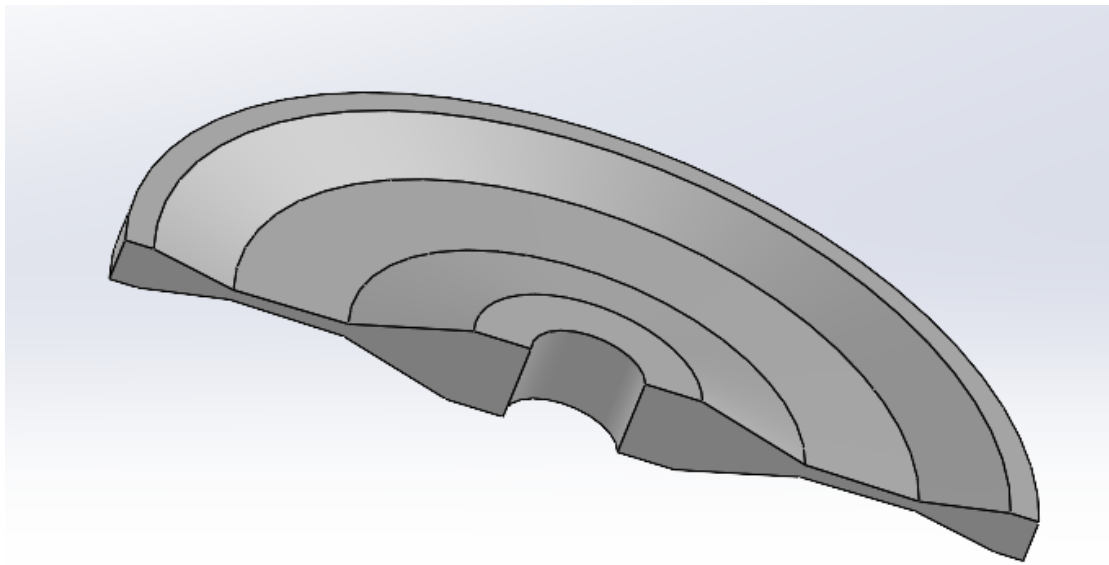


Figure 10: Cross section of the test disk modeled in Solidworks for the temperature validation. The dimensions are described in Table 1

The dimensions, material and boundary conditions are summarized in Table 1

Station	1	2	3	4	5	6
R (m)	0.05	0.1	0.2	0.3	0.375	0.4
t (m)	0.07	0.0225	0.0125	0.01	0.04	0.04
Material	INCONEL 718					
T <sub>bore</sub> (K)	398.15					
T <sub>rim</sub> (K)	823.15					

Table 1: Dimensions,material and boundary condition of thermal study disk.

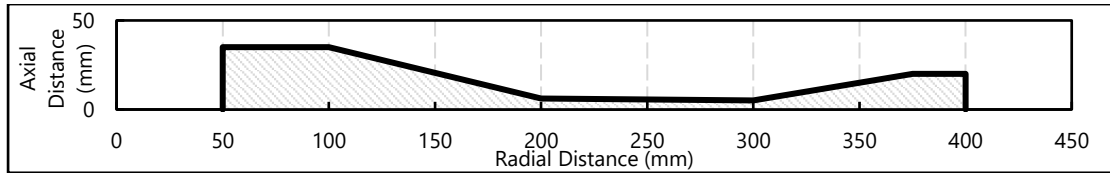


Figure 11: Half cross section of the disk described in Table 1

The results of Solidworks are shown in Figure 12:

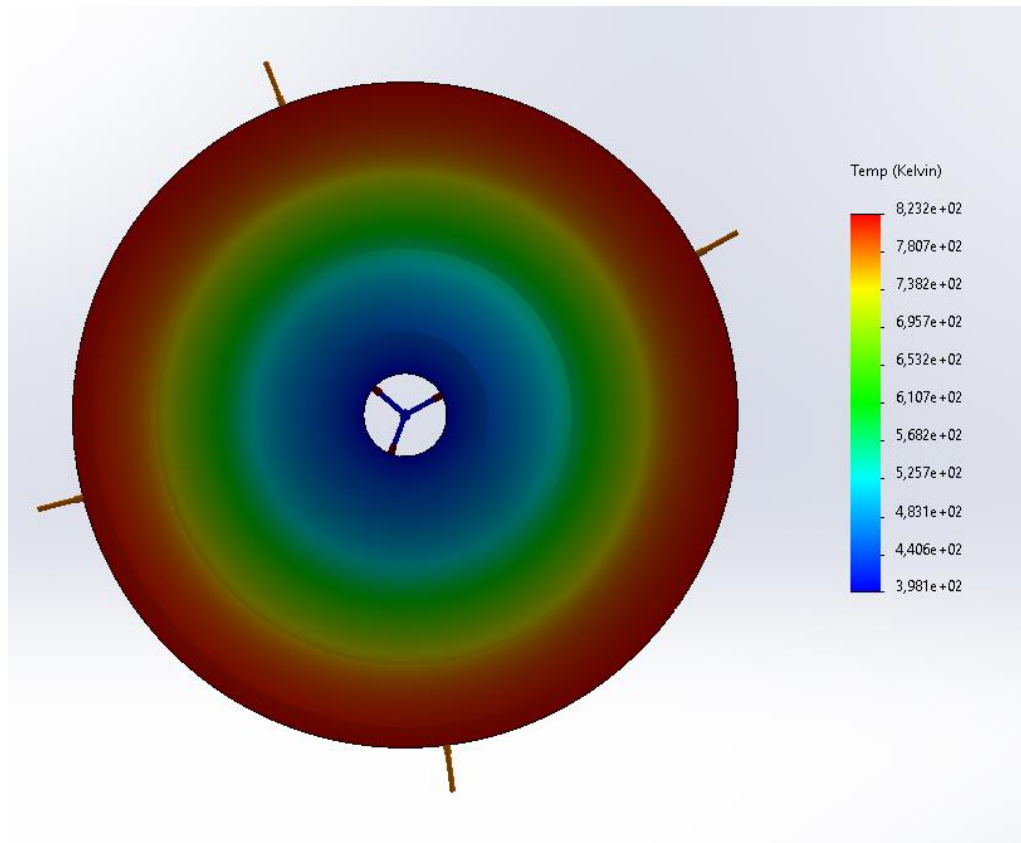


Figure 12: Solidworks thermal study results. The study is described in Table 1.

Sensors of temperature were put radially at the center plane of the disk in order to obtain a radial profile from Solidworks.



Figure 13: The blue points are sensors on the thermal study test disk in order to obtain the radial temperature profile.



### 3.5.3 Comparison of the results

The results of the two methods described in 3.2 and 3.3 are compared with Solidworks results for validation. Figure 14 compares the analytical one-dimensional solution with the solution of Solidworks. Figure 15 compares the numerical thickness inclusive solution with the Solidworks one.

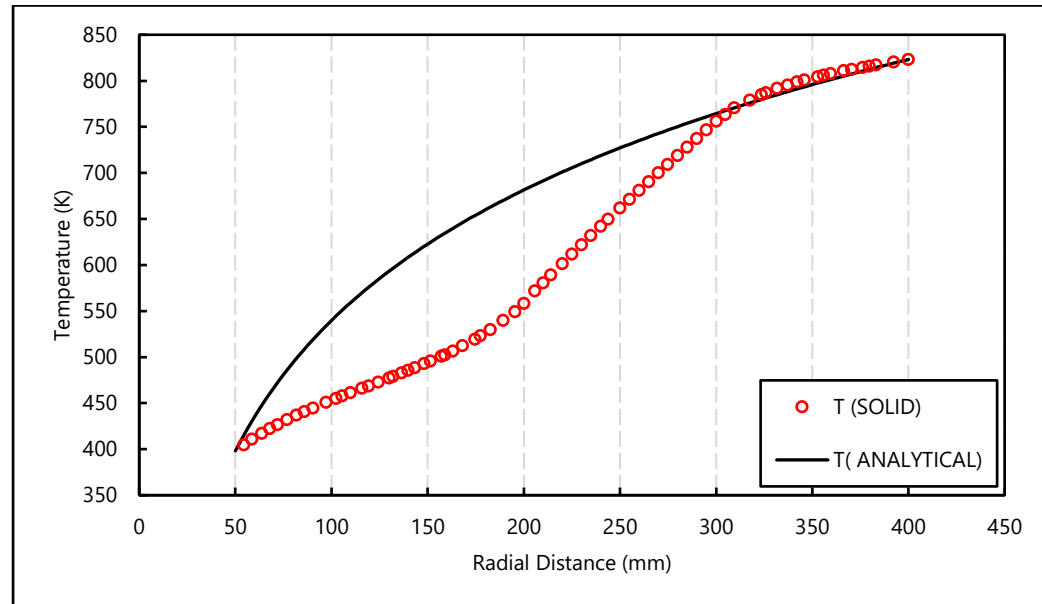


Figure 14: Comparison of the results of Solidworks and one-dimensional analytical solution of constant thickness Fourier's heat conduction law (method described in 3.2). The studies were conducted on the disk described at Table 1.

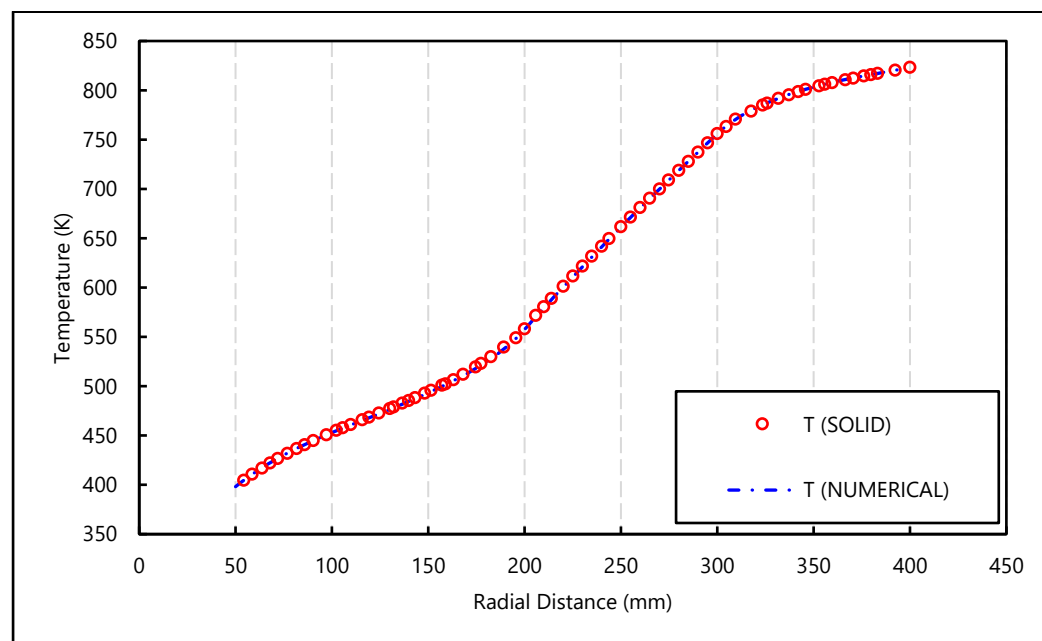


Figure 15: Comparison of the results of Solidworks and PROOSIS implementation of thickness inclusive Fourier's heat conduction law (method described in 3.3). The studies were conducted on the disk described at Table 1.

Solidworks sensor points do not match the program nodes. Therefore, in order to calculate the percentage differences between the PROOSIS and Solidworks solution, a simple script is written in MATLAB for the interpolation of Solidworks results and errors calculation. At the same radial positions the error is calculated as:

$$T_{error}(\%) = \frac{T_{solid,interpolated} - T_{proosis}}{T_{proosis}} \cdot 100$$

The results are shown in Figure 16:

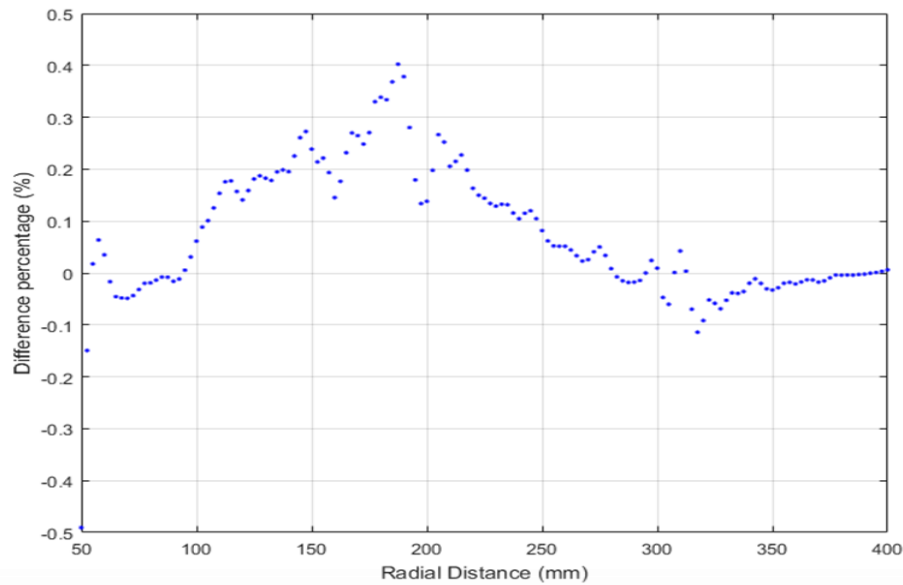


Figure 16: Percentage differences between temperatures calculated with Solidworks and PROOSIS at the same radial stations. The two compared temperature profiles are the ones shown in Figure 13.

Figure 16 indicates that the absolute temperature error is no more than 0.5%. As expected, it can be concluded that the solution that takes into account the thickness of the disk is far more accurate and the curve form is closer to reality. Also, the one-dimensional solution is a lot quicker than the FEA one. Thus, it is chosen for usage in the stress calculation and subsequently in the optimization algorithm.

## 4 Stress Analysis

### 4.1 Introduction to stress analysis

The methodology of disk stress calculation is based on in plane stress analysis and will be analyzed in this chapter. The disks of aircraft gas turbine engines are subjected to body forces, blade loads, thermal loads, shaft torque loads, engine thrust and landing loads. From the above, the most important loads for design are the body forces, blade loads and thermal loads since the rest occur only locally. The calculations assume plane stress condition, there are no variations of stresses and temperature gradient in the axial direction. Small angles are assumed due to the small displacements. The parts that connect the disks to the shaft are far less rigid than the disk and thus it is considered that they do not impose a radial or tangential stresses on the disks. These connecting parts are cylinders or cones and provide only shear and torsion [1]. In order to simulate the in-plane radial and tangential stresses the disk's cross section is discretized in small elements that are defined by their radial and tangential position and their radial and tangential span, as shown in Figure 17. The stress calculation described in this chapter is according to [2].

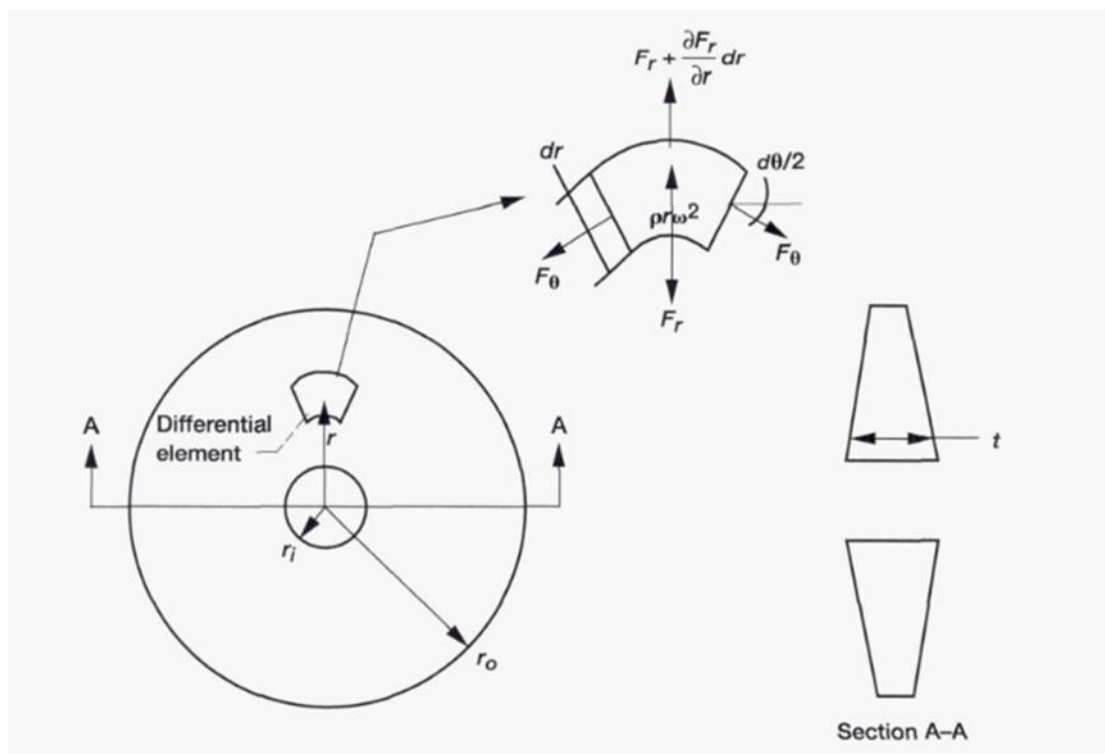


Figure 17: The disk is divided into elements [1]

## 4.2 Equations of stress analysis

Due to the single plane problem it applies that:

$$\frac{d}{dz} = 0, \tau_{rz} = \tau_{\theta z} = \sigma_z = 0$$

Also due to axisymmetry:

$$\frac{d}{d\theta} = 0$$

According to the balance of forces in every small element the following can be deduced [1]

$$\sum F_{\theta} = 0 \quad (26)$$

$$\sum F_r = 0 \Rightarrow \frac{dF_r}{dr} dr - F_{\theta} d\theta + t\rho r^2 \omega^2 dr d\theta = 0 \quad (27)$$

The forces acting on the surfaces of the differential elements can be expressed as:

$$F_r = \sigma_r r t d\theta \quad (28)$$

$$F_{\theta} = \sigma_{\theta} t dr \quad (29)$$

The equilibrium equation of the disk is obtained by substituting equations (28) and (29) into (27):

$$\frac{d}{dr}(t r \sigma_r) - t \sigma_{\theta} + t \rho r^2 \omega^2 = 0 \quad (30)$$

The strains can be obtained as:

$$\varepsilon_r = \frac{du}{dr} \quad (31)$$

$$\varepsilon_{\theta} = \frac{u}{r} \quad (32)$$

Every stress can be broken down to its two components, mechanical and thermal [2] :

$$\begin{bmatrix} \sigma_r \\ \sigma_\theta \\ \sigma_z \\ \tau_{rz} \\ \tau_{\theta z} \\ \tau_{r\theta} \end{bmatrix} = \begin{bmatrix} \sigma_r^m \\ \sigma_\theta^m \\ \sigma_z^m \\ \tau_{rz}^m \\ \tau_{\theta z}^m \\ \tau_{r\theta}^m \end{bmatrix} + \begin{bmatrix} \sigma_r^T \\ \sigma_\theta^T \\ \sigma_z^T \\ \tau_{rz}^T \\ \tau_{\theta z}^T \\ \tau_{r\theta}^T \end{bmatrix} \quad (33)$$

According to general form of Hooke's Law the stiffness tensor and the stresses are expressed as:

$$[\mathbf{C}] = \begin{bmatrix} C_{11} & C_{12} & C_{13} & 0 & 0 & 0 \\ C_{12} & C_{22} & C_{23} & 0 & 0 & 0 \\ C_{13} & C_{23} & C_{33} & 0 & 0 & 0 \\ 0 & 0 & 0 & C_{44} & 0 & 0 \\ 0 & 0 & 0 & 0 & C_{55} & 0 \\ 0 & 0 & 0 & 0 & 0 & C_{66} \end{bmatrix} \quad (34)$$

$$[\sigma^m] = [\mathbf{C}][\varepsilon] \quad (35)$$

$$[\sigma^T] = [\mathbf{C}][\beta]T \quad (36)$$

Where T is the difference of the temperature from the reference temperature.

$$\varepsilon = \begin{bmatrix} \varepsilon_r \\ \varepsilon_\theta \\ \varepsilon_z \\ \gamma_{rz} \\ \gamma_{\theta z} \\ \gamma_{r\theta} \end{bmatrix} = \begin{bmatrix} \frac{du}{dr} \\ \frac{u}{r} \\ -\frac{C_{13}}{C_{33}} \frac{du}{dr} - \frac{C_{23}}{C_{33}} \frac{u}{r} \\ 0 \\ 0 \\ 0 \end{bmatrix} \quad (37)$$

$$\beta = \begin{bmatrix} \beta_r \\ \beta_\theta \\ \beta_z \\ \beta_{rz} \\ \beta_{\theta z} \\ \beta_{r\theta} \end{bmatrix} = \begin{bmatrix} \alpha_r \\ \alpha_\theta \\ -\frac{C_{13}}{C_{33}} \alpha_r - \frac{C_{23}}{C_{33}} \alpha_\theta \\ 0 \\ 0 \\ 0 \end{bmatrix} \quad (38)$$

Where  $\varepsilon_z$  and  $\beta_z$  are calculated so that  $\sigma_z^m = \sigma_z^T = 0$  is satisfied.

Due to (33),(35),(36) the radial and tangential stress can be expressed as:

$$\sigma_r = A \frac{du}{dr} + B \frac{u}{r} - A\alpha_r T - B\alpha_\theta T \quad (39)$$

$$\sigma_\theta = B \frac{du}{dr} + D \frac{u}{r} - B\alpha_r T - D\alpha_\theta T \quad (40)$$

Where:

$$A = \frac{C_{11}C_{33} - C_{13}^2}{C_{33}}, B = \frac{C_{12}C_{33} - C_{13}C_{23}}{C_{33}}, \quad (41)$$

$$D = \frac{C_{22}C_{33} - C_{23}^2}{C_{33}}$$

And the stiffness tensor elements are:

$$C_{11} = C_{33} = \frac{E_r(E_\theta - E_r\nu_{\theta r}^2)}{E_\theta - 2E_r\nu_{\theta r}^2} \quad (42)$$

$$C_{22} = \frac{E_\theta^2}{E_\theta - 2E_r\nu_{\theta r}^2} \quad (43)$$

$$C_{12} = C_{23} = \frac{E_r E_\theta \nu_{\theta r}}{E_\theta - 2E_r\nu_{\theta r}^2} \quad (44)$$

$$C_{13} = \frac{E_r^2 \nu_{\theta r}^2}{E_\theta - 2E_r\nu_{\theta r}^2} \quad (45)$$

The equations above are general and cover anisotropic as well as isotropic materials.

However, in case the material is isotropic they can easily be converted by assuming  $E_r = E_\theta$  and  $\alpha_r = \alpha_\theta$ .

The boundary condition at the rim of the disk is the total centrifugal load of the carried dead weight divided by the cross-section area of these support points. The boundary radial stress value at the bore of the disk is considered to be zero since, as it is discussed above, the parts that connect the disk to the shaft are relatively flexible and do not impose radial stresses.

Consequently the bore boundary is :

$$\sigma_{r,bore} = A \frac{du}{dr} + B \frac{u}{r} - A\alpha_r T - B\alpha_\theta T \Big|_{r_{bore}} = 0 \quad (46)$$

The rim boundary is:

$$\sigma_{r,rim} = A \frac{du}{dr} + B \frac{u}{r} - A\alpha_r T - B\alpha_\theta T \Big|_{r_{rim}} = \frac{n_b m_b r_{cg}}{2\pi r_{rim} t} \omega^2 \quad (47)$$

### 4.3 Discretization of the analytical equations

#### 4.3.1 Stresses equation

The equation that should be solved and discretized is the equilibrium equation (30), with the use of stress expressions (39), (40) and boundary conditions (46), (47). The disk is radially discretized into n nodes, the first station is always the bore and the last station is the rim. There, the boundary conditions are applied. The discretization is executed with the use of 2 intervals [0,1] and [1,2] between three successive theoretical radial stations 0,1,2 or (i-1), i, (i+1) in the disk.

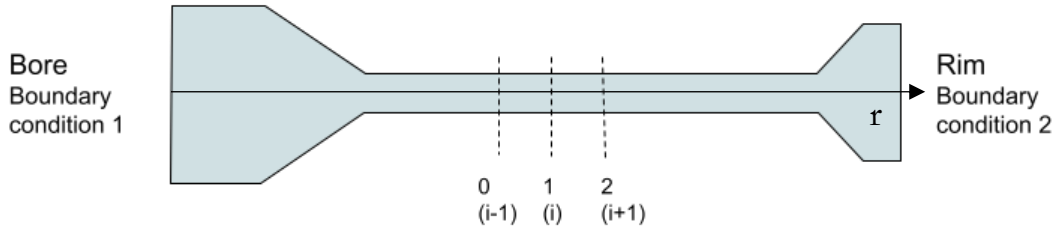


Figure 18: The disk is radially discretized into n stations; the first station is always the bore and the last station is the rim. There, the boundary conditions are applied. The discretization is executed with the use of 2 intervals [0,1] and [1,2] between three successive theoretical radial stations 0,1,2 or (i-1), i, (i+1) in the disk.

Assuming an auxiliary variable x the following formulas can be expressed. Variable x can be substituted with displacement u, thickness t, radius r, temperature T, terms A,B,D and thermal expansion coefficient a.

$$\Delta x_{21} = x_{i+1} - x_i \quad (48)$$

$$\Delta x_{10} = x_i - x_{i-1} \quad (49)$$

$$\bar{x}_{21} = \frac{x_{i+1} + x_i}{2} \quad (50)$$

$$\bar{x}_{10} = \frac{x_i + x_{i-1}}{2} \quad (51)$$

Average radial stress at the intervals [0,1] and [1,2] is calculated using (39):

$$\begin{aligned}\bar{\sigma}_{r10} &= \frac{\sigma_{r0} + \sigma_{r1}}{2} \\ &= \bar{A}_{10} \frac{\Delta u_{10}}{\Delta r_{10}} + \bar{B}_{10} \frac{\bar{u}_{10}}{\bar{r}_{10}} - \bar{A}_{10} \bar{a}_{r10} \bar{T}_{10} \\ &\quad - \bar{B}_{10} \bar{a}_{\theta10} \bar{T}_{10}\end{aligned}\quad (52)$$

$$\begin{aligned}\bar{\sigma}_{r21} &= \frac{\sigma_{r1} + \sigma_{r2}}{2} \\ &= \bar{A}_{21} \frac{\Delta u_{21}}{\Delta r_{21}} + \bar{B}_{21} \frac{\bar{u}_{21}}{\bar{r}_{21}} - \bar{A}_{21} \bar{a}_{r21} \bar{T}_{21} \\ &\quad - \bar{B}_{21} \bar{a}_{\theta21} \bar{T}_{21}\end{aligned}\quad (53)$$

The integration of equation (30) at the intervals [0,1] and [1,2] can be expressed as:

$$\begin{aligned}\int_1^2 \frac{d}{dr} (tr\sigma_r) dr &= \int_1^2 (t\sigma_\theta - t\rho r^2 \omega^2) dr \\ (tr\sigma_r)_2 - (tr\sigma_r)_1 &= \bar{t}_{21} \bar{\sigma}_{\theta21} \Delta r_{21} - \bar{t}_{21} \rho \omega^2 \left( \frac{r_2^3 - r_1^3}{3} \right)\end{aligned}\quad (54)$$

$$\begin{aligned}\int_0^1 \frac{d}{dr} (tr\sigma_r) dr &= \int_0^1 (t\sigma_\theta - t\rho r^2 \omega^2) dr \\ (tr\sigma_r)_1 - (tr\sigma_r)_0 &= \bar{t}_{10} \bar{\sigma}_{\theta10} \Delta r_{10} - \bar{t}_{10} \rho \omega^2 \left( \frac{r_1^3 - r_0^3}{3} \right)\end{aligned}\quad (55)$$

Integration of equation (40) in interval [1,2]:

$$\begin{aligned}\int_1^2 \sigma_\theta dr &= \int_1^2 B \frac{du}{dr} dr + \int_1^2 D \frac{u}{r} dr - \int_1^2 B \alpha_r T dr \\ &\quad - \int_1^2 D \alpha_\theta T dr\end{aligned}\quad (56)$$

$$\begin{aligned}\bar{\sigma}_{\theta21} \Delta r_{21} &= \bar{B}_{21} \Delta u_{21} + \bar{D}_{21} \bar{u}_{21} \ln \left( \frac{r_2}{r_1} \right) \\ &\quad - \bar{B}_{21} \bar{a}_{r21} \bar{T}_{21} \Delta r_{21} - \bar{D}_{21} \bar{a}_{\theta21} \bar{T}_{21} \Delta r_{21}\end{aligned}\quad (57)$$



Integration of equation (40) in interval  $[0,1]$ :

$$\begin{aligned} \int_0^1 \sigma_\theta dr = \int_0^1 B \frac{du}{dr} dr + \int_0^1 D \frac{u}{r} dr - \int_0^1 B \alpha_r T dr \\ - \int_0^1 D \alpha_\theta T dr \end{aligned} \quad (58)$$

$$\begin{aligned} \bar{\sigma}_{\theta 10} \Delta r_{10} = \bar{B}_{10} \Delta u_{10} + \bar{D}_{10} \bar{u}_{10} \ln \left( \frac{r_1}{r_0} \right) \\ - \bar{B}_{10} \bar{\alpha}_{r 10} \bar{T}_{10} \Delta r_{10} - \bar{D}_{10} \bar{\alpha}_{\theta 10} \bar{T}_{10} \Delta r_{10} \end{aligned} \quad (59)$$

We set:

$$\beta_1 = (tr)_1 \quad (60)$$

$$\beta_2 = (tr)_2 \quad (61)$$

Then by substituting in equation (54)

$$\beta_2 \sigma_{r2} - \beta_1 \sigma_{r1} = \bar{t}_{21} \bar{\sigma}_{\theta 21} \Delta r_{21} - \bar{t}_{21} \rho \omega^2 \left( \frac{r_2^3 - r_1^3}{3} \right) \quad (62)$$

Then substituting equation (57) into (62):

$$\begin{aligned} \beta_2 \sigma_{r2} - \beta_1 \sigma_{r1} = \bar{t}_{21} \left[ \bar{B}_{21} \Delta u_{21} + \bar{D}_{21} \bar{u}_{21} \ln \left( \frac{r_2}{r_1} \right) \right. \\ \left. - \bar{B}_{21} \bar{\alpha}_{r 21} \bar{T}_{21} \Delta r_{21} - \bar{D}_{21} \bar{\alpha}_{\theta 21} \bar{T}_{21} \Delta r_{21} \right. \\ \left. - \rho \omega^2 \left( \frac{r_2^3 - r_1^3}{3} \right) \right] \end{aligned} \quad (63)$$

Then we eliminate the term  $\beta_2 \sigma_{r2}$  by multiplying equation (53) by  $2\beta_2$  and then subtracting equation (63) from it:

$$\begin{aligned}
\sigma_{r_1} = & \left( \frac{2\beta_2}{\beta_2 + \beta_1} \right) \left[ \bar{A}_{21} \frac{\Delta u_{21}}{\Delta r_{21}} + \bar{B}_{21} \frac{\bar{u}_{21}}{\bar{r}_{21}} \right. \\
& - (\bar{A}_{21} \bar{a}_{r_{21}} + \bar{B}_{21} \bar{a}_{\theta_{21}}) \bar{T}_{21} \Big] \\
& + \left( \frac{\bar{t}_{21}}{\beta_2 + \beta_1} \right) \left[ -\bar{B}_{21} \Delta u_{21} - \bar{D}_{21} \bar{u}_{21} \ln \left( \frac{r_2}{r_1} \right) \right. \\
& + (\bar{B}_{21} \bar{a}_{r_{21}} + \bar{D}_{21} \bar{a}_{\theta_{21}}) \bar{T}_{21} \Delta r_{21} \\
& \left. + \rho \omega^2 \left( \frac{r_2^3 - r_1^3}{3} \right) \right] \quad (64)
\end{aligned}$$

We follow the same procedure to express  $\sigma_{r_1}$  over interval  $[0,1]$ . We set:

$$\beta_0 = (tr)_0 \quad (65)$$

$$\beta_1 = (tr)_1 \quad (66)$$

Then equation (55) is written as:

$$\beta_1 \sigma_{r_1} - \beta_0 \sigma_{r_0} = \bar{t}_{10} \bar{\sigma}_{\theta_{10}} \Delta r_{10} - \bar{t}_{10} \rho \omega^2 \left( \frac{r_1^3 - r_0^3}{3} \right) \quad (67)$$

Substituting equation (59) into equation (67) gives:

$$\begin{aligned}
\beta_1 \sigma_{r_1} - \beta_0 \sigma_{r_0} = & \bar{t}_{10} \left[ \bar{B}_{10} \Delta u_{10} + \bar{D}_{10} \bar{u}_{10} \ln \left( \frac{r_1}{r_0} \right) \right. \\
& - \bar{B}_{10} \bar{a}_{r_{10}} \bar{T}_{10} \Delta r_{10} - \bar{D}_{10} \bar{a}_{\theta_{10}} \bar{T}_{10} \Delta r_{10} \\
& \left. - \rho \omega^2 \left( \frac{r_1^3 - r_0^3}{3} \right) \right] \quad (68)
\end{aligned}$$

Then we eliminate the term  $\beta_0 \sigma_{r_0}$  by multiplying equation (52) by  $2\beta_0$  and then adding it with equation (68):

$$\begin{aligned}
\sigma_{r_1} = & \left( \frac{2\beta_0}{\beta_1 + \beta_0} \right) \left[ \bar{A}_{10} \frac{\Delta u_{10}}{\Delta r_{10}} + \bar{B}_{10} \frac{\bar{u}_{10}}{\bar{r}_{10}} \right. \\
& - (\bar{A}_{10} \bar{a}_{r_{10}} + \bar{B}_{10} \bar{a}_{\theta_{10}}) \bar{T}_{10} \Big] \\
& + \left( \frac{\bar{t}_{10}}{\beta_1 + \beta_0} \right) \left[ \bar{B}_{10} \Delta u_{10} \right. \\
& + \bar{D}_{10} \bar{u}_{10} \ln \left( \frac{r_1}{r_0} \right) \\
& - (\bar{B}_{10} \bar{a}_{r_{10}} + \bar{D}_{10} \bar{a}_{\theta_{10}}) \bar{T}_{10} \Delta r_{10} \\
& \left. - \rho \omega^2 \left( \frac{r_1^3 - r_0^3}{3} \right) \right] \quad (69)
\end{aligned}$$

After this procedure there are two different expressions for  $\sigma_{r1}$ , (64) and (69). Into these equations we substitute  $\Delta u$  and  $\bar{u}$  according to (48)-(51)

$$\Delta u_{21} = u_{i+1} - u_i \quad (70)$$

$$\Delta u_{10} = u_i - u_{i-1} \quad (71)$$

$$\bar{u}_{21} = \frac{u_{i+1} + u_i}{2} \quad (72)$$

$$\bar{u}_{10} = \frac{u_i + u_{i-1}}{2} \quad (73)$$

Equating the two expressions of  $\sigma_{r1}$  gives an equation which comprises of terms with  $u_{i-1}, u_i, u_{i+1}$  multiplied by their coefficients and remaining terms called RHS (right hand side of the equation). The coefficients are:

$$\begin{aligned} Coeff. u_{i-1} = & \left( \frac{2\beta_0}{\beta_1 + \beta_0} \right) \left( \frac{\bar{A}_{10}}{\Delta r_{10}} - \frac{\bar{B}_{10}}{2r_{10}} \right) \\ & + \left( \frac{\bar{t}_{10}}{\beta_1 + \beta_0} \right) \left( \bar{B}_{10} - \frac{\bar{D}_{10}}{2} \ln \left( \frac{r_1}{r_0} \right) \right) \end{aligned} \quad (74)$$

$$\begin{aligned} Coeff. u_i = & \left( \frac{2\beta_2}{\beta_1 + \beta_2} \right) \left( \frac{-\bar{A}_{21}}{\Delta r_{21}} + \frac{\bar{B}_{21}}{2r_{21}} \right) \\ & + \left( \frac{\bar{t}_{21}}{\beta_1 + \beta_2} \right) \left( \bar{B}_{21} - \frac{\bar{D}_{21}}{2} \ln \left( \frac{r_2}{r_1} \right) \right) \\ & - \left( \frac{2\beta_0}{\beta_1 + \beta_0} \right) \left( \frac{\bar{A}_{10}}{\Delta r_{10}} - \frac{\bar{B}_{10}}{2r_{10}} \right) \\ & - \left( \frac{\bar{t}_{10}}{\beta_1 + \beta_0} \right) \left( \bar{B}_{10} + \frac{\bar{D}_{10}}{2} \ln \left( \frac{r_1}{r_0} \right) \right) \end{aligned} \quad (75)$$

$$\begin{aligned} Coeff. u_{i+1} = & \left( \frac{2\beta_2}{\beta_1 + \beta_2} \right) \left( \frac{\bar{A}_{21}}{\Delta r_{21}} + \frac{\bar{B}_{21}}{2r_{21}} \right) \\ & - \left( \frac{\bar{t}_{21}}{\beta_1 + \beta_2} \right) \left( \bar{B}_{21} + \frac{\bar{D}_{21}}{2} \ln \left( \frac{r_2}{r_1} \right) \right) \end{aligned} \quad (76)$$

The right hand side of the equation is:

$$\begin{aligned}
RHS = & \left( \frac{2\beta_2 \bar{T}_{21}}{\beta_1 + \beta_2} \right) (\bar{A}_{21} \bar{a}_{r21} + \bar{B}_{21} \bar{a}_{\theta 21}) \\
& - \left( \frac{\bar{t}_{21} \bar{T}_{21} \Delta r_{21}}{\beta_1 + \beta_2} \right) (\bar{B}_{21} \bar{a}_{r21} + \bar{D}_{21} \bar{a}_{\theta 21}) \\
& - \left( \frac{2\beta_0 \bar{T}_{10}}{\beta_1 + \beta_0} \right) (\bar{A}_{10} \bar{a}_{r10} + \bar{B}_{10} \bar{a}_{\theta 10}) \\
& - \left( \frac{\bar{t}_{10} \bar{T}_{10} \Delta r_{10}}{\beta_1 + \beta_0} \right) (\bar{B}_{10} \bar{a}_{r10} + \bar{D}_{10} \bar{a}_{\theta 10}) \quad (77) \\
& - \left( \frac{\bar{t}_{21}}{\beta_1 + \beta_2} \right) \rho \omega^2 \left( \frac{r_2^3 - r_1^3}{3} \right) \\
& - \left( \frac{\bar{t}_{10}}{\beta_1 + \beta_0} \right) \rho \omega^2 \left( \frac{r_1^3 - r_0^3}{3} \right)
\end{aligned}$$

Assuming that the disk is discretized by  $n$  nodes, the equation above can be applied onto the  $(n-2)$  internal nodes. The remaining 2 equations are obtained by the boundary conditions.

#### 4.3.2 Stress Boundary Conditions

For the bore boundary the displacement derivative is expressed via the three-point forward difference approximation:

$$\frac{du}{dr} = \frac{4u_2 - u_3 - 3u_1}{r_3 - r_1} \quad (78)$$

By substituting (78), equation (46) can be written:

$$\begin{aligned}
\sigma_{r,bore} &= A \frac{du}{dr} + B \frac{u}{r} - A\alpha_r T - B\alpha_\theta T \Big|_{r_{bore}} = 0, \\
\sigma_{r,bore} &= A_1 \left( \frac{4u_2 - u_3 - 3u_1}{r_3 - r_1} \right) + B_1 \frac{u_1}{r_1} - A_1 \alpha_{r1} T_1 \quad (79) \\
&\quad - B_1 \alpha_{\theta 1} T_1 = 0
\end{aligned}$$

And the coefficients can be deduced:

$$Coeff.u_1 = \frac{B_1}{r_1} - \frac{3A_1}{r_3 - r_1} \quad (80)$$

$$Coeff.u_2 = \frac{4A_1}{r_3 - r_1} \quad (81)$$

$$Coeff.u_3 = -\frac{A_1}{r_3 - r_1} \quad (82)$$

$$RHS = A_1 \alpha_{r1} T_1 + B_1 \alpha_{\theta 1} T_1 \quad (83)$$

For the rim boundary the displacement derivative is expressed via the three-point backward difference approximation:

$$\frac{du}{dr} = \frac{3u_n - 4u_{n-1} + u_{n-2}}{r_n - r_{n-2}} \quad (84)$$

Thus, equation (47) can be written:

$$\begin{aligned} \sigma_{r,rim} &= A \frac{du}{dr} + B \frac{u}{r} - A\alpha_r T - B\alpha_\theta T \Big|_{r_{rim}} = \frac{n_b m_b r_{cg}}{2\pi r_n t_n} \omega^2, \\ \sigma_{r,rim} &= A_n \left( \frac{3u_n - 4u_{n-1} + u_{n-2}}{r_n - r_{n-2}} \right) + B_n \frac{u_n}{r_n} \\ &\quad - A_n \alpha_{rn} T_n - B_n \alpha_{\theta n} T_n \\ &= \frac{n_b m_b r_{cg}}{2\pi r_n t_n} \omega^2 \end{aligned} \quad (85)$$

$$Coeff.u_{n-2} = \frac{A_n}{r_n - r_{n-2}} \quad (86)$$

$$Coeff.u_{n-1} = \frac{-4A_n}{r_n - r_{n-2}} \quad (87)$$

$$Coeff.u_n = \frac{B_n}{r_n} + \frac{3A_n}{r_n - r_{n-2}} \quad (88)$$

$$RHS = \frac{n_b m_b r_{cg}}{2\pi r_n t_n} \omega^2 + A_n \alpha_{rn} T_n + B_n \alpha_{\theta n} T_n \quad (89)$$

#### 4.3.3 Stresses Final solution procedure

The coefficients formulated above are used to construct a (nxn) matrix, this matrix is multiplied by the vector (nx1) of radial displacements at every node. The right side of the system is the vector comprised of the RHSs.

$$\begin{bmatrix}
(80) & (81) & (82) & 0 & 0 & 0 & 0 \\
(74) & (75) & (76) & 0 & 0 & 0 & 0 \\
0 & (74) & (75) & (76) & 0 & 0 & 0 \\
0 & 0 & \dots & \dots & \dots & 0 & 0 \\
0 & 0 & 0 & (74) & (75) & (76) & 0 \\
0 & 0 & 0 & 0 & (74) & (75) & (76) \\
0 & 0 & 0 & 0 & (86) & (87) & (88)
\end{bmatrix}
\begin{bmatrix}
u_1 \\
u_2 \\
u_3 \\
\dots \\
u_{n-2} \\
u_{n-1} \\
u_n
\end{bmatrix}
=
\begin{bmatrix}
(83) \\
(77) \\
(77) \\
\dots \\
(77) \\
(77) \\
(89)
\end{bmatrix} \quad (90)$$

The five-diagonal system described in equation (90) is transformed into a tridiagonal system by elimination of 2 diagonal vectors.

The first two rows of the system can be expressed as:

$$c_{80}u_1 + c_{81}u_2 + c_{82}u_3 = c_{83} \quad (91)$$

$$c_{74}u_1 + c_{75}u_2 + c_{76}u_3 = c_{77} \quad (92)$$

In order to make  $c_{82}$  equal to zero :

$$(91) - \frac{c_{82}}{c_{76}}(92) \Rightarrow$$

$$\left(c_{80} - \frac{c_{82}}{c_{76}}c_{74}\right)u_1 + \left(c_{81} - \frac{c_{82}}{c_{76}}c_{75}\right)u_2 = c_{83} - \frac{c_{82}}{c_{76}}c_{77} \quad (93)$$

Equation (93) becomes the new first row.

The last two rows can be expressed as:

$$c_{74}u_{n-2} + c_{75}u_{n-1} + c_{76}u_n = c_{77} \quad (94)$$

$$c_{86}u_{n-2} + c_{87}u_{n-1} + c_{88}u_n = c_{89} \quad (95)$$

In order to make  $c_{86}$  equal to zero

$$(95) - \frac{c_{86}}{c_{74}}(94) \Rightarrow$$

$$\left(c_{87} - \frac{c_{86}}{c_{74}}c_{75}\right)u_{n-1} + \left(c_{88} - \frac{c_{86}}{c_{74}}c_{76}\right)u_n = c_{89} - \frac{c_{86}}{c_{74}}c_{77} \quad (96)$$

Equation (96) becomes the new last row

The resulting tridiagonal system is solved with a common algorithm as described in the previous chapter.

Once the system is solved and the displacements are found their derivative can be numerically computed and thus the radial and tangential stresses can be calculated at every node according to equations (39),(40). Von mises stress is given by the equation:

$$\sigma_{von\ Mises} = \sqrt{\frac{(\sigma_1 - \sigma_2)^2 + (\sigma_2 - \sigma_3)^2 + (\sigma_3 - \sigma_1)^2}{2}}$$

In a plane stress problem:

$$\sigma_1 = \sigma_r$$

$$\sigma_2 = \sigma_\theta$$

$$\sigma_3 = 0$$

Thus:

$$\sigma_{von\ Mises} = \sqrt{\frac{(\sigma_r - \sigma_\theta)^2 + \sigma_\theta^2 + \sigma_r^2}{2}}$$

## 4.4 Stress calculation implementation in PROOSIS

Stress calculation is executed by calling the function `calcDiskS_FV`. The inputs are:

<b>istg:</b>	The number of the stage. It is used for naming the file with the results
<b>compINSTANCE_NAME:</b>	The name of the engine. It is used for naming the file with the results
<b>NmechDes:</b>	Disk rotational speed (rpm)
<b>NmaxQNdes:</b>	Disk overspeed factor
<b>Nd:</b>	The number of nodes
<b>R[Nd]:</b>	Discretized disk radius
<b>t[Nd]:</b>	Discretized disk thickness
<b>T_in[Nd]:</b>	Input temperature radial distribution
<b>rho:</b>	Material Density
<b>Er [Nd]:</b>	Elastic modulus of the material in the radial direction
<b>Et[Nd]:</b>	Elastic modulus of the material in the tangential direction
<b>ar[Nd]:</b>	Thermal expansion coefficient of the material in the radial direction
<b>at[Nd]:</b>	Thermal expansion coefficient of the material in the tangential direction
<b>nu[Nd]:</b>	Material poisson ratio
<b>sigma_rr_bbv:</b>	Boundary radial stress at the bore
<b>sigma_rr_rbv:</b>	Boundary tangential stress at the bore
<b>includeHeatTrans:</b>	Boolean variable. If it is TRUE , heat transfer effects are included.
<b>dT_in:</b>	Temperature adder to the reference temperature, which is considered the room temperature
<b>printFuncRpts:</b>	Boolean variable. If it is TRUE , the results are printed inside files

The outputs of the function are:

<b>sigma_rr[Nd]:</b>	Radial stress profile
<b>sigma_tt[Nd]:</b>	Tangential stress profile
<b>sigma_vM[Nd]:</b>	Von Mises stress profile



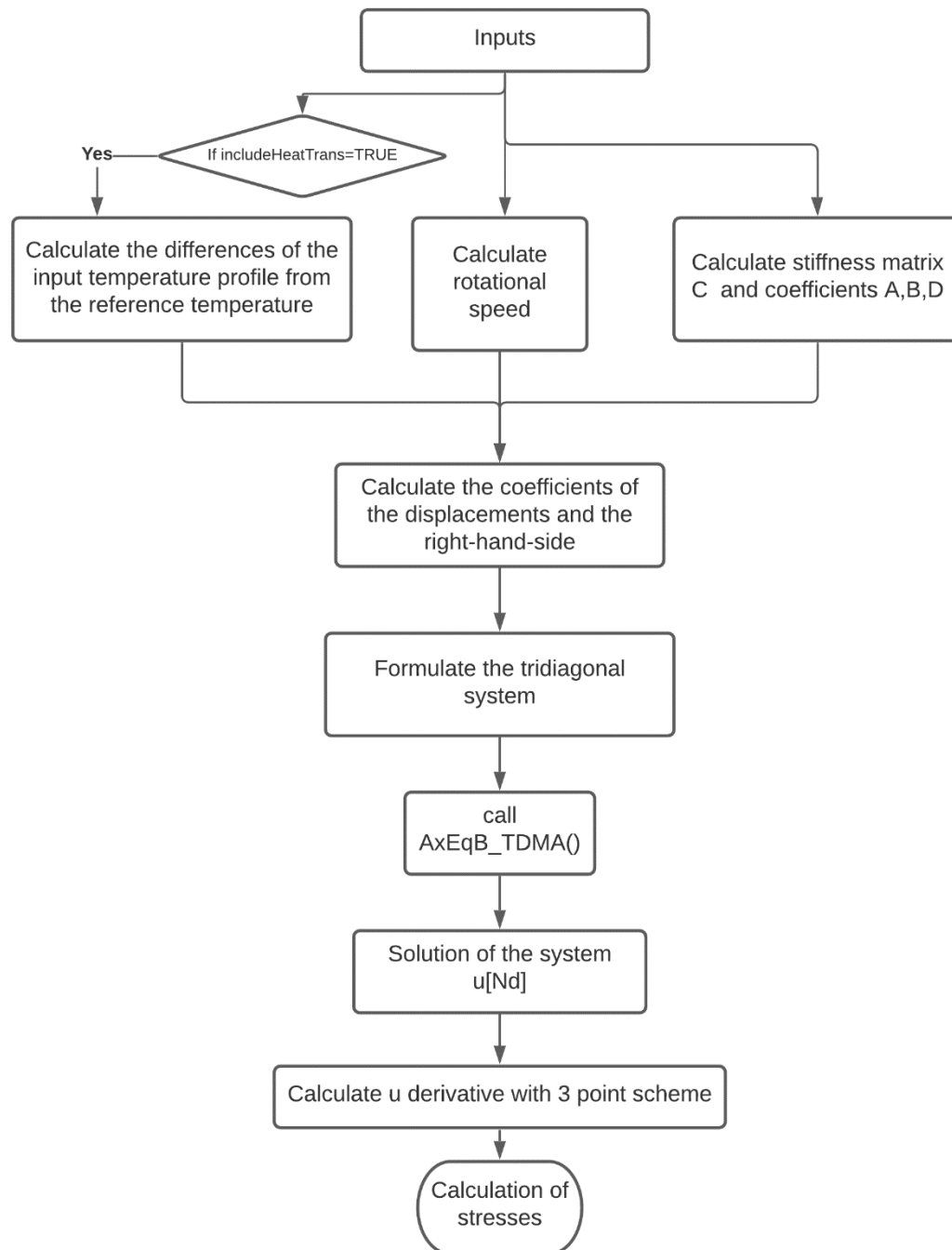


Figure 19: Workflow of the stress calculating function calcDiskS\_FV()

## 5. Stresses validation with Solidworks

### 5.1 Introduction to stress validation

The validation was implemented using the geometry of the three first stages' disks of NASA's E3 Engine. The dimensions of the disks were extracted by the digitization of the high-pressure compressor drawings [4]. Table 1 summarizes the geometry, material, disk type and rotational speed of the 3 first stages of the High Pressure Compressor as obtained from [4]:

Stage Index	1	2	3
Rotational Speed $\omega$ (rad/s)	1300.3		
Material	Ti-8-1-1	Ti-6Al-4V	Ti-6Al-4V
Density (kg/m <sup>3</sup> )	4370.0	4430.0	4430.0
Disk Type	RING	HYPERBOLIC	WEB
R1 (m) Bore Radius	0.1041	0.1066	0.1063
R2 (m)	0.1142	0.1210	0.1201
R3 (m)	0.1243	0.1401	0.1536
R4 (m)	0.1344	0.1700	0.1986
R5 (m)	0.1445	0.1967	0.2171
R6 (m) Rim Radius	0.1546	0.2020	0.2303
t1 (m)	0.0937	0.0329	0.0247
t2 (m)	0.0937	0.0329	0.0247
t3 (m)	0.0937	0.0153	0.0062
t4 (m)	0.0937	0.0075	0.0062
t5 (m)	0.0937	0.0462	0.0281
t6 (m) Rim Thickness	0.0937	0.0462	0.0281

Table 2 E3 Disks Information

Using the information of Table 2 Table 2 E3 Disks Information the three disks were modeled in Solidworks and for each of them two static studies were run for two different load cases. For the third load case which is the only one that includes temperature gradient the turbine disk described in Table 1 is used. The results of the PROOSIS stress calculation function were compared with the results of Solidworks studies.

### 5.2 Brief Description of Finite Element Analysis (FEA)

Solidworks uses Finite Element Analysis to calculate the stresses. This method is three-dimensional since the whole part is divided (meshed) into tetrahedrons. A tetrahedron element has 4 nodes with 6 degrees of freedom (DOFs) each. Six DOFs model every type of displacement in the three dimensions. The DOFs variables are collected inside the  $u$  vector. Also, each element has a known matrix of elasticity  $K$ . If the matrices of elasticity of all elements are combined properly, with respect to the common DOFs between bordering elements, a global matrix of elasticity is formed. Therefore, it applies:

$$[F] = [K_{global}] \cdot [u]$$

After the equation is solved, the strains can be calculated from the displacements vector  $u$ . Thus, the stresses are calculated as follows:

$$[\sigma] = [E] \cdot [\varepsilon]$$

### 5.3 Validation Process

The following validation cases were examined:

For E3 HPC three first disks:

- a) There is no temperature gradient, the disk is at room temperature. The disk bore and rim stresses are zero. The only loads are the body centrifugal loads.
- b) There is no temperature gradient, the disk is at room temperature. The disk bore stress is zero, the rim stress is as imposed from the dead weight and there are body centrifugal loads.

For an arbitrary turbine disk with geometry described in Table 1:

- c) There is temperature gradient. The disk bore stress is zero, the rim stress is as imposed from the dead weight and there are body centrifugal loads.

Load case	a	b	c
Temperature gradient	no	no	yes
Disk bore stress	no	no	no
Disk rim stress	no	yes	yes
Centrifugal body loads	yes	yes	yes

Table 3 The load cases

#### 5.3.1 Boundary conditions and formulation of load cases

Substituting E3 blade dimensions into the equations described in section 1.4 we obtain the values of the boundary conditions. The main calculations are summarized in Table 4:

Stage Index	1	2	3
Blades Number $n_b$	28	38	50
Overall Blade Weight $m_b$ (kg)	0.8656	0.2792	0.1171
Overall Blade Center of Gravity $r_{cg}$ (m)	0.199106	0.230983	0.253347
Rim Load $\sigma_{r,rim}$ (MPa)	89.7	70.6	61.6

Table 4 Rim stress calculations

Thus, the load cases conditions are summarized in the Tables 5,6 and 7.

LOAD CASE	a		
Geometry, material	See Table 2		
Stage Index	1	2	3
Temperature gradient	-	-	-
Bore Load $\sigma_{r,bore}$ (MPa)	0	0	0
Rim Load $\sigma_{r,rim}$ (MPa)	0	0	0
Rotational velocity (rad/s)	1300.3		

Table 5: Load case a description

LOAD CASE	b		
Geometry , material	See Table 2		
Stage Index	1	2	3
Temperature gradient	-	-	-
Bore Load $\sigma_{r,bore}$ (MPa)	0	0	0
Rim Load $\sigma_{r,rim}$ (MPa)	89.7	70.6	61.6
Rotational velocity (rad/s)	1300.3		

Table 6: Load case b description

LOAD CASE	c	
Geometry, material	See Table 1	
Temperature gradient	Tbore (K)	398.15
	Trim (K)	823.15
Bore Load $\sigma_{r,bore}$ (MPa)	0	
Rim Load $\sigma_{r,rim}$ (MPa)	66.8	
Rotational velocity (rad/s)	392.7	

Table 7: Load case c description

### 5.3.2 Solidworks settings

FEM method is a three-dimensional method and hence, it can calculate stress concentration, as well as stress gradients at the axial direction. Consequently, in order to compare the results of the two methods under the same circumstances, in the Solidworks environment sensors of radial and tangential stresses are put throughout the centerline of the disk contour, as shown in Figure 20, Figure 21 and Figure 22:

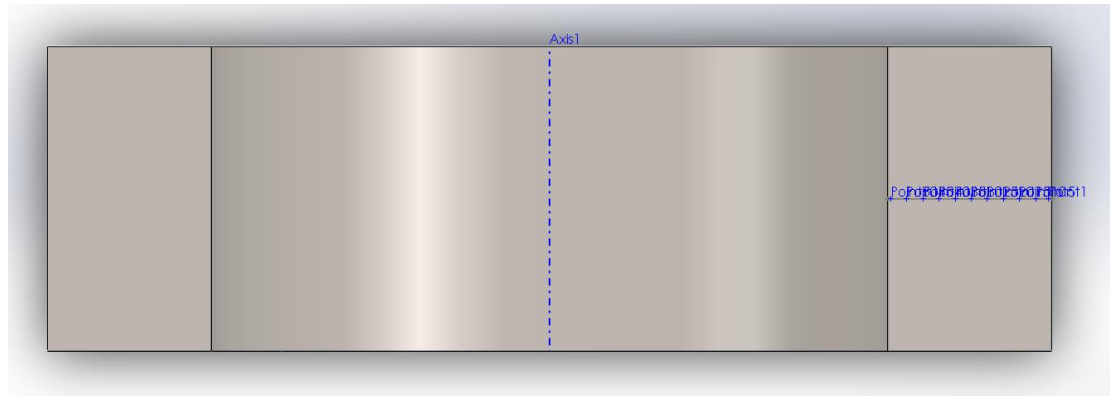


Figure 20 : Section view of 1st stage of HPC in E3. The blue points are sensors of stress.



Figure 21: Section view of 2nd stage of HPC in E3. The blue points are sensors of stress.

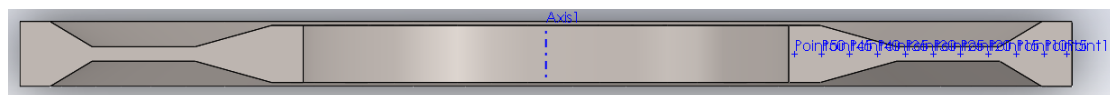


Figure 22: Section view of 3rd stage of HPC in E3. The blue points are sensors of stress.

Another challenge was that most FEM software requires the movement of the object to be restricted at every axis. This means that at least one face or edge of the part should be a fixture which means zero displacement there. All fixtures together should restrict the movement of the component at all three directions. In reality disks are not radially restricted, there is no point with zero displacement since all points including the bore are centrifuged in higher radii. This was something modelled in the analytical solution of the previous chapter with the zero-stress boundary condition at the bore. However, commercial software like Solidworks cannot accept stress boundaries so Inertial Relief was used to avoid the fixtures. This setting calculates the opposite inertial load and imposes it to every node so that the part is balanced without fixtures needed.

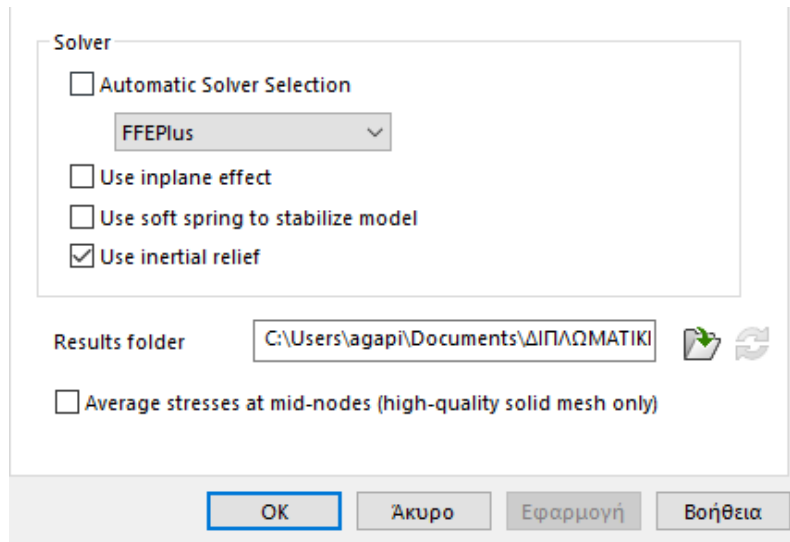


Figure 23 Inertial relief setting.

Finally, for load case c it should be noted that the Solidworks solver cannot handle the change of the material properties at every node that the temperature gradient causes. Thus, INCONEL 718 properties are considered those at temperature  $T=373.15$  K and constant throughout the radius. PROOSIS function is capable of reading the material properties at every node in accordance with the temperature profile, so in order to match this with the PROOSIS stress calculation the temperature at which the material properties are read is manually changed to 373.15 K and kept it constant at every node for the comparison.

### 5.3.3 Mesh Independence

A mesh independence study was conducted. For every disk we run the analysis multiple times, each time reducing the element size until the maximum von Mises stress converges. The study used for mesh independence is the load case a) for E3 HPC disks.

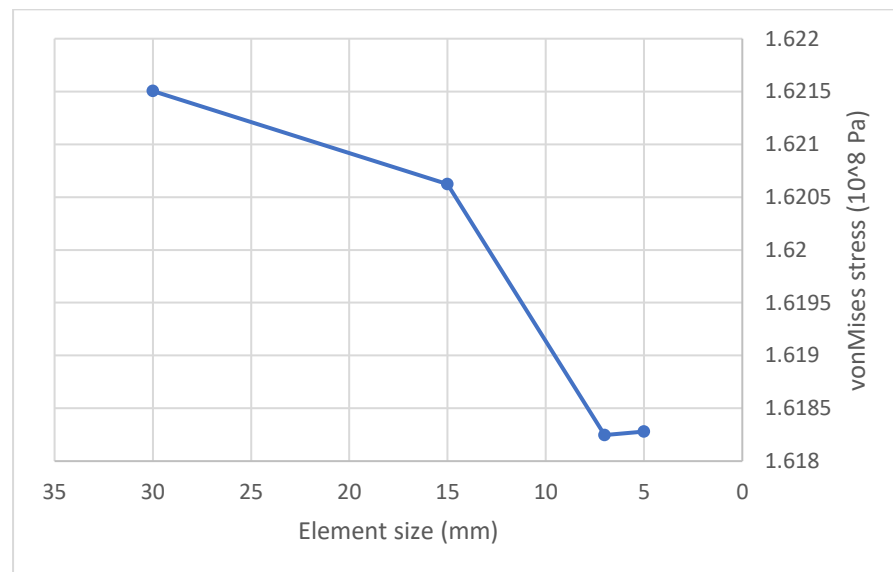


Figure 24: Mesh independence chart for 1<sup>st</sup> stage disk of HPC NASA/GE E3.

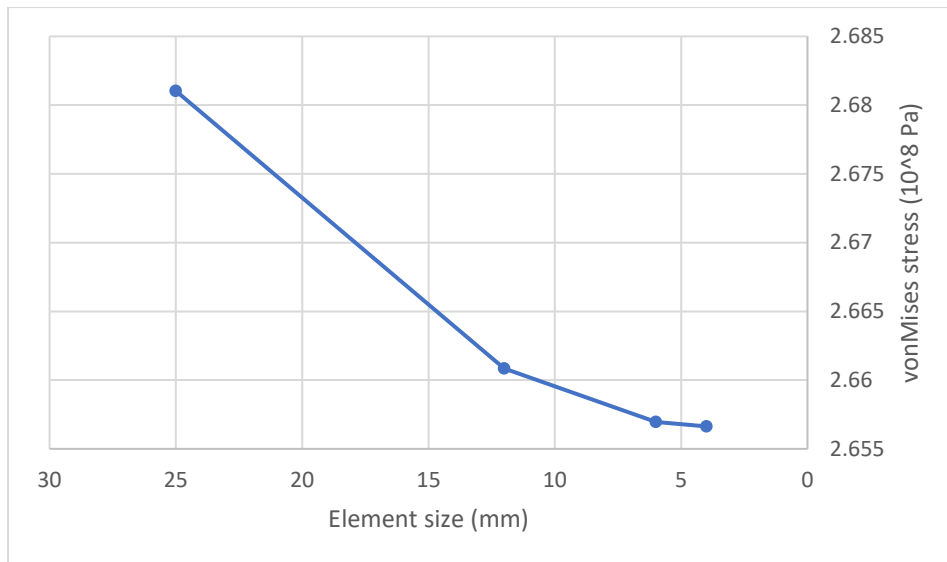


Figure 25: Mesh independence chart for 2<sup>nd</sup> stage disk of HPC NASA/GE E3.

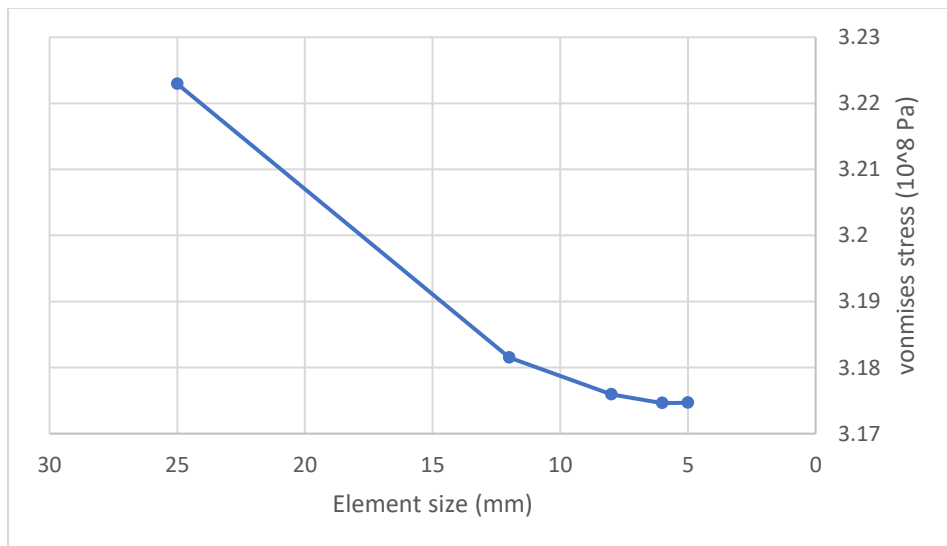


Figure 26: Mesh independence chart for 3<sup>rd</sup> stage disk of HPC NASA/GE E3.

### 5.3.4 Results Comparison

In this paragraph the resulting stress curves of PROOSIS algorithm and Solidworks static analysis are compared. The radial stress is symbolized as  $\sigma_{rr}$  and  $\sigma_{tt}$  the tangential stress.

For Stage 1

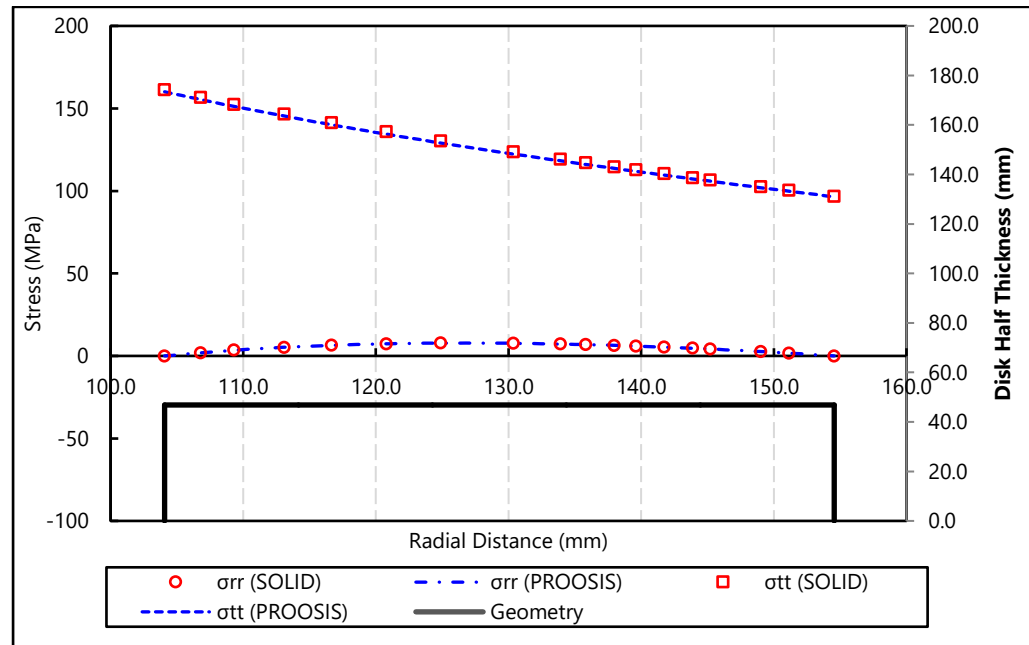


Figure 27: Stress curves comparison for NASA/GE E3 HPC ,Stage 1, Load case a): zero bore stress,zero rim stress,no temperature gradient

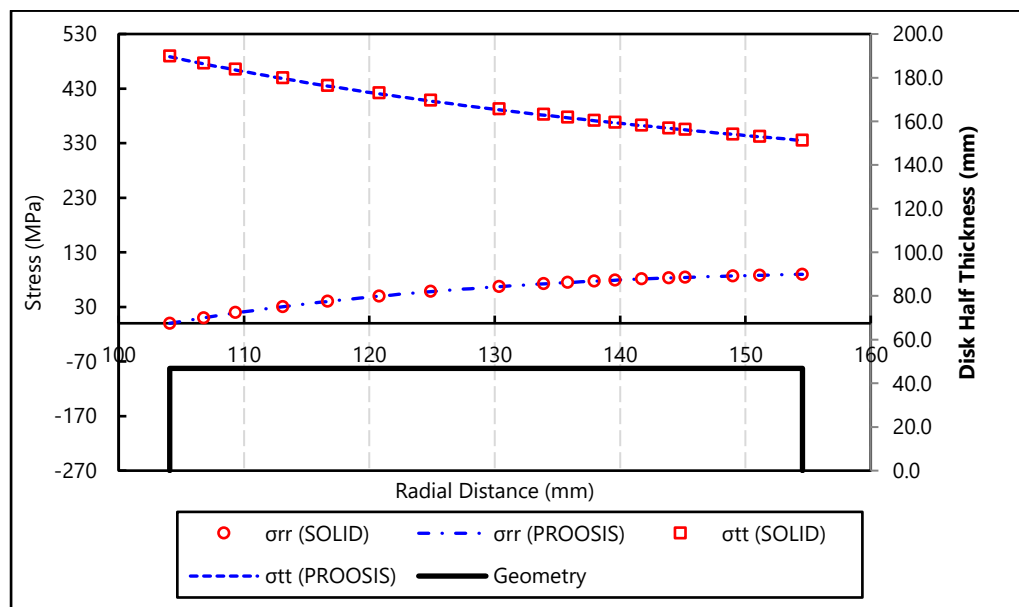


Figure 28: Stress curves comparison for NASA/GE E3 HPC, Stage 1, Load case b): zero bore stress, non-zero rim stress, no temperature gradient



For Stage 2:

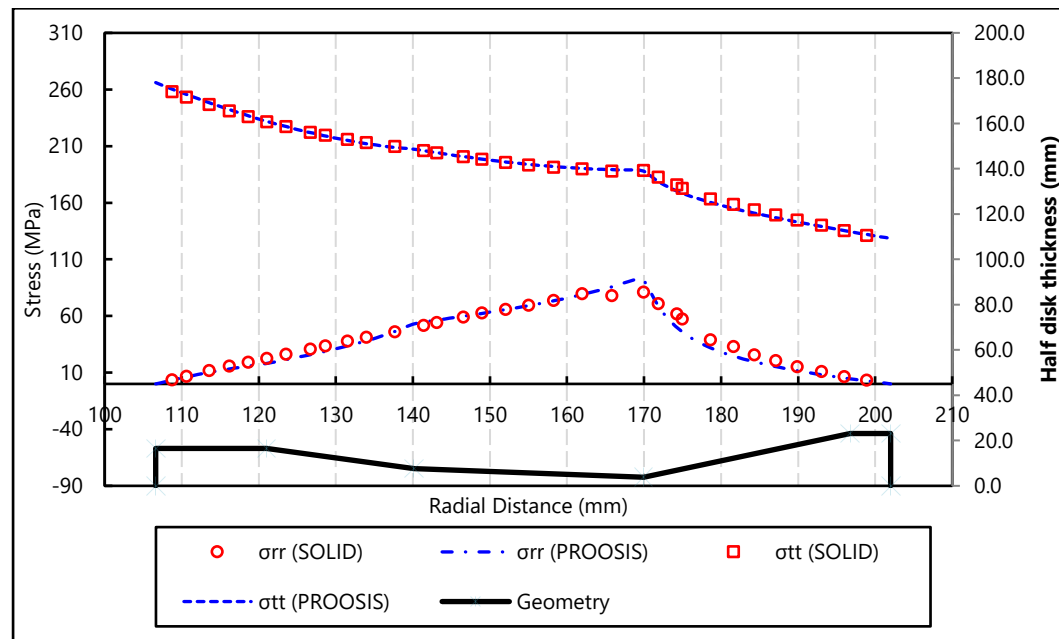


Figure 29: Stress curves comparison for NASA/GE E3 HPC, Stage 2, Load case a): zero bore stress, zero rim stress, no temperature gradient

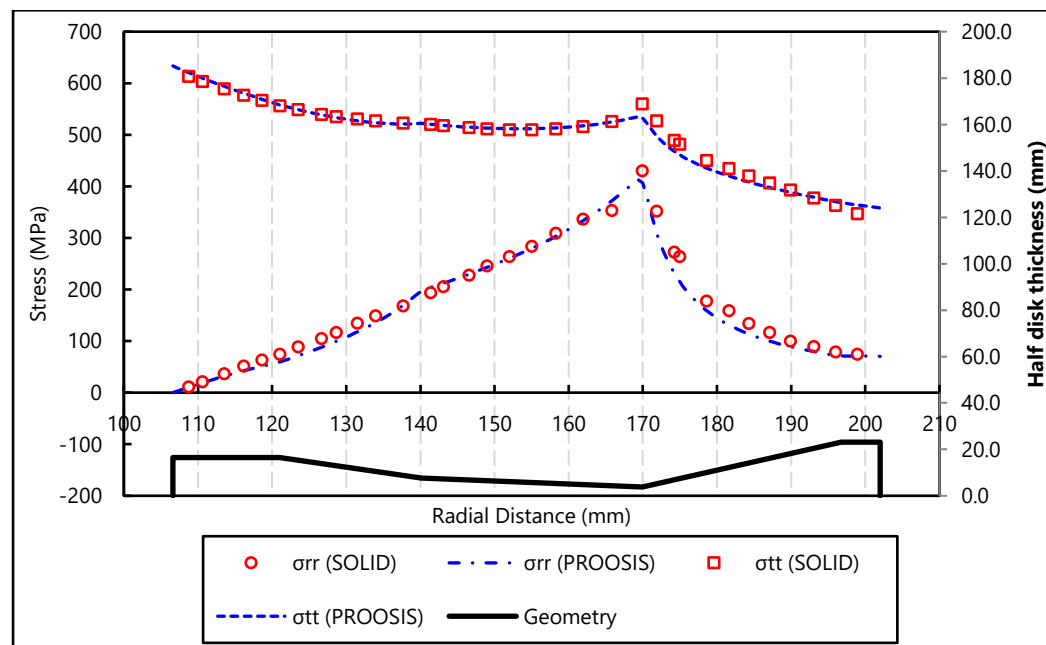


Figure 30: Stress curves comparison for NASA/GE E3 HPC, Stage 2, Load case b): zero bore stress, non-zero rim stress, no temperature gradient

For Stage 3:

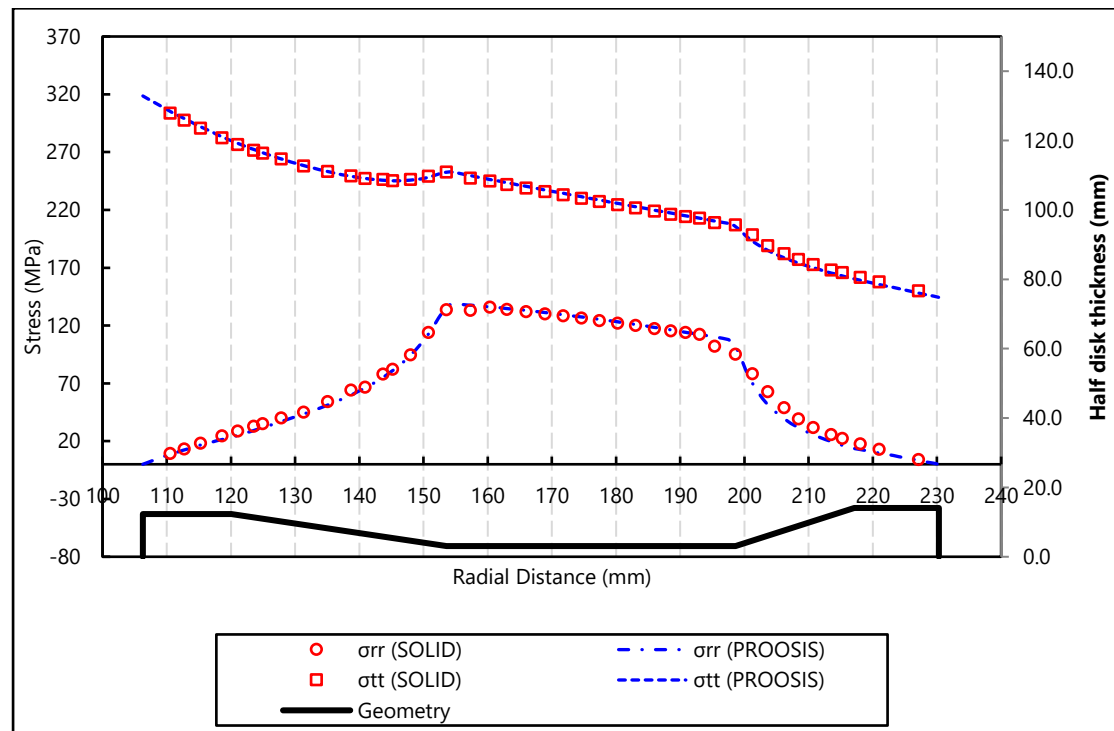


Figure 31: Stress curves comparison for NASA/GE E3 HPC, Stage 3, Load case a): zero bore stress, zero rim stress, no temperature gradient

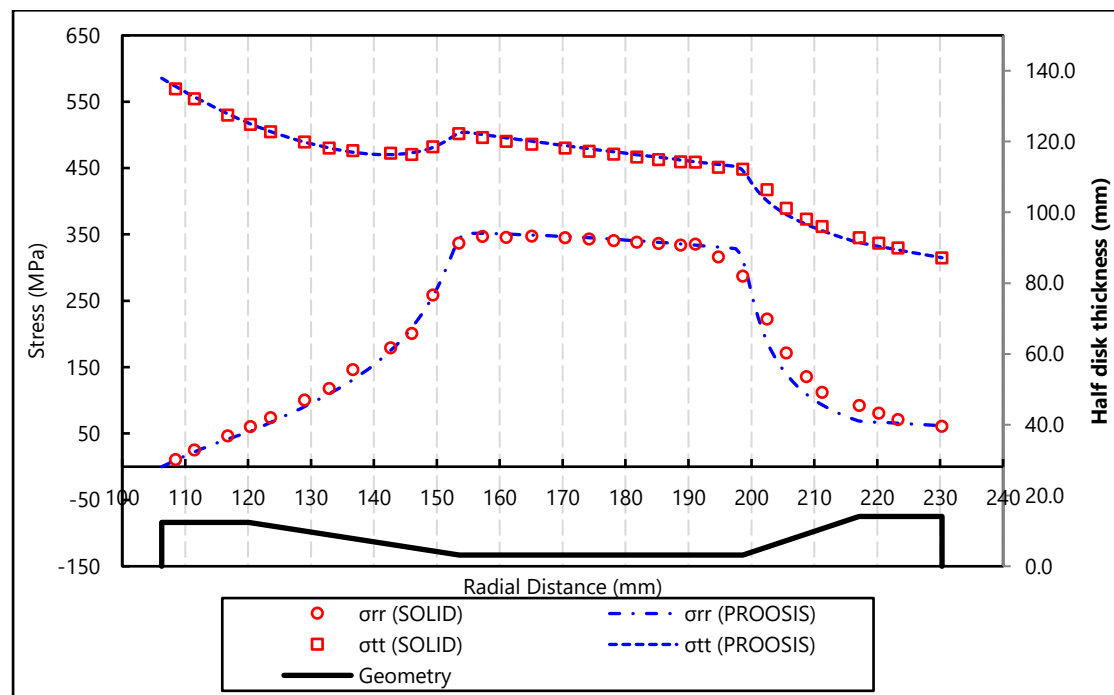


Figure 32: Stress curves comparison for NASA/GE E3 HPC, Stage 3, Load case b): zero bore stress, non-zero rim stress, no temperature gradient

For Turbine Disk Load case c:

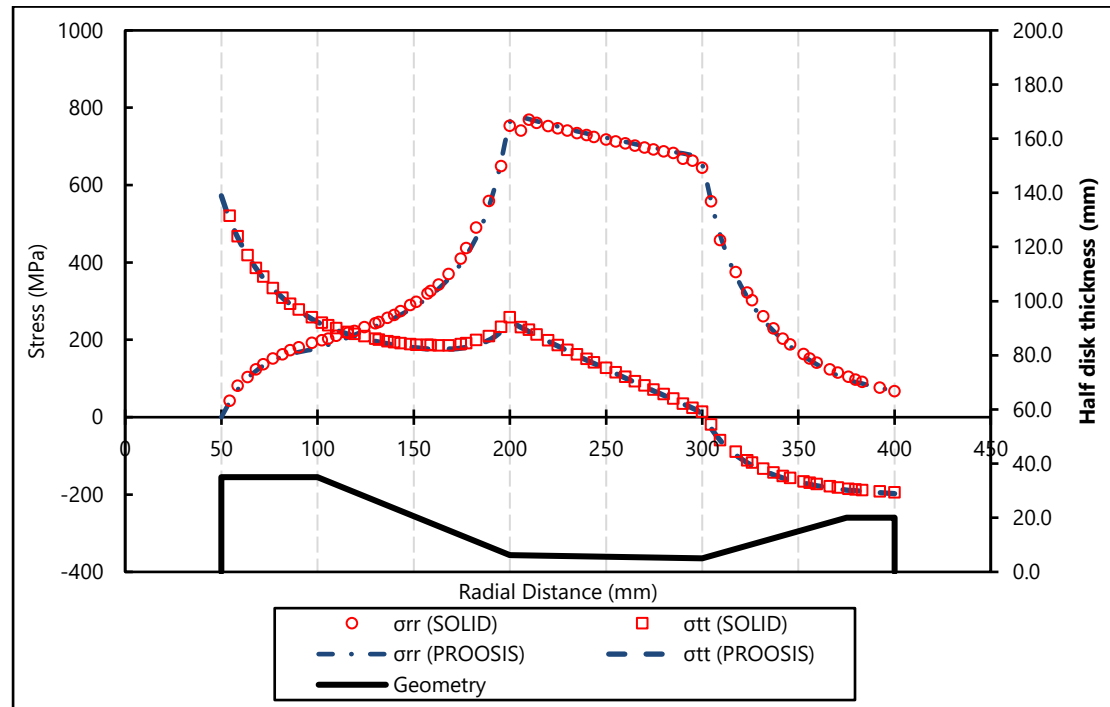


Figure 33: Comparison of the radial and tangential stresses as calculated by Solidworks and PROOSIS analyses on the disk described at Table 1 with temperature gradient, centrifugal load, rim load and zero bore load (Load case c).

### 5.3.5 Conclusions

It is worth mentioning that at any point Solidworks assigns the stress value of the closest node while probing the results. This means that solidworks points do not necessarily match with the algorithm nodes. Therefore, we need to interpolate solidworks results and match each radial distance with the equivalent proosis node in order to calculate the differences. This is executed with a simple MATLAB code which calculates the von Mises stress error as follows:

$$\sigma_{vM,error}(\%) = \frac{\sigma_{vM,solid,interpolated} - \sigma_{vM,proosis}}{\sigma_{vM,proosis}} \cdot 100$$

Table 8 shows the RMS of the calculated stress errors at every node for every validation case.

RMS of Von Mises stress errors (%)			
HPC E3 Stage Index	1	2	3
Load case a	0.983	1.903	1.480
Load case b	0.304	4.633	2.318
Turbine arbitrary disk			
Load case c	2.327		

Table 8: The RMS of von mises stress errors(%) for every validation case

It is concluded that the in plane-stress calculation modeled in PROOSIS can replace a much more time consuming FEA method without loss in accuracy. The PROOSIS model uses approximately one to two hundred nodes whereas a FEA method uses hundreds of thousands of nodes for a whole disk. The PROOSIS functions are used for the optimization algorithm, where time efficiency is very important since stress calculation is executed multiple times until convergence.

## 6. Optimization

### 6.1 Introduction

In this chapter the method that was developed for weight optimization is described. A function that calculates the disk weight is developed and validated by comparing the results with those from Solidworks evaluation tool. Subsequently, an experiment was set for the optimization of the first three stages disks of HPC NASA's/GE E3 engine. The selection of those three disks is convenient because they include all of the main disk types; Ring, Hyperbolic and Web respectively. Every disk is optimized with three different approaches: Lolis [9], Gasturb [5], Armand [1]. While the objective function and stress criteria are considered common, each case provides its own design variables, constraints and correlations between the dimensions. Nelder Mead Simplex algorithm is used for the optimization because it was available in PROOSIS, it can handle non continuous functions and does not require derivatives calculation. Upon the violation of every constraint a penalty value is added to the objective function.

### 6.2 Mass Calculating function

The mass of a disk is calculated by the formula [1]:

$$M = 2\pi\rho\sum_{j=1}^{j=5} [\frac{m_j}{3}(r_{j+1}^3 - r_j^3) + \frac{n_j}{2}(r_{j+1}^2 - r_j^2)] \quad (97)$$

A web type disk is divided in 5 parts as shown in Figure 4, the inner rim, the inner shoulder, the web, the outer shoulder and the outer rim. At each of these parts the thickness is a linear function of the radius :

$$t = m \cdot r + n \quad (98)$$

Thus, in a known geometry described by 6 thicknesses in 6 radial stations it can be deduced that:

$$\begin{aligned} m_j &= \frac{t_{j+1} - t_j}{r_{j+1} - r_j} \\ n_j &= t_j - \frac{t_{j+1} - t_j}{r_{j+1} - r_j} r_j \\ &\text{For } j=1,...,5 \end{aligned} \quad (99)$$

The equation for mass calculation is used for ring and web as well as hyperbolic type disks, since in the weight optimization we assume that all six geometry defining points are connected through a straight line.

The PROOSIS function that calculates the disk weight is WKG\_diskW\_ARMAND\_MOD().The inputs of the function are:

<b>istg:</b>	The number of the stage. It is used for naming the file with the results
<b>compINSTANCE_NAME:</b>	The name of the engine. It is used for naming the file with the results
<b>material:</b>	Disk Material
<b>nrs:</b>	Number of disk radial segments
<b>R[nrs+1]:</b>	Disk radius at nrs+1 radial stations
<b>t[nrs+1]:</b>	Disk thickness at nrs+1 radial stations
<b>dsf_in[nrs]:</b>	User-defined thickness form factor for the nrs radial segments

For a ring disk nrs=1 , for web or hyperbolic disk nrs=5.

The output is the weight **WKG**

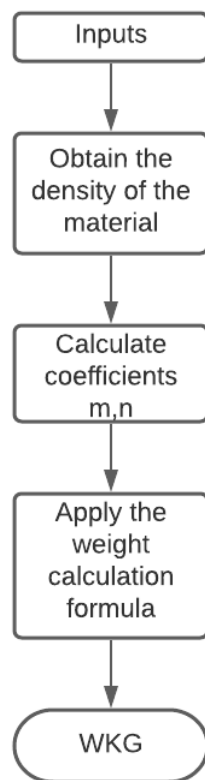


Figure 34: Workflow of weight calculation function WKG\_diskW\_ARMAND\_MOD.

### 6.3 Optimization problem construction

The initial geometries are those of the three first disks of NASA's/GE E3 engine HPC, which are summarized in Table 2. The rim radius and thickness ( $r_6$  and  $t_6$ ) are always fixed. The rim thickness should be equal to the axial component of the chord of the blade. The rim radius should be equal to the airfoil hub radius minus the height of the blade root. Blade root includes platform, neck if existing and fir-tree.

$$t_6 = c_{bl,ax} \quad (100)$$

$$r_6 = r_{airfoil\ hub} - h_{blade\ root} \quad (101)$$

The stress criteria for the disk structural integrity require the average tangential stress calculated at +120% overspeed to be lower than or equal to 0.9 times the ultimate material strength at the disk average temperature. Additionally, the maximum von mises stress should be lower than or equal to the yield strength at the maximum temperature (thus the minimum yield strength) divided by the safety factor 1.1 [1] :

$$\sigma_{\theta,avg_{120}} \leq 0.9\sigma_{UTS,at\ avg T} \Rightarrow RBM_{120} = \frac{\sigma_{\theta,avg_{120}}}{0.9\sigma_{UTS}} \leq 1 \quad (102)$$

$$\sigma_{vonMises,max} \leq \frac{\sigma_{Y,min}}{1.1} \Rightarrow RDM = \frac{\sigma_{vonMises,max}}{\frac{\sigma_y}{1.1}} \leq 1 \quad (103)$$

To include the case where some tangential stresses are negative their average is calculated by the formula:

$$\sigma_{\theta,avg} = \sqrt{\frac{1}{N} \sum_{i=1}^N \sigma_{\theta i}^2}$$

Where N is the number of nodes.

In structural problems the weight reduction is equivalent to stress maximizing. Consequently, the objective function is formed in a way that its minimization results in maximum stresses. Optimal geometry is obtained by Nelder Mead Simplex method, which does not require the calculation of derivatives and is suitable for discontinuous functions. Thus, we set the objective function as:

$$F = \frac{1}{2}(\max[RDM, RBM] - 1)^2 \quad (104)$$

Constraints that apply to every case is that the mass of the disk should be above zero, and the bore radius should be above 1.1 time the maximum shaft radius:

$$M > 0 \quad (105)$$

$$r_1 > 1.1r_{shaft,max} \quad (106)$$

## 6.4 Implementation of optimization in PROOSIS

Prior to optimization experiment some useful functions are created:

- Function **t\_vs\_R()** returns the disk thickness for an input radial station.
- Function **discrDiskGeom()** discretizes the input disk geometry based on the input number of nodes Nd
- Function **ObtainBoundLoad()** calculates the boundary loads by the dead weight centrifugal forces
- Function **getMtr\_vs\_T()** obtains all the necessary material properties at every node according to the temperature at every node
- Function **initGeom()** initializes the geometry using the stage index as an input. Depending on the stage index it obtains the appropriate dimensions from the table that summarizes the geometry of all 3 disks.
- Function **updateGeom()** updates the disk geometry based on the current values of the design parameters.
- Function **OBJ\_FCN()** calculates the objective function value by running stress analysis and adding penalty values if any constraint is violated.
- Function **runOptim()** takes the objective function value as an input and calls the Simplex method.

The declarations of the experiment are used as inputs for the procedure. These inputs are the stage index, the optimization approach (Lolis,Gasturb,Armand), the temperature profile calculation type (constant temperature, numerical or analytical Fourier solution or input temperature profile), the inclusion of thermal effects or not and the safety factors used at the stress criteria. In the HPC E3 optimization the temperature was chosen to be constant and equal to the rim temperature.

Figure 35 shows a workflow diagram that represents the whole optimization procedure as executed in the experiment.



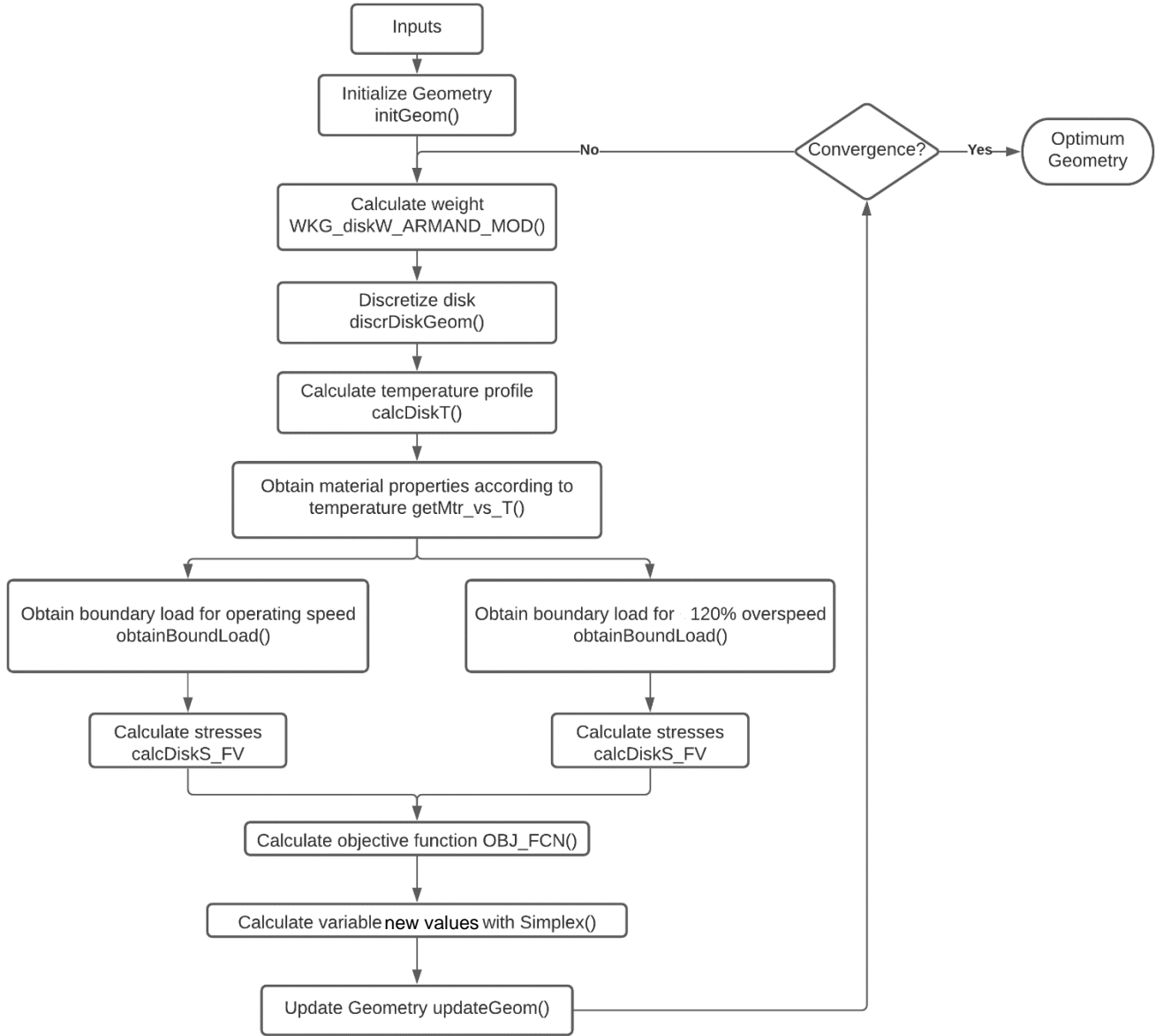


Figure 35: The Workflow of optimization experiment

In the following subchapters the results for every case of optimization are presented.

## 6.5 E3 HPC 1<sup>st</sup> stage optimization

Due to the simplicity of the geometry no different cases can be implemented and the problem is constructed as referred to Lolis [9]. Disk geometry is fully described by its rim radius, bore radius and its constant thickness. Since the rim radius and thickness are fixed for the attachment of the blade, there is only one unknown variable :  $r_1$

The following correlations are applied:

$$t_1 = t_2 = t_3 = t_4 = t_5 = t_6 = c_{bl,ax} \quad (107)$$

$$r_i = r_1 + (i - 1) \cdot \frac{r_6 - r_1}{5} \text{ for } i = 2, \dots, 5 \quad (108)$$

The results of the optimization of the 1<sup>st</sup> stage ring disk are presented in Table 9:

Weights		
Initial weight (kg)	Optimal weight (kg)	Difference (%)
16.806	10.218	-39.2
Initial Geometry		
	Bore	Rim
r(m)	0.1041	0.1546
t(m)	0.0937	0.0937
Optimum Geometry		
	Bore	Rim
r(m)	0.1263	0.1546
t(m)	0.0937	0.0937
Stress ratios		
	Initial	Optimum
RBM_120	0.630805	1
RDM	0.596673	0.862939

Table 9: Results of 1st stage HPC E3 optimization

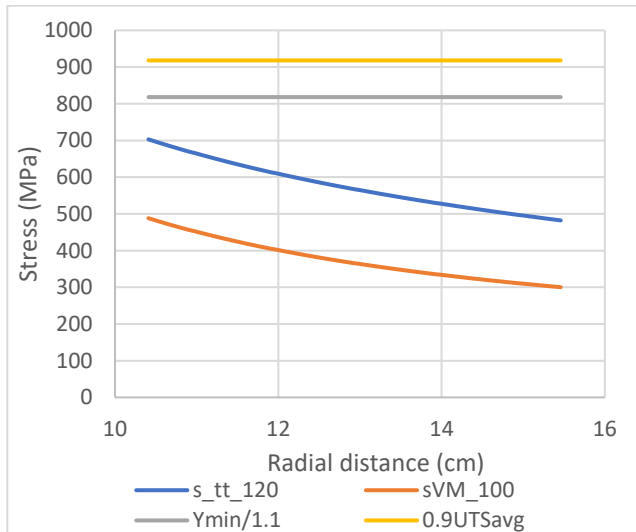


Figure 36: Stresses at the initial disk of the 1<sup>st</sup> stage of E3 HPC. Von Mises stress calculated at 100% speed and tangential stress calculated at 120% speed, compared with their maximum limits yield strength/1.1 and 0.9\*ultimate strength.

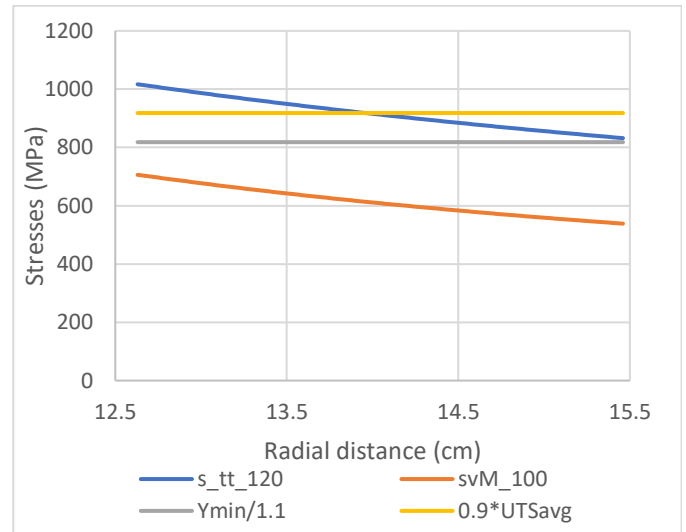


Figure 37: Stresses at the optimal geometry of 1st stage disk of HPC E3. It is shown that the maximum stress criterion has reached its limits.

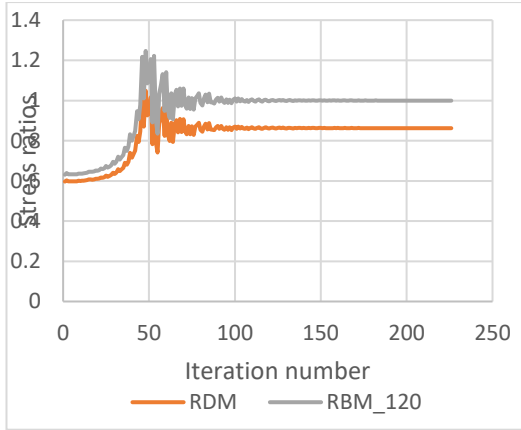


Figure 38 : Convergence of the stress ratios for 1<sup>st</sup> stage disk.

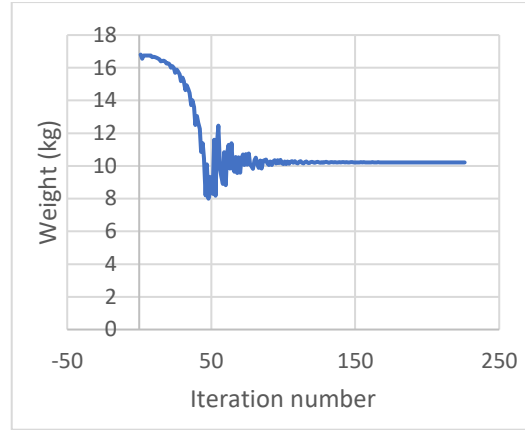


Figure 39: Weight convergence of the 1st stage disk

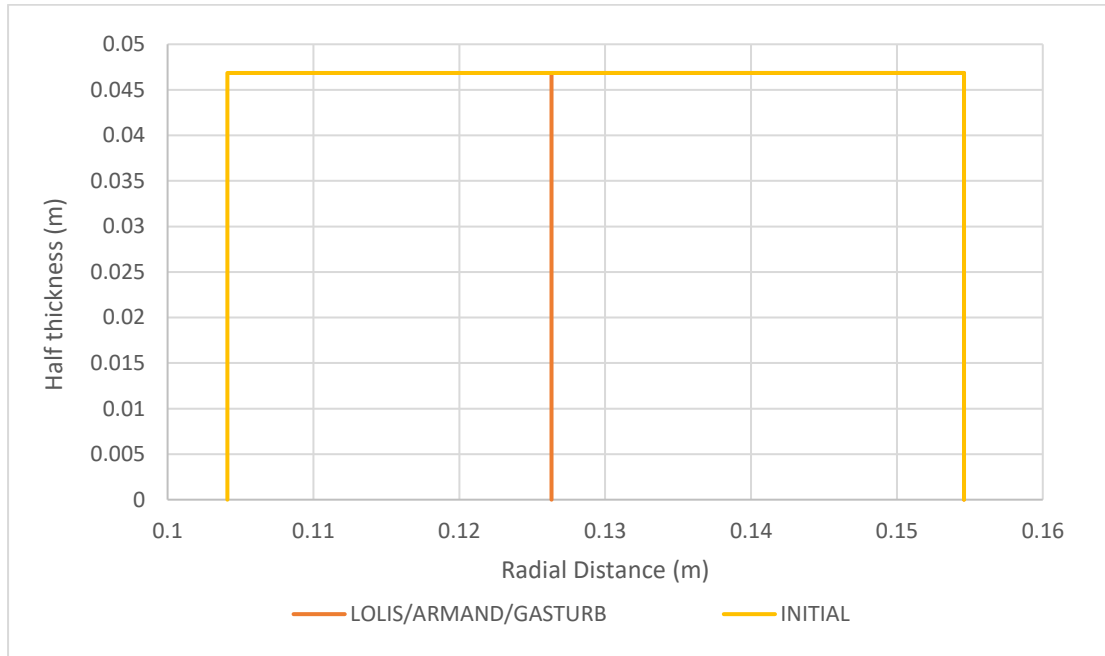


Figure 40: Initial and optimum 1<sup>st</sup> stage disk semi-contours for comparison. It is obvious that the disk weight is reduced since the bore radius is increased.

## 6.6 E3 HPC 2<sup>nd</sup> stage optimization

The second stage disk is a hyperbolic type. The disk geometry is fully described by 12 variables. However, the rim radius and thickness is fixed and the outer and inner rim have constant thickness. Thus:

$$r_6 = r_{rim}$$

$$t_6 = t_{rim}$$

$$t_5 = t_6$$

$$t_1 = t_2$$

The remaining 8 variables are independent and will be handled differently according to each approach.

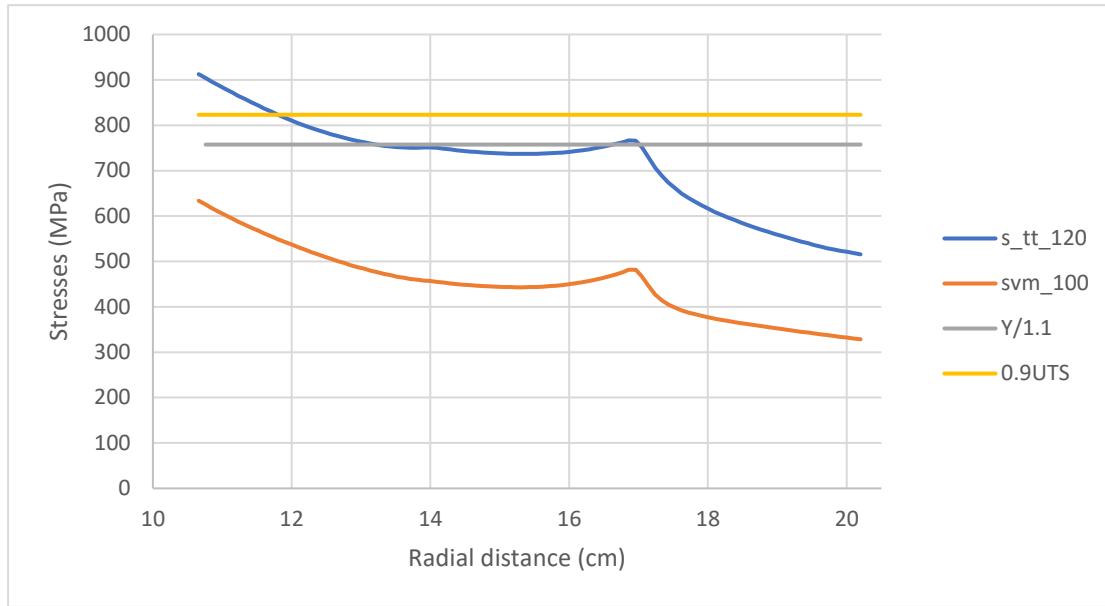


Figure 41: HPC E3 2nd stage initial stresses indicate that they can be further increased.

### 6.6.1 Lolis approach

From the 8 independent variables this approach chooses the following as design variables and keeps the rest constant and equal to initial

Design variables:  $r_1, r_2, t_2, t_4$

There are additional constraints due to spacing. For each of them that is violated a penalty value is added to the objective function:

$$r_2 \geq 1.1 \cdot r_1 \quad (109)$$

$$r_4 \geq 1.1 \cdot r_3 \quad (110)$$

$$1.5 \cdot t_4 \leq t_2 \leq 2 \cdot t_6 \quad (111)$$

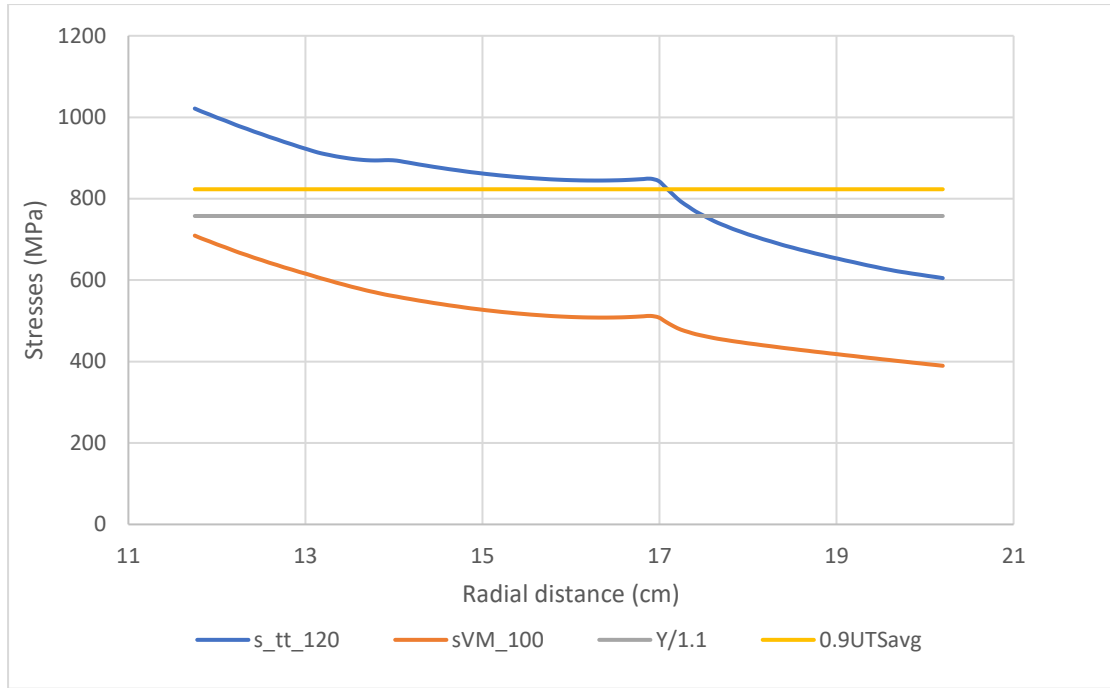


Figure 42: Stresses at the optimal geometry of 2<sup>nd</sup> stage disk of HPC E3 according to Lolis. The stresses have reached their limits

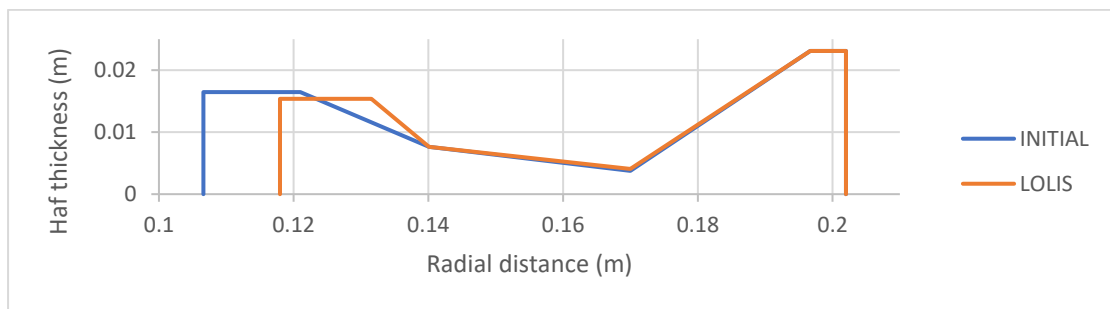


Figure 43: Comparison of 2nd stage HPC E3 initial and optimal geometry according to Lolis. It is obvious that the new disk geometry is of lower weight.

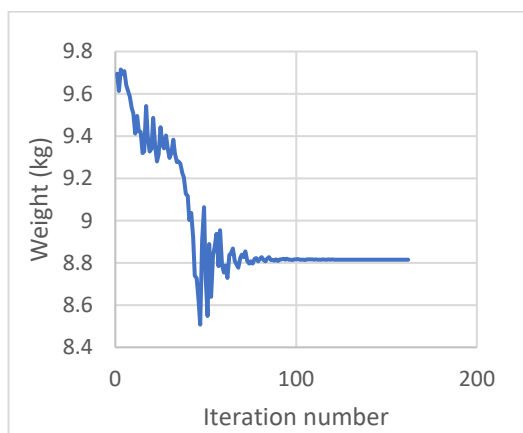


Figure 44: Weight convergence for 2nd stage disk ,Lolis approach

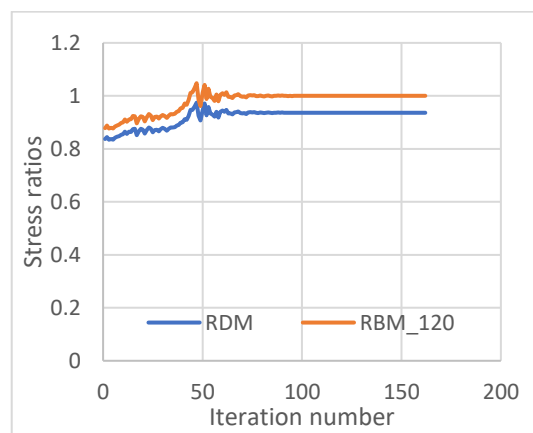


Figure 45: Stress convergence for 2nd stage disk Lolis approach

### 6.6.2 Gasturb approach

From the 8 independent variables this approach chooses the following 6 as design variables and keeps the rest constant and equal to initial:

Design variables:  $r_1, r_2, r_5, t_1, t_3, t_4$

The geometric constraints are the following. For each of them that is violated a penalty value is added to the objective function:

$$0.1 \leq \frac{r_6 - r_5}{t_6} \leq 1 \quad (112)$$

$$0.15 \leq \frac{t_3}{t_6} \leq 1 \quad (113)$$

$$0.2 \leq \frac{r_2 - r_1}{t_6} \leq 1 \quad (114)$$

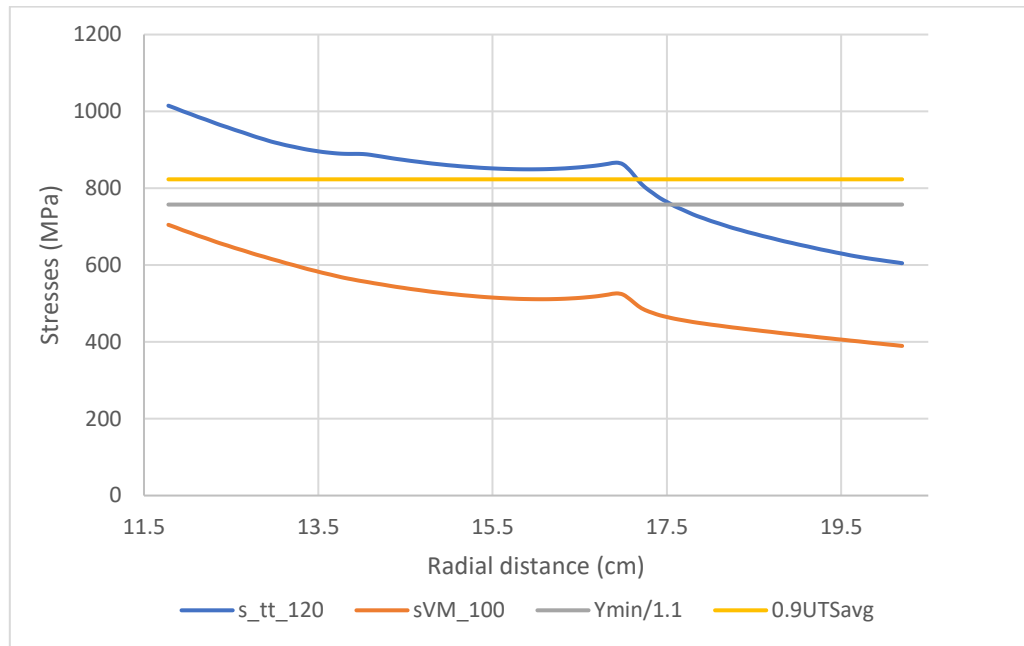


Figure 46: Stresses at the optimal geometry of 2<sup>nd</sup> stage disk of HPC E3 according to Gasturb. The stresses have reached their limits

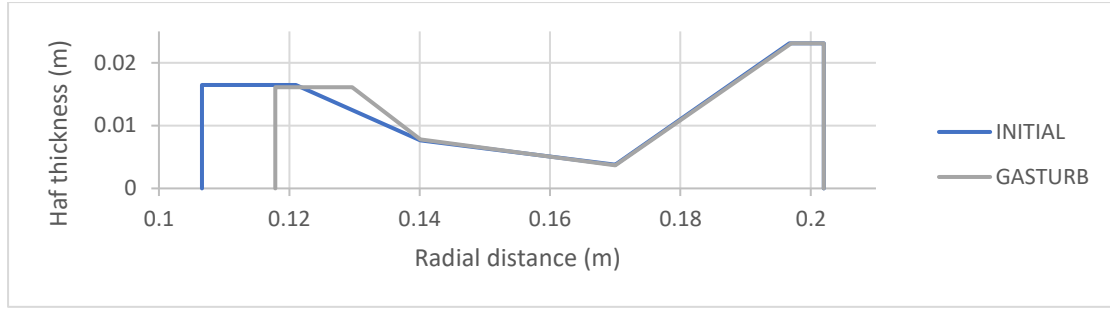


Figure 47: Comparison of 2nd stage HPC E3 initial and optimal geometry according to Gasturb. It is obvious that the new disk geometry is of lower weight.

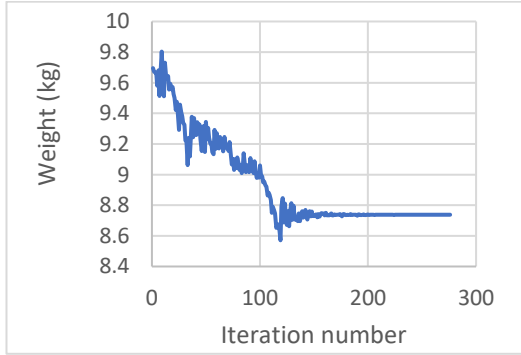


Figure 48: Weight convergence for 2nd stage disk Gasturb approach

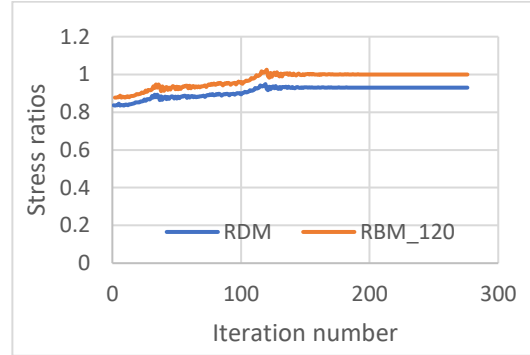


Figure 49: Stresses convergence for 2nd stage disk Gasturb approach

### 6.6.3 Armand approach

From the 8 independent variables this approach chooses the following 7 as design variables and keeps the rest constant and equal to initial:

Design variables:  $r_1, r_2, r_3, r_4, t_1, t_3, t_4$

The additional geometric constraints are:

$$r_2 - r_1 > 0 \quad (115)$$

$$r_3 - r_2 > 0 \quad (116)$$

$$r_4 - r_3 > 0 \quad (117)$$

$$r_5 - r_4 > 0 \quad (118)$$

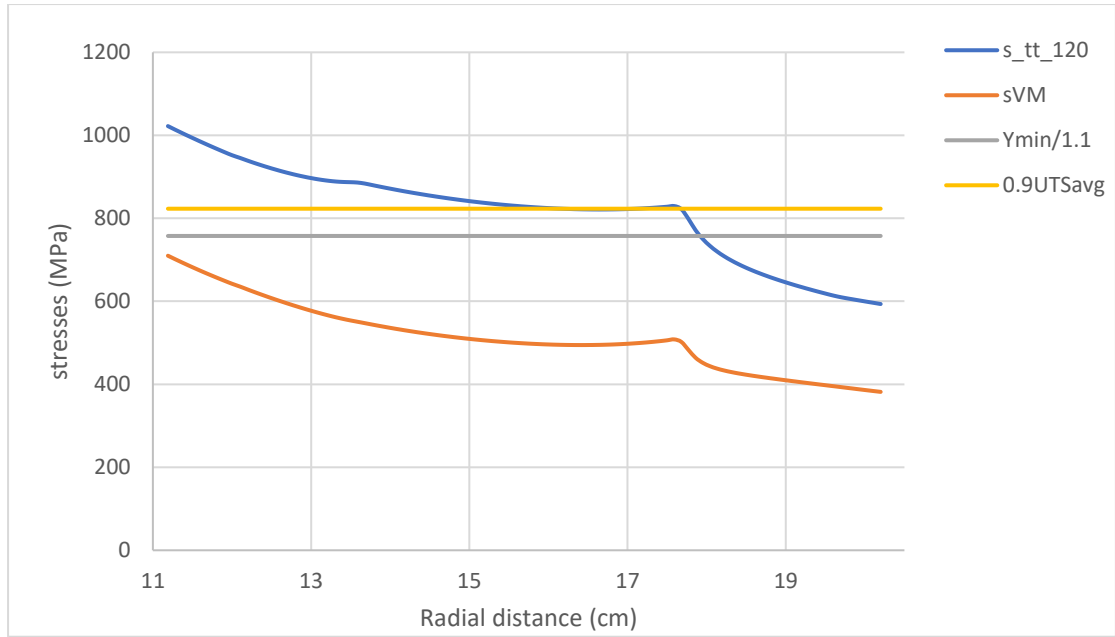


Figure 50: Stresses at the optimal geometry of 2<sup>nd</sup> stage disk of HPC E3 according to Armand. The stresses have reached their limits

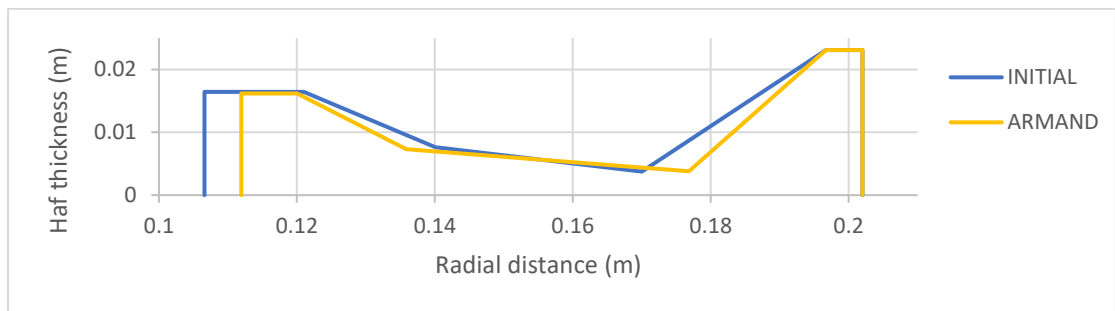


Figure 51: Comparison of 2nd stage HPC E3 initial and optimal geometry according to Armand. It is obvious that the new disk geometry is of lower weight.

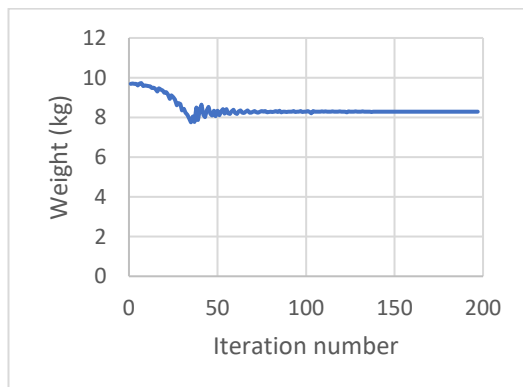


Figure 52: Weight convergence of 2nd stage disk Armand approach

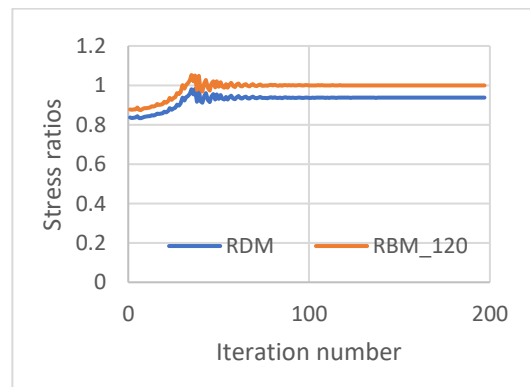


Figure 53: Stresses convergence of 2nd stage disk Armand approach



#### 6.6.4 Table of optimization results for 2<sup>nd</sup> stage

The results are presented in the following Table 10 :

Stage 2					Initial weight (kg) : 9.695			
Weight results								
Approach			Optimal weight (kg)			Difference (%)		
Lolis			8.815			-9.08		
Gasturb			8.738			-9.87		
Armand			8.289			-14.5		
Geometry								
Initial			Lolis		Gasturb		Armand	
	r(m)	t(m)	r(m)	t(m)	r(m)	t(m)	r(m)	t(m)
1	0.1066	0.0329	0.1180	0.0307	0.1179	0.0322	0.1119	0.0323
2	0.121	0.0329	0.13156	0.0307	0.1296	0.0322	0.1200	0.0323
3	0.1401	0.0153	0.1401	0.0153	0.1401	0.0156	0.1359	0.0147
4	0.17	0.0075	0.1700	0.0082	0.1700	0.0073	0.1768	0.0076
5	0.1967	0.0462	0.1967	0.0462	0.1970	0.0462	0.1967	0.0462
6	0.202	0.0462	0.202	0.0462	0.2020	0.0462	0.2020	0.0462
Stress ratios								
		Lolis			Gasturb		Armand	
RBM_120		1			1		1	
RDM		0.9364			0.9304		0.9372	

Table 10 : Summarization of the results of 2<sup>nd</sup> stage of HPC E3 optimization

#### 6.7 E3 3<sup>rd</sup> stage optimization

The third stage disk is a web type. The disk geometry is fully described by 12 variables. However, the rim radius and thickness is fixed and the outer rim, inner rim and web have constant thickness. Thus:

$$r_6 = r_{rim}$$

$$t_6 = t_{rim}$$

$$t_5 = t_6$$

$$t_1 = t_2$$

$$t_3 = t_4$$

The remaining 7 variables are independent and will be handled differently according to the approach.

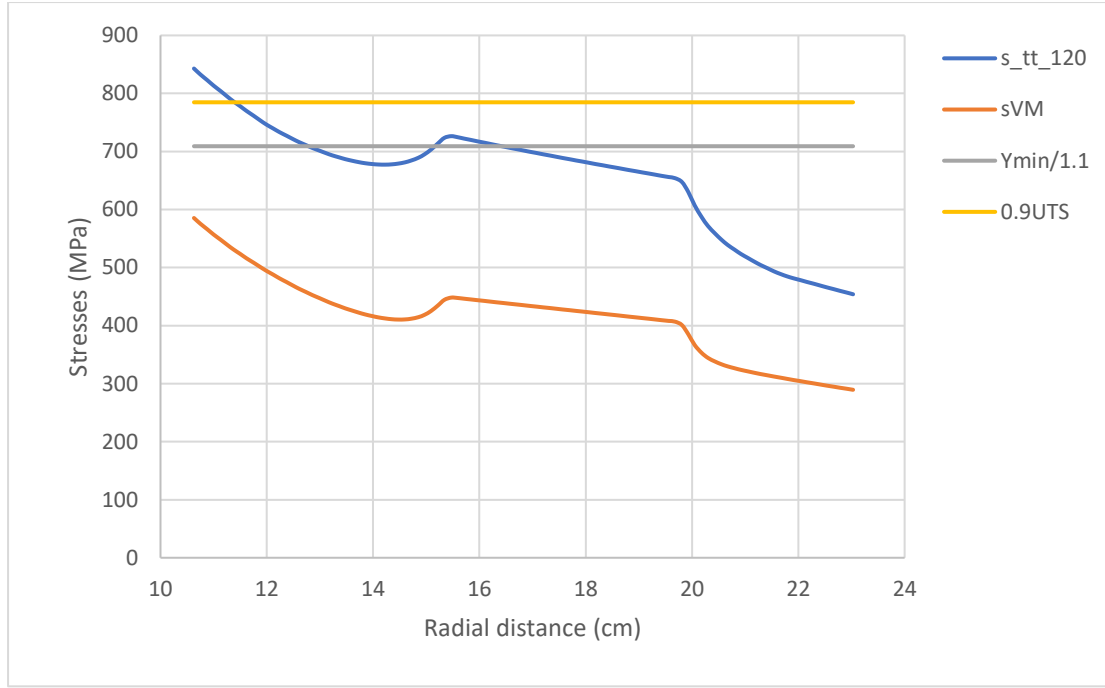


Figure 54: HPC E3 3<sup>rd</sup> stage initial stresses indicate that they can be further increased.

### 6.7.1 Lolis approach

From the 7 independent variables this approach chooses the following 4 as design variables:

Design variables:  $r_1, r_2, t_1, t_3$

Two correlations are added since the shoulder angles are kept constant. The following formulas are used in geometry update:

$$r_3 = r_2 + \frac{t_2 - t_3}{2 \tan\left(\frac{\pi}{5}\right)}$$

$$r_4 = r_5 - \frac{t_5 - t_4}{2 \tan\left(\frac{\pi}{5}\right)}$$

The one remaining variable  $r_5$  is kept equal to initial.

There are additional constraints due to spacing. For each of them that is violated a penalty value is added to the objective function:

$$r_2 \geq 1.1 \cdot r_1$$

$$r_4 \geq 1.1 \cdot r_3$$

$$1.5 \cdot t_4 \leq t_2 \leq 2 \cdot t_6$$

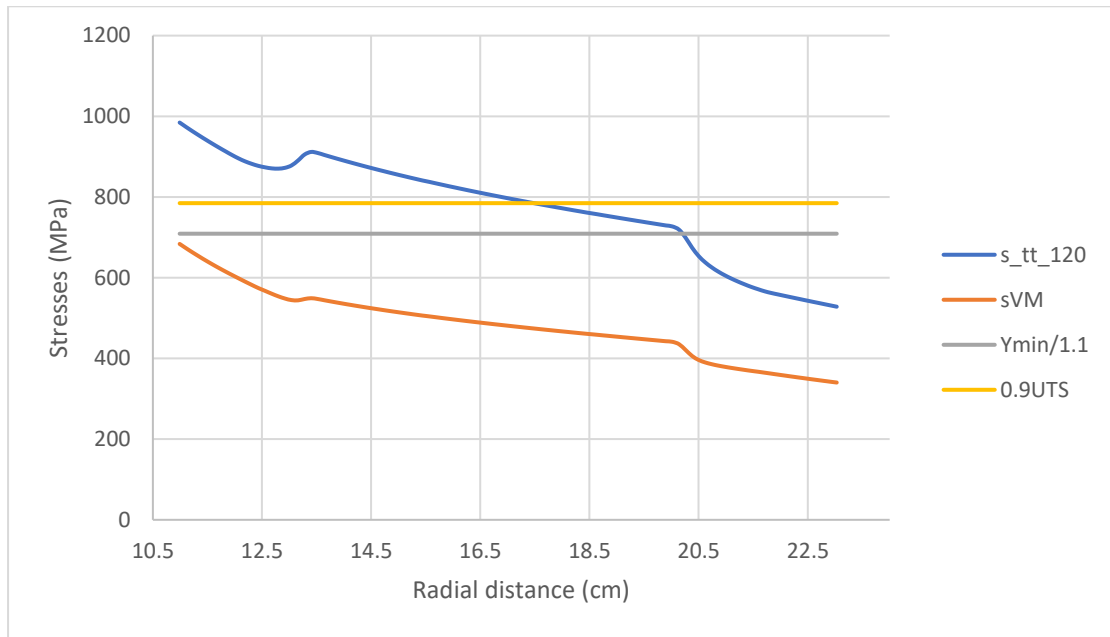


Figure 55: Stresses at the optimal geometry of 3<sup>rd</sup> stage disk of HPC E3 according to Lolis. The stresses have reached their limits

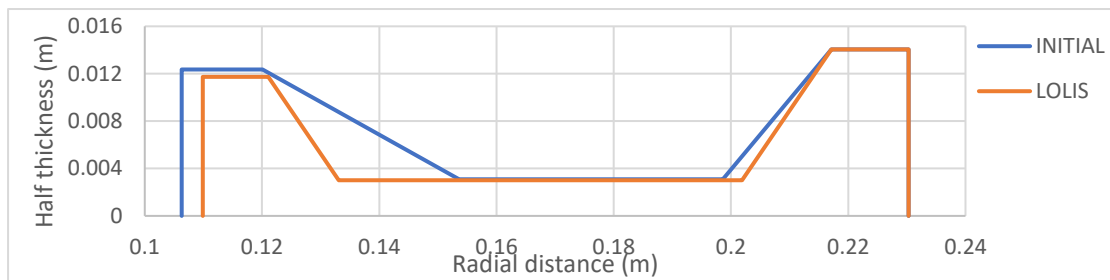


Figure 56: Comparison of 3<sup>rd</sup> stage HPC E3 initial and optimal geometry according to Lolis. It is obvious that the new disk geometry is of lower weight.

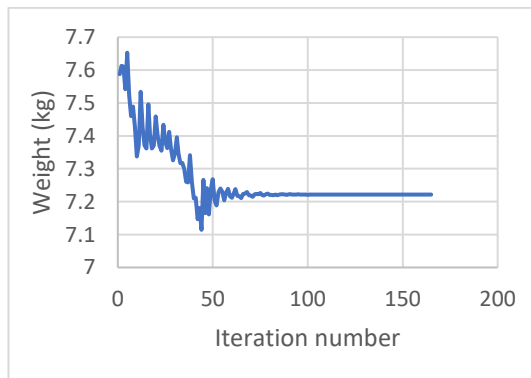


Figure 57: Weight convergence for 3rd stage disk Lolis approach

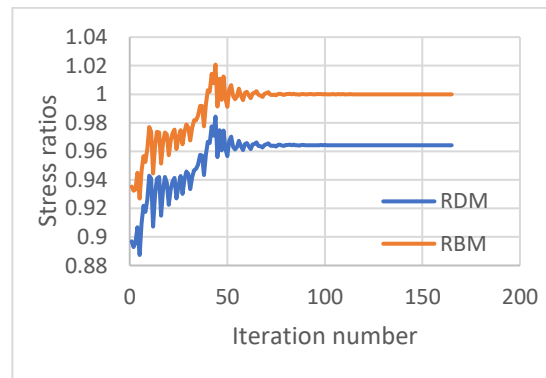


Figure 58: Weight convergence for 3rd stage disk Lolis approach

## 6.7.2 Gasturb approach

From the 7 independent variables this approach chooses the following 5 as design variables:

Design variables:  $r_1, r_2, r_5, t_1, t_3$

The two remaining dimensions are calculated by correlations. Gasturb keeps the shoulder angles constant. Thus, the following formulas are used in geometry update:

$$r_3 = r_2 + \frac{t_2 - t_3}{2 \tan\left(\frac{\pi}{6}\right)}$$

$$r_4 = r_5 - \frac{t_5 - t_4}{2 \tan\left(\frac{\pi}{3}\right)}$$

The geometric constraints are:

$$0.1 \leq \frac{r_6 - r_5}{t_6} \leq 1$$

$$0.15 \leq \frac{t_3}{t_6} \leq 1$$

$$0.2 \leq \frac{r_2 - r_1}{t_6} \leq 1$$

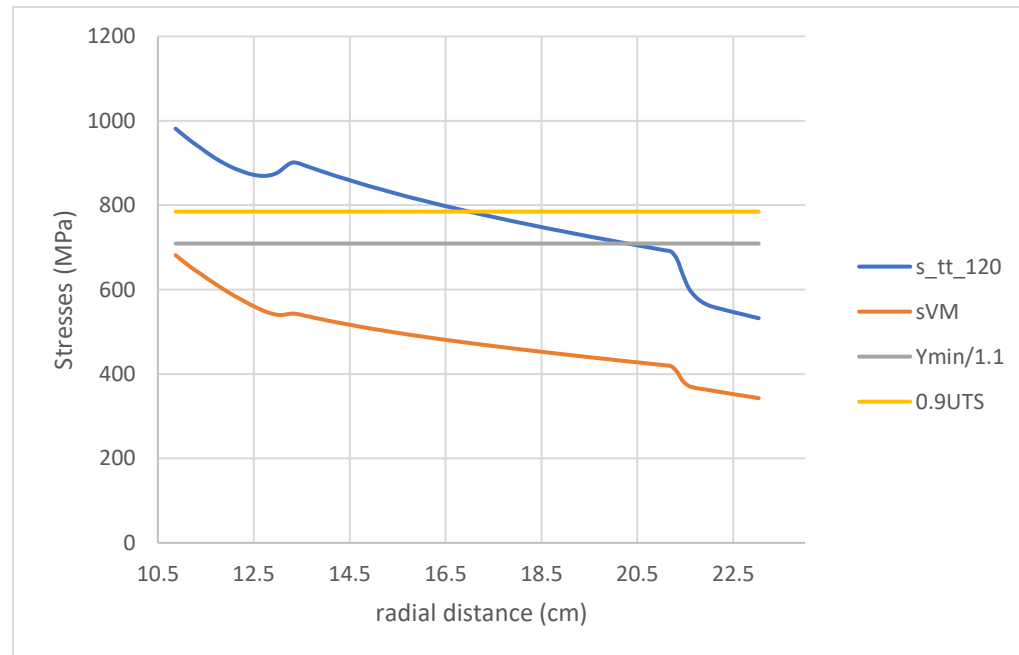


Figure 59: Stresses at the optimal geometry of 3<sup>rd</sup> stage disk of HPC E3 according to Gasturb. The stresses have reached their limits

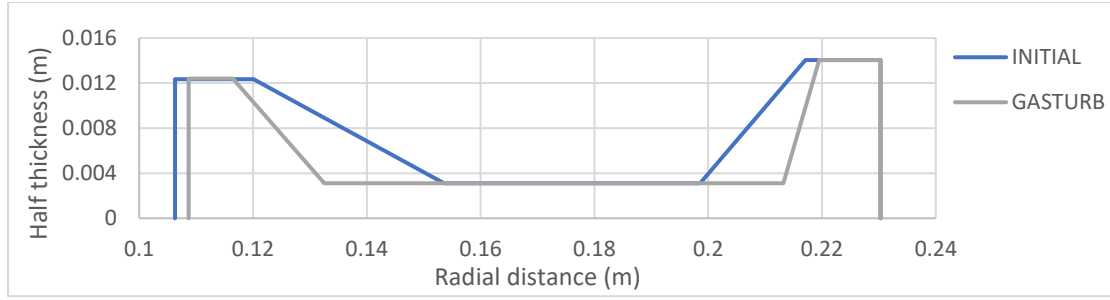


Figure 60: Comparison of 3<sup>rd</sup> stage HPC E3 initial and optimal geometry according to Gasturb. It is obvious that the new disk geometry is of lower weight.

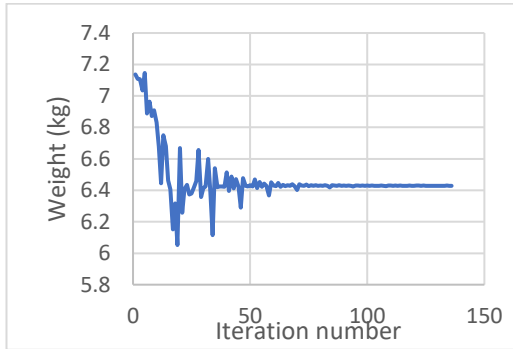


Figure 61: Weight convergence for 3rd stage disk Gasturb approach

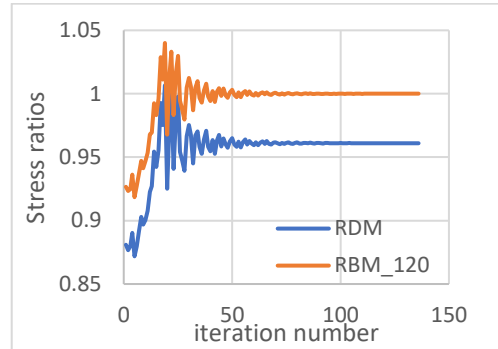


Figure 62: Stresses convergence for 3rd stage disk Gasturb approach

### 6.7.3 Armand approach

From the 7 independent variables this approach chooses the following 6 as design variables:

Design variables:  $r_1, r_2, r_3, r_4, t_1, t_3$

The one remaining variable  $r_5$  is kept equal to the initial one.

The additional geometric constraints are:

$$r_2 - r_1 > 0$$

$$r_3 - r_2 > 0$$

$$r_4 - r_3 > 0$$

$$r_5 - r_4 > 0$$

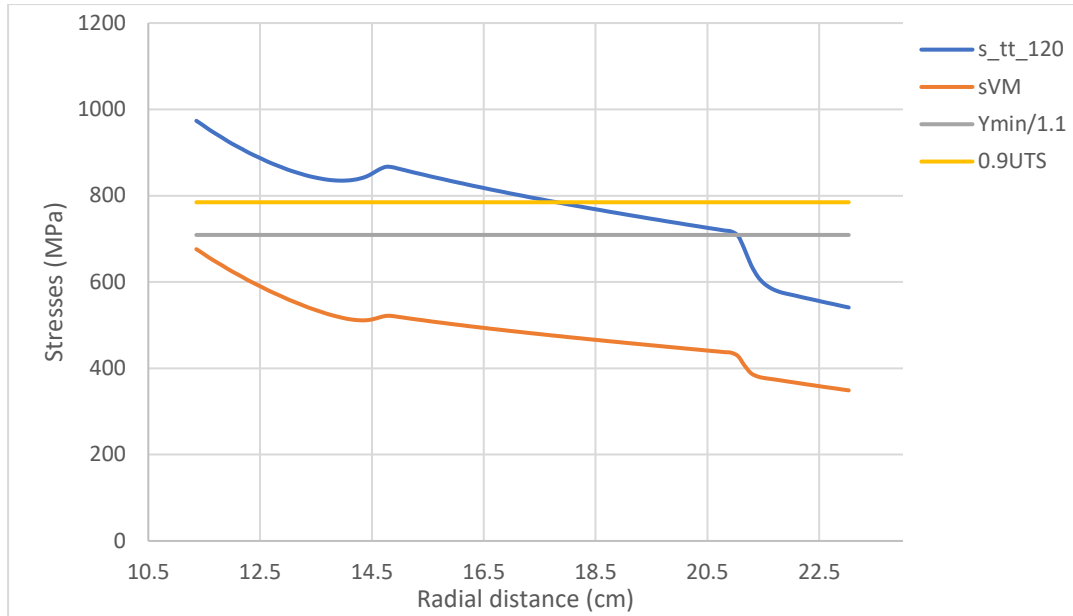


Figure 63: Stresses at the optimal geometry of 3<sup>rd</sup> stage disk of HPC E3 according to Armand. The stresses have reached their limits.

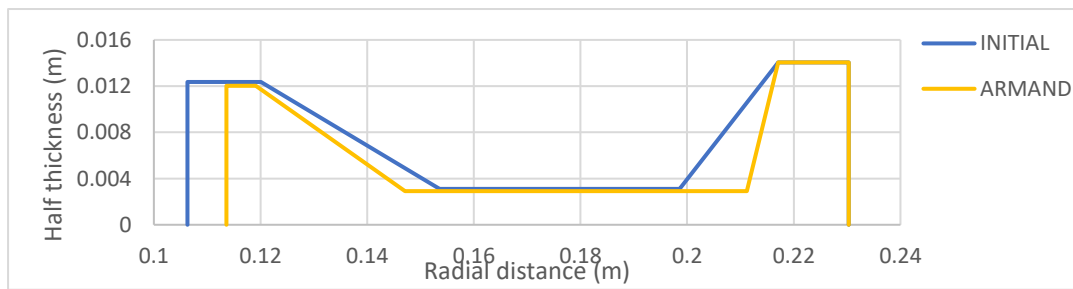


Figure 64: Comparison of 3<sup>rd</sup> stage HPC E3 initial and optimal geometry according to Armand. It is obvious that the new disk geometry is of lower weight.

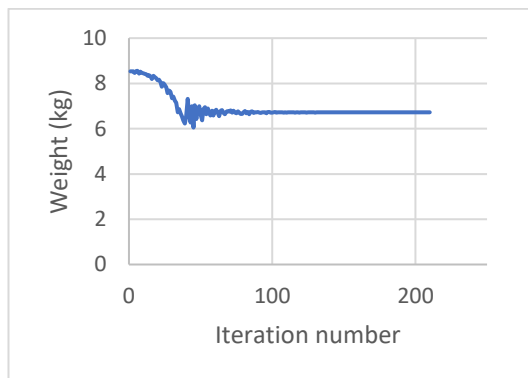


Figure 65: Weight convergence for 3rd stage disk Armand approach

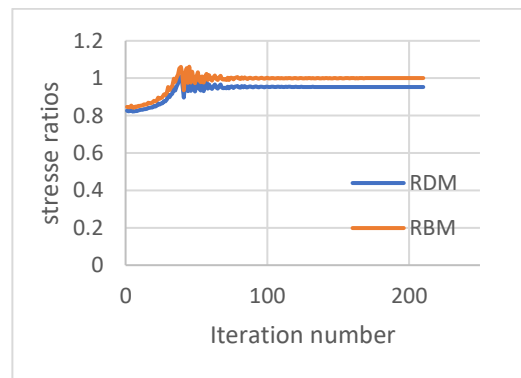


Figure 66: Stresses convergence for 3rd stage disk Armand approach

## 6.7.4 Table of optimization results for 3<sup>rd</sup> stage

The results are presented in the following Table 11 :

Stage 3					Initial weight (kg) : 8.527			
Weight results								
Approach			Optimal weight (kg)			Difference (%)		
Lolis			7.222			-15.3		
Gasturb			6.429			-24.6		
Armand			6.72			-21.2		
Geometry								
Initial			Lolis		Gasturb		Armand	
	r(m)	t(m)	r(m)	t(m)	r(m)	t(m)	r(m)	t(m)
1	0.1063	0.0247	0.1099	0.0235	0.1087	0.0248	0.1136	0.0240
2	0.1201	0.0247	0.1211	0.0235	0.1165	0.0248	0.1191	0.0240
3	0.1536	0.0062	0.1331	0.006	0.1325	0.0062	0.1471	0.0058
4	0.1986	0.0062	0.2019	0.006	0.2132	0.0062	0.2112	0.0058
5	0.2171	0.0281	0.2171	0.0281	0.2195	0.0281	0.2171	0.0281
6	0.2303	0.0281	0.2303	0.0281	0.2303	0.0281	0.2303	0.0281
Optimum Stress ratios								
		Lolis			Gasturb		Armand	
RBM_120		1			1		1	
RDM		0.9643			0.9610		0.9534	

Table 11 : Summarization of the results of HPC E3 3<sup>rd</sup> stage optimization

## 6.8 Validation with “Gasturb Details 5”

### 6.8.1 Stress validation

Prior to optimization validation, a stress validation was executed in order to ensure that Gasturb Software calculates the stresses the same way PROOSIS function does. The Gasturb Demo Disk, the default file of “Gasturb Details 5” was used for this analysis. The same geometry and boundary conditions of were inserted in PROOSIS and the stresses were calculated. The blades were considered unshrouded and the temperature constant throughout the disk and equal to 823.15 K.

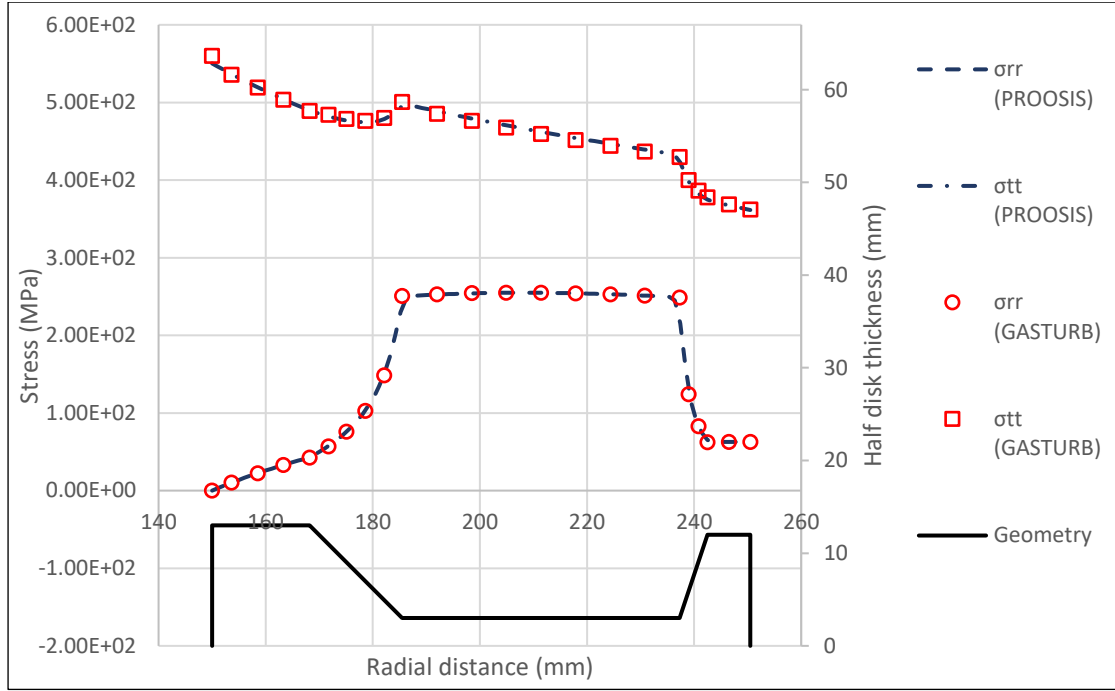


Figure 67: Comparison of stress results from Gasturb Details 5 and PROOSIS. The disk analyzed is the Demo disk that opens with Gasturb Software as a default.

It is deduced that the stress results are very close so we can continue with comparing the optimization results.

## 6.8.2 Optimization verification

An optimization case was run with PROOSIS experiment and Gasturb Software in order to compare the results. The optimization was constructed according to the following conditions that were applied at both studies to ensure that the problem is the same.

Initial geometry is the default Demo disk that comes with the Software. The geometry, material and constant temperature are summarized in Table 12.

Radial Stations	1	2	3	4	5	6
r (mm)	150	168.2	185.5	237.3	242.5	250.5
t(mm)	26	26	6	6	24	24
Material	INCONEL 718					
Temperature (K)	823.15					

Table 12 : Gasturb Demo disk geometry



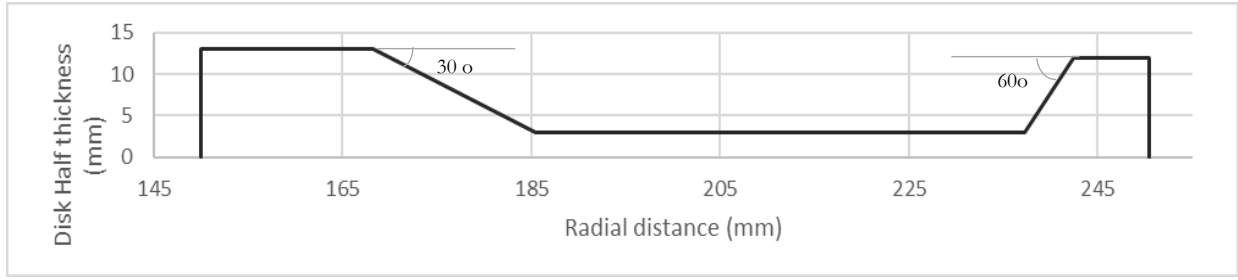


Figure 68: Demo Disk semi-contour

The bore boundary stress is zero, the rim boundary condition is calculated as the dead weight centrifugal load as indicated in Table 13.

Number of blades (nb)	103
Dead weight per blade (kg)	0.1118
Radius of dead weight center of gravity (m)	0.346895
Rotational speed (rpm)	7350
Rim stress (MPa)	62.665

Table 13: Demo disk rim load calculation

The following three design variables are chosen. The rest disk dimensions are considered constant and equal to the initial

$$x_1 = \frac{t_3}{t_6}$$

$$x_2 = \frac{r_2 - r_1}{t_6}$$

$$x_3 = \frac{r_6 - r_5}{t_6}$$

The initial values of the design variables are:

$$X = \{x_1, x_2, x_3\} = \{0.25, 0.7583, 0.3333\}$$

The geometrical constraints are :

$$0.15 \leq x_1 \leq 1$$

$$0.2 \leq x_2 \leq 1$$

$$0.1 \leq x_3 \leq 1$$

Gasturb assumes constant angle in the shoulders of the disk; 30° for the inner shoulder and 60° for the outer shoulder. This means that the following equations should be used for the update of the geometry in PROOSIS:

$$r_3 = r_2 + \frac{t_2 - t_3}{2 \tan\left(\frac{\pi}{6}\right)}$$

$$r_4 = r_5 - \frac{t_5 - t_4}{2 \tan\left(\frac{\pi}{3}\right)}$$

The disk is web type and the blades are considered unshrouded. Stress criteria are put as constraints. In Gasturb there are two main stress criteria:

$$BM(\%) = \left( \frac{\text{Burst Margin}}{0.47 \cdot \sigma_{UTS,at\ avg\ T}} - 1 \right) \cdot 100 \quad (119)$$

$$DM(\%) = \left( \frac{\text{Stress Margin}}{\sigma_Y} - 1 \right) \cdot 100 \quad (120)$$

Generally, the stress margin is local, it should be calculated in every node and the minimum of all resulting values should be kept as critical. In this particular optimization case, the temperature is constant throughout the nodes and so is the yield strength. Therefore, the minimum stress margin is expressed as in equation (120) .

In PROOSIS algorithm the stress criteria are expressed as:

$$RBM = \frac{\sigma_{\theta,avg}}{\sigma_{UTS,at\ avg\ T}} \quad (121)$$

$$RDM = \frac{\sigma_{von\ Mises,max}}{\sigma_Y} \quad (122)$$

Substituting equations in we get

$$BM = \left( 0.47 \frac{1}{RBM} - 1 \right) \cdot 100 \Rightarrow$$

$$RBM = \frac{0.47}{\frac{BM}{100} + 1} \quad (123)$$

$$DM = \left( \frac{1}{RDM} - 1 \right) \cdot 100 \Rightarrow$$

$$RDM = \frac{1}{\frac{DM}{100} + 1} \quad (124)$$

Gasturb suggests that the margins should be :

$$BM, DM \geq 10$$

Substituting in equations we get the stress constraints for the PROOSIS algorithm:

$$RBM \leq 0.4273$$

$$RDM \leq 0.91$$

The results of both methods are shown in Table 14 :

Initial weight = 13.2 kg	
GASTURB	
Optimal weight (kg)	9.84
RBM	0.4273
RDM	0.5714
X=[x1,x2,x3]	[0.15 , 0.6329 , 0.1]
PROOSIS	
Optimal weight (kg)	10.19
RBM	0.4273
RDM	0.5658
X=[x1,x2,x3]	[0.15 , 0.591 , 0.191]

Table 14: comparison of optimization results from Gasturb Details 5 and PROOSIS

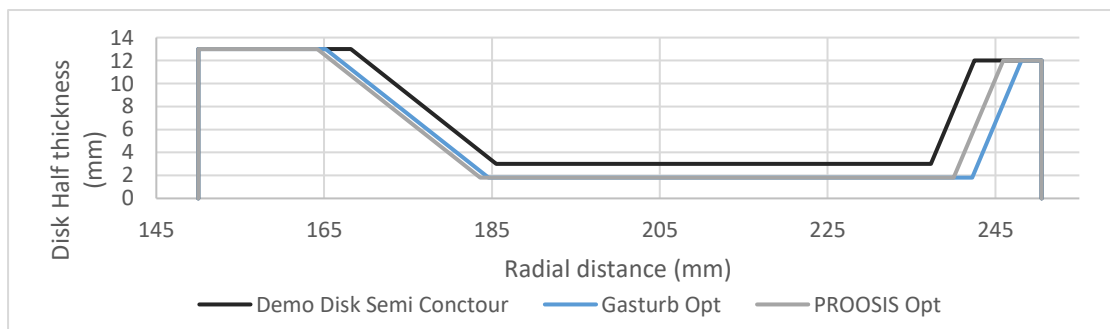


Figure 69: Contours of initial disk (black line), Gasturb Details 5 optimum disk (blue line) and PROOSIS optimum disk (grey line).

All the design variables are decreased in the final solution in comparison with their initial values. This results in smaller disk dimensions and thus in less weight. All the final values are of the same order of magnitude. The differences between the two solutions could be attributed to the different optimization method used, the way the constraints are imposed or the possible different calculation of the objective function since Gasturb Details 5 does not give such information.

## 7. Summary, conclusions and future suggestions

For the purpose of this thesis, bibliographical sources concerning the design and optimization of thermal turbomachinery disks were extensively studied. Using this information, tools for the design and optimization of disks were developed in PROOSIS. Two main functions were developed; the temperature profile calculating function and the stress calculating function which takes the results from the temperature analysis as an input. The results of these functions were validated by comparison with Solidworks results. Subsequently, they were used for the optimization problem. Weight optimization was accomplished by the stresses maximization. The initial geometries were taken from the first three disks of HPC NASA/GE E3. Nelder-Mead Simplex method was used for the update of the geometry and in every iteration the temperature and stress calculating functions were called to recalculate the objective function value. There were three optimization cases examined, each with variables and constraints according to Lolis, Gasturb and Armand.

It can be concluded that the one-dimensional modeling for temperature and stress calculation gives results very close to the FEA method with far less nodes and thus in less processing time. This makes the optimization quicker. Additionally, it is proven that the maximization of the stresses using Simplex method can result in a lighter design with as much as 7 design variables. Apart from that the proximity of the PROOSIS optimum solution with the one calculated by “Gasturb Details 5” validates the efficiency of the optimization program.

The developed tools are quite versatile since a lot of options are left to the user and can be put as inputs in the functions. This makes them suitable for integration in bigger problems like a whole engine design. After the airflow analysis, the resulting blade geometry can be used for the extraction of an optimized disk geometry to support the blade. The same tools can be run successively until the disks of a whole engine are designed. Alternatively, the optimization method developed can be combined with other methods such as genetic algorithms.

## References

- [1] “Structural Optimization Methodology for Rotating Disks of Aircraft Engines” ,Sasan C. Armand , NASA Lewis Research Center Ohio ,1995
- [2] “Rapid low fidelity turbomachinery disk optimization” David P. Gutzwiller, Mark G. Turner 2010
- [3] “A Computer Code for Gas Turbine Engine Weight and Disk Life Estimation” , Michael T. Tong ,Ian Halliwell , Louis J. Ghosn ,2004
- [4] “Energy Efficient Engine High Pressure Compressor Detailed Design Report” P.R Holloway, G.L. Knight , C.C. Koch , S.J Shaffer , NASA-Lewis Research Center 1982
- [5] “GasTurb Details” Joachim Kurzke
- [6] “Heat Transfer”, 10<sup>th</sup> Edition , J.P.Holman
- [7] “Heat and Mass Transfer, Fundamentals & Applications”, 5<sup>th</sup> Edition, Yunus A. Cengel, Afshin J.Ghahar
- [8] “Mechanical Design of Turbomachinery Notes”, Dr Suresh Sampath, R A Cookson, A S Haslam, P Laskaridis , p.152
- [9] “Development of a Preliminary Weight Estimation Method for Advanced Turbofan Engines” , Periklis Lolis, P.h.D Thesis, July 2014
- [10] “Numerical Recipes, The art of scientific computing”, William H. Press, Saul A. Teukolsky, William T. Vetterling, Brian P. Flannery, 2007

## 8. Εκτεταμένη περίληψη (Ελληνικά)

Σε αυτή τη διπλωματική εργασία μελετάται ο σχεδιασμός δίσκων θερμικών στροβιλομηχανών. Η διαδικασία ξεκινά από μια αρχική γεωμετρία δίσκου και προτείνει με νέα που ικανοποιεί όλες τις απαιτήσεις του προκαταρκτικού σχεδιασμού ενός δίσκου, με λιγότερο βάρος. Πιο συγκεκριμένα, δημιουργήθηκαν στο λογισμικό PROOSIS τα αριθμητικά εργαλεία για την βελτιστοποίηση ενός δίσκου.

Για τον σκοπό αυτής της εργασίας χρησιμοποιήθηκε σαν πρότυπο ο κινητήρας NASA's/GE E3. Οι γεωμετρίες των δίσκων των τριών πρώτων βαθμίδων του συμπιεστή υψηλής πίεσης του αντλήθηκαν από την ψηφιοποίηση των σχεδίων του κινητήρα που βρέθηκαν στη βιβλιογραφία. Επιπλέον και άλλες σημαντικές τιμές για τα περύγια αντλήθηκαν από πίνακες που υπάρχουν στις πηγές. Με τις πληροφορίες για τα περύγια ήταν δυνατός ο υπολογισμός του βάρους τους, των κέντρων μάζας τους και τελικά των φορτίων που επιβάλλουν στον δίσκο ως οριακές συνθήκες.

Η βελτιστοποίηση απαιτεί τον υπολογισμό τάσεων ώστε να εξασφαλιστεί ότι ικανοποιούνται τα τασικά κριτήρια. Πριν τον υπολογισμό των τάσεων η θερμοκρασιακή κατανομή του δίσκου είναι απαραίτητη για να χρησιμοποιηθεί ως είσοδος στον υπολογισμό των τάσεων και έτσι να συνυπολογιστούν οι θερμικές τάσεις. Συμπερασματικά, τα βασικά εργαλεία που αναπτύχθηκαν πριν την βελτιστοποίηση είναι μια συνάρτηση υπολογισμού του θερμοκρασιακού προφίλ και μια συνάρτηση υπολογισμού των τάσεων. Οι παραπάνω συναρτήσεις βασίζονται τη λύση τους σε μονοδιάστατες μεθόδους. Η συνάρτηση υπολογισμού τάσεων μπορεί να έχει σαν είσοδο το θερμοκρασιακό προφίλ, να λαμβάνει τις ιδιότητες του υλικού σε κάθε κόμβο ανάλογα με την θερμοκρασία του και μπορεί να διαχειριστεί ανισότροπα υλικά. Για την πιστοποίηση των αποτελεσμάτων, οι ίδιες αναλύσεις έτρεξαν με τις συναρτήσεις που αναπτύχθηκαν στο PROOSIS και με τη τρισδιάστατη μέθοδο των πεπερασμένων στοιχείων μέσω του SOLIDWORKS. Η στατική θερμοκρασιακή ανάλυση του Solidworks υπολογίζει την θερμοκρασιακή κατανομή στον δίσκο. Η στατική τασική ανάλυση του ίδιου λογισμικού υπολογίζει την κατανομή των τάσεων ανάλογα με τα φορτία που επιβάλλονται. Είναι δυνατόν τα αποτελέσματα μιας θερμικής ανάλυσης να εισαχθούν στην τασική ανάλυση για τον συνυπολογισμό των θερμικών τάσεων στις συνολικές τάσεις. Η σύγκριση των αποτελεσμάτων της θερμοκρασιακής κατανομής μπορεί να γίνει μεμονωμένα χρησιμοποιώντας μια τυχαία γεωμετρία δίσκου στροβίλου. Ακολούθως η πιστοποίηση των τάσεων γίνεται μέσω τριών περιπτώσεων φόρτισης. Για τις περιπτώσεις α και β χρησιμοποιείται η γεωμετρία των τριών πρώτων δίσκων του συμπιεστή υψηλής πίεσης του κινητήρα NASA's E3 σε θερμοκρασία δωματίου. Στην περίπτωση γ ο δίσκος προσομοιώνεται με κατανομή θερμοκρασίας. Η περίπτωση γ προσομοιώνεται με την ίδια γεωμετρία δίσκου στροβίλου που χρησιμοποιήθηκε για την πιστοποίηση της θερμοκρασίας.

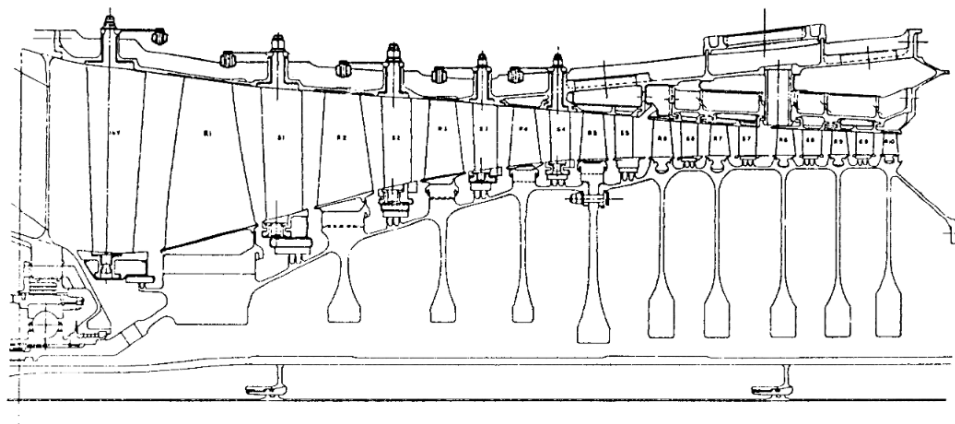
Τα αποτελέσματα που προκύπτουν από τις δύο μεθόδους έχουν σε κάθε περίπτωση επαρκώς μικρές διαφορές. Επομένως, η συγκριτικά χρονοβόρα μέθοδος των πεπερασμένων στοιχείων μπορεί να αντικατασταθεί από τις μεθόδους που υλοποιήθηκαν στο PROOSIS. Συμπεραίνεται ότι οι συναρτήσεις που αναπτύχθηκαν στο PROOSIS είναι κατάλληλες για ένα πρόβλημα βελτιστοποίησης όπου οι τάσεις χρειάζεται να υπολογιστούν πολλές φορές.

Ο σκοπός της βελτιστοποίησης είναι η μείωση του βάρους τηρώντας τους περιορισμούς. Για αυτό το λόγο, αναπτύχθηκε στο λογισμικό του εργαστηρίου μια συνάρτηση υπολογισμού

βάρους με είσοδο την γεωμετρία δίσκου. Η συνάρτηση χρησιμοποιεί τον αναλυτικό τύπο για τον όγκο και το βάρος δίσκου και τα αποτελέσματα της πιστοποιούνται με τη χρήση του εργαλείου υπολογισμού μάζας στο Solidworks. Οι μεταβλητές σχεδιασμού είναι πάντα κάποιες από τις διαστάσεις του δίσκου. Οι περιορισμοί αποτελούνται από τα επιτρεπόμενα όρια των τάσεων και τους γεωμετρικούς περιορισμούς που φράζουν ορισμένες διαστάσεις και τις συνδέουν με σχέσεις μεταξύ τους. Η μέθοδος πολυτόπου Nelder-Mead (Simplex) χρησιμοποιήθηκε για την ελαχιστοποίηση του βάρους. Σε κάθε επαναλάληψη η κατανομή θερμοκρασιών και τάσεων επαναυπολογίζεται για την ανανεωμένη γεωμετρία και ελέγχεται η ικανοποίηση των περιορισμών, επιπλέον επαναυπολογίζεται και η τιμή της αντικειμενικής συνάρτησης. Εφόσον η Simplex είναι μέθοδος που απαιτεί μόνο την τιμή της αντικειμενικής συνάρτησης, μια τιμή προστίθεται σε αυτήν με κάθε παραβίαση ενός περιορισμού. Η μείωση του βάρους είναι ισοδύναμη με την αύξηση των τάσεων, επομένως η αντικειμενική συνάρτηση καταστρώνεται με τρόπο που η ελαχιστοποίηση της συνεπάγεται μεγιστοποίηση των τάσεων. Η αντικειμενική συνάρτηση δεν είναι απαραίτητα συνεχής αλλά ένα πλεονέκτημα της Simplex είναι ότι διαχειρίζεται και μη συνεχείς συναρτήσεις. Η βελτιστοποίηση υλοποιείται σε τρεις διαφορετικές περιπτώσεις, καθεμία από τις οποίες έχει δικές τις μεταβλητές και περιορισμούς σύμφωνα με τις βιβλιογραφικές πηγές : Lolis, Gasturb, Armand. Κάθε μία από αυτές τις μεθόδους χρησιμοποιείται για την βελτιστοποίηση των τριών πρώτων δίσκων του συμπιεστή υψηλής πίεσης της μηχανής NASA's E3. Επιπλέον έγινε σύγκριση των αποτελεσμάτων βελτιστοποίησης με το λογισμικό «Gasturb Details 5». Χρησιμοποιήθηκε το αρχείο «DemoDisk» που βρίσκεται ήδη στο λογισμικό. Η γεωμετρία, οι οριακές συνθήκες, η θερμοκρασιακή κατανομή, οι μεταβλητές και οι περιορισμοί τηρήθηκαν ίδια στο GASTURB και στο PROOSIS. Τα αποτελέσματα ήταν κοντινά.

## 8.1 Εισαγωγή

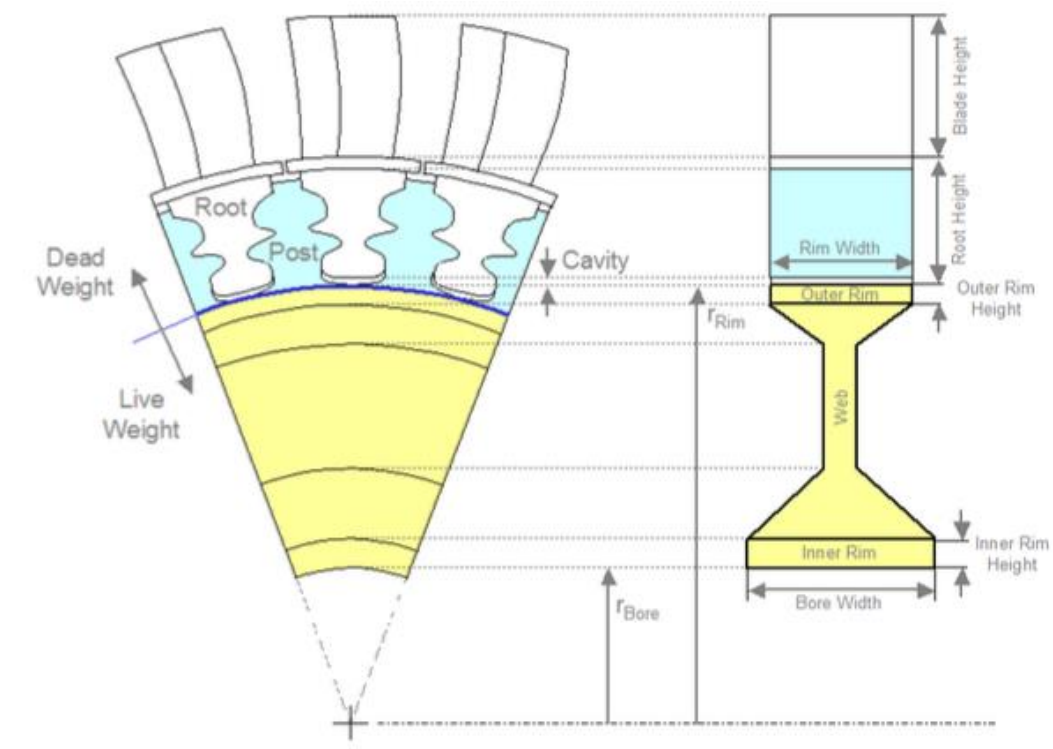
Οι δίσκοι μιας θερμικής στροβιλομηχανής είναι βασικές συνιστώσες γιατί στηρίζουν τα περιστρεφόμενα πετρώγια και τα συνδέουν με τον άξονα. Μετά το σχεδιασμό των περυγίων, θα πρέπει να σχεδιαστούν οι δίσκοι έτσι ώστε να τηρούνται όλες οι μηχανικές απαιτήσεις ειδικά στις υψηλές θερμοκρασίες που επικρατούν στο στρόβιλο. Η Εικόνα 1 αναπαριστά σε σκαρίφημα την ημιτομή του συμπιεστή υψηλής πίεσης της μηχανής NASA/GE E3.



Εικόνα 1: Σκαρίφημα της ημιτομής του συμπιεστή υψηλής πίεσης της μηχανής NASA/GE E3



Το συναρμολόγημα δίσκου και πτερυγίων μπορεί να διαχωριστεί σε δύο νοητά μέρη: το dead weight και το live weight. Το live weight είναι το μέρος του δίσκου που θεωρείται ότι προσφέρει την μηχανική στήριξη και είναι αυτό που μελετάται σε αυτή την εργασία. Δέχεται τα φυγοκεντρικά φορτία της δικής του μάζας και της μάζας του dead weight. Το dead weight δεν προσφέρει στήριξη, μόνο επιβάλλει το φυγοκεντρικό του φορτίο στον υπόλοιπο δίσκο. Αποτελείται από τα πτερύγια και τα posts του δίσκου. Τα posts είναι ειδικές διαμορφώσεις πάνω στον δίσκο για την προσάρτηση των πτερυγίων. Το live weight μπορεί να λάβει διάφορα σχήματα, τρία είναι τα βασικά που χρησιμοποιούνται περισσότερο στη βιβλιογραφία: το ring type, το web type και το hyperbolic type. Στον συμπιεστή υψηλής πίεσης της μηχανής Ε3 ο δίσκος της πρώτης βαθμίδας είναι ring type, της δεύτερης hyperbolic type και της τρίτης web type. Στην Εικόνα 2 φαίνεται το συναρμολόγημα του δίσκου με τα πτερύγια και η διαχωριστική γραμμή μεταξύ live και dead weight. Το κίτρινο μέρος είναι το live weight, το γαλάζιο μέρος είναι τα posts και το λευκό μέρος είναι τα πτερύγια. Η συναρμογή των πτερυγίων με το δίσκο είναι χαλαρή, υπάρχει και μια κοιλότητα ανάμεσα στο κατώτερο σημείο του πτερυγίου και στο λεγόμενο rim, το σημείο του live weight με τη μεγαλύτερη ακτίνα. Η προσάρτηση γίνεται με δύο συμπληρωματικά σχήματα που περιορίζουν την μετακίνηση του πτερυγίου ακτινικά, το ένα είναι στη ρίζα του πτερυγίου και το άλλο στο post του δίσκου.



Εικόνα 2: Σε αυτή την εικόνα φαίνεται το συναρμολόγημα δίσκου και πτερυγίων. Το κίτρινο μέρος είναι το live weight, το γαλάζιο μέρος είναι τα posts και το λευκό μέρος είναι τα πτερύγια. Τα πτερύγια προσαρτώνται στους δίσκους μέσω της εμπλοκής με τα posts.

Το σχήμα ενός δίσκου μπορεί να περιγραφεί με έξι ακτινικές αποστάσεις από το κέντρο περιστροφής

$$r_1, r_2, r_3, r_4, r_5, r_6$$

Και έξι πάχη στις αντίστοιχες ακτίνες

$$t_1, t_2, t_3, t_4, t_5, t_6$$

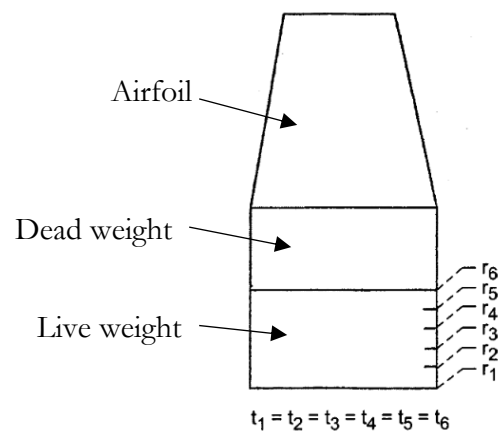
Τύπος ring: Αυτός ο τύπος δίσκου περιγράφεται από το πάχος του που θεωρείται σταθερό σε κάθε θέση και δύο ακτινικές θέσεις, την εξωτερική και την εσωτερική. Για τις ενδιάμεσες ακτινικές θέσεις εφαρμόζεται γραμμική παρεμβολή:

$$t_1 = t_2 = t_3 = t_4 = t_5 = t_6 = t_{rim}$$

$$r_1 = r_{bore} , r_6 = r_{rim}$$

$$r_i = r_1 + (i - 1) \cdot \frac{r_6 - r_1}{5} \text{ for } i = 1, \dots, 6$$

Η Εικόνα 3 παρουσιάζει την τομή ενός δίσκου ring γεωμετρίας.

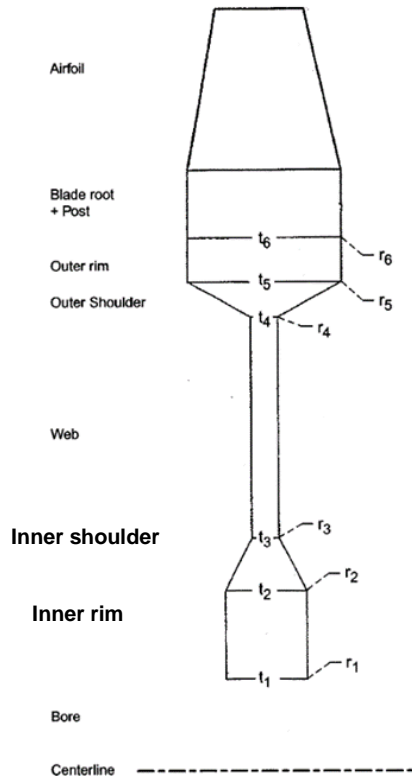


Εικόνα 3: Τομή ενός δίσκου με γεωμετρία τύπου ring. Πάνω από το live weight, βρίσκεται το dead weight από το οποίο φαίνεται το post και η αεροτομή.

Τύπος web: Αυτός ο τύπος δίσκου παρουσιάζεται στην Εικόνα 4. Βασικό του χαρακτηριστικό είναι ότι έχει τρία μέρη με σταθερό πάχος, το inner rim, το web και το outer rim.

$$t_1 = t_2, t_3 = t_4, t_5 = t_6$$

$$t_3 < t_2, t_4 < t_5$$



Εικόνα 4: Τομή δίσκου γεωμετρίας web

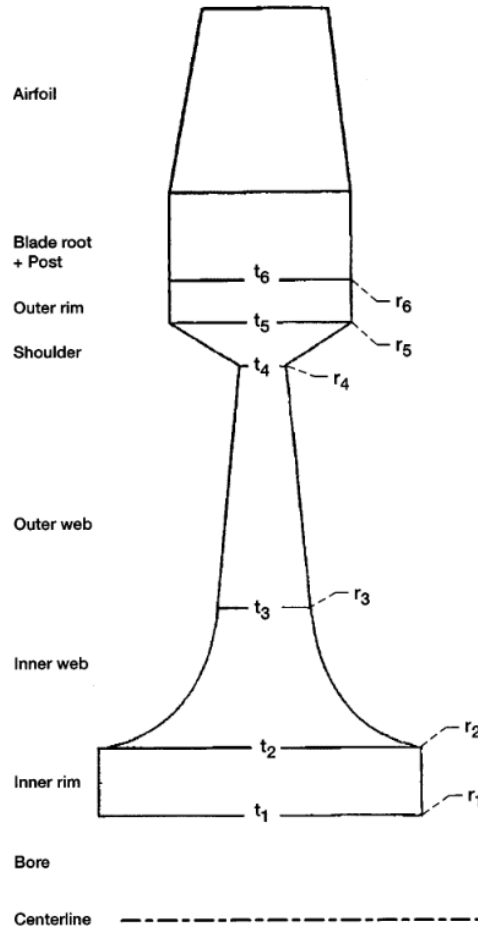
Τύπος hyperbolic: Αυτός ο τύπος δίσκου φαίνεται στην Εικόνα 5. Έχει δύο μέρη με σταθερό πάχος, το inner rim και το outer rim. Βασικές διαφορές του από την γεωμετρία web είναι ότι τα πάχη στις θέσεις 3 και 4 δεν είναι ίσα μεταξύ τους και μεταξύ των ακτινικών θέσεων 2 και 3 υπάρχει καμπύλη. Το πάχος σε κάθε σημείο μεταξύ των 2 και 3 δίνεται από την εξίσωση [2]:

$$t_i = t_2 + (t_3 - t_2) \left( \frac{r_i - r_2}{r_3 - r_2} \right)^{dsf}$$

Ο συντελεστής σχήματος  $dsf < 1$  επιλέγεται από τον χρήστη. Ισχύουν οι παρακάτω συσχετίσεις διαστάσεων:

$$t_1 = t_2, t_5 = t_6$$

$$t_3 < t_2, t_4 < t_5$$



Εικόνα 5: Τομή δίσκου γεωμετρίας hyperbolic type

## 8.2 Υπολογισμοί για το dead weight

Εξισώσεις για την γεωμετρία, το βάρος και το κέντρο μάζας του περυγίου μπορούν να αντληθούν από την βιβλιογραφία [5]. Ξεκινώντας από την γεωμετρία της αεροτομής και χρησιμοποιώντας αυτές τις εξισώσεις μπορεί να υπολογιστεί το dead weight ανα περύγιο και το κέντρο μάζας του. Τότε το φυγοκεντρικό φορτίο που προκαλείται στο rim υπολογίζεται ως:

$$\sigma_{r,rim} = \frac{n_b m_b r_{cg}}{2\pi r_{rim} t_{rim}} \omega^2$$

### 8.3 Υπολογισμός θερμοκρασιακού προφίλ

Υλοποιήθηκαν δυο προσεγγίσεις για τον υπολογισμό της ακτινικής κατανομής της θερμοκρασίας, μια που δεν λαμβάνει υπόψη της το μεταβλητό πάχος του δίσκου και μια που το λαμβάνει. Για να πιστοποιηθούν τα αποτελέσματα και των δύο, έγινε θερμική ανάλυση ενός δίσκου με τις δύο προαναφερθείσες μεθόδους και με το λογισμικό Solidworks που χρησιμοποιεί την τρισδιάστατη μέθοδο των πεπερασμένων στοιχείων. Έστερα συγκρίθηκαν τα αποτελέσματα.

Στην πρώτη περίπτωση χρησιμοποιείται η μονοδιάστατη εξίσωση αγωγής θερμότητας του Fourier σε κυλινδρικές συντεταγμένες:

$$\frac{d^2T}{dr^2} + \frac{1}{r} \frac{dT}{dr} = 0$$

Η παραπάνω εξίσωση λύνεται αναλυτικά με οριακές συνθήκες τις θερμοκρασίες στο bore και στο rim και προκύπτει:

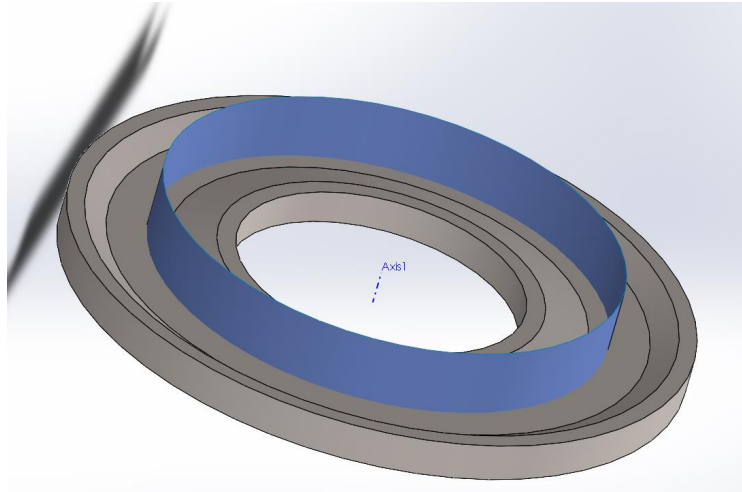
$$T(r) = \frac{T_{bore} - T_{rim}}{\ln r_{bore} - \ln r_{rim}} \ln \frac{r}{r_{rim}} + T_{rim}$$

Στην δεύτερη περίπτωση, το πρόβλημα λαμβάνει υπόψη το μεταβλητό πάχος δίσκου εισάγωντας στην εξίσωση Fourier την συνεισφορά του πάχους σε κάθε ακτινική θέση μέσω του εμβαδού  $A_h$ . Το εμβαδόν  $A_h$  είναι το κυλινδρικό εμβαδόν μέσα από το οποίο άγεται η θερμότητα σε κάθε ακτινική θέση. Η εξίσωση Fourier σε αυτή την περίπτωση γράφεται ως:

$$\frac{1}{A_h} \frac{\partial}{\partial r} \left( k A_h \frac{\partial T}{\partial r} \right) + \dot{q} = \rho c_p \frac{\partial T}{\partial t}$$

Η επιφάνεια  $A_h$  περιγράφεται στην Εικόνα 6 και για μία ακτινική θέση  $i$  δίνεται από την παρακάτω εξίσωση:

$$A_{h,i} = 2\pi r_i t_i$$



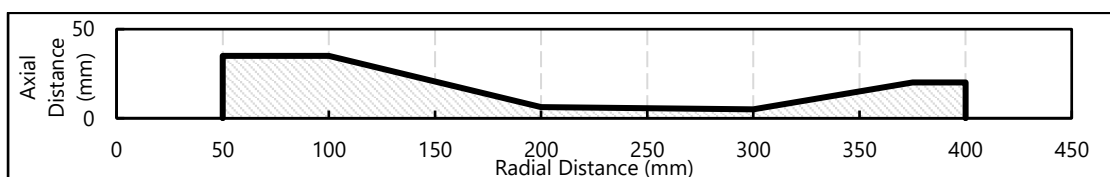
Εικόνα 6: Το γκρίζο τεμάχιο είναι ο δίσκος. Το εμβαδον  $A_h$  σε κάθε ακτινική θέση είναι η τομή της μπλέ κυλινδρικής επιφάνειας με το δίσκο. Η μπλέ επιφάνεια έχει κάθε φορά ακτίνα ίση με την ακτινική θέση του δίσκου που μας αφορά.

Η τελευταία εξίσωση του Fourier διακριτοποιείται και έτσι κατασκευάζεται τριδιαγώνιο σύστημα με αγνώστους τις θερμοκρασίες από το οποίο προκύπτει η λύση.

Η υλοποίηση του υπολογισμού της θερμοκρασίας έγινε στο PROOSIS με τη συνάρτηση calcDiskT(). Ο Πίνακας 1 περιέχει τη γεωμετρία, το υλικό και τις οριακές θερμοκρασίες ενός δίσκου στροβίλου

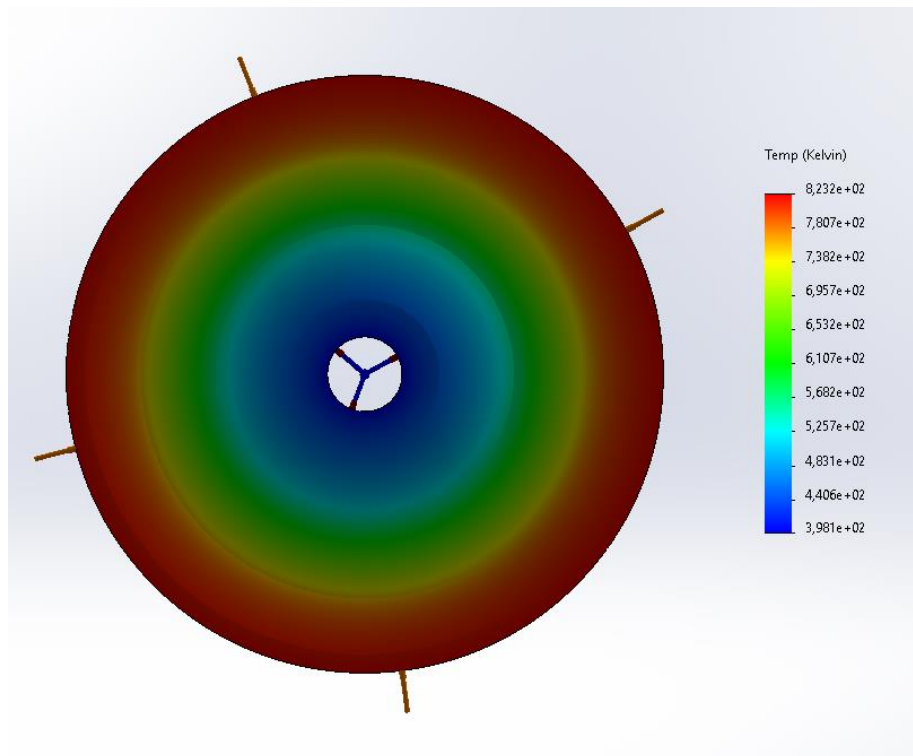
Station	1	2	3	4	5	6
R (m)	0.05	0.1	0.2	0.3	0.375	0.4
t (m)	0.07	0.0225	0.0125	0.01	0.04	0.04
Material	INCONEL 718					
T <sub>bore</sub> (K)	398.15					
T <sub>trim</sub> (K)	823.15					

Πίνακας 1: Η γεωμετρία, το υλικό και οι οριακές θερμοκρασίες ενός τυχαίου δίσκου στροβίλου



Εικόνα 7: Ημιτομή του δίσκου στροβίλου

Τα αποτελέσματα της θερμικής μελέτης στο Solidworks φαίνονται στην Εικόνα 8



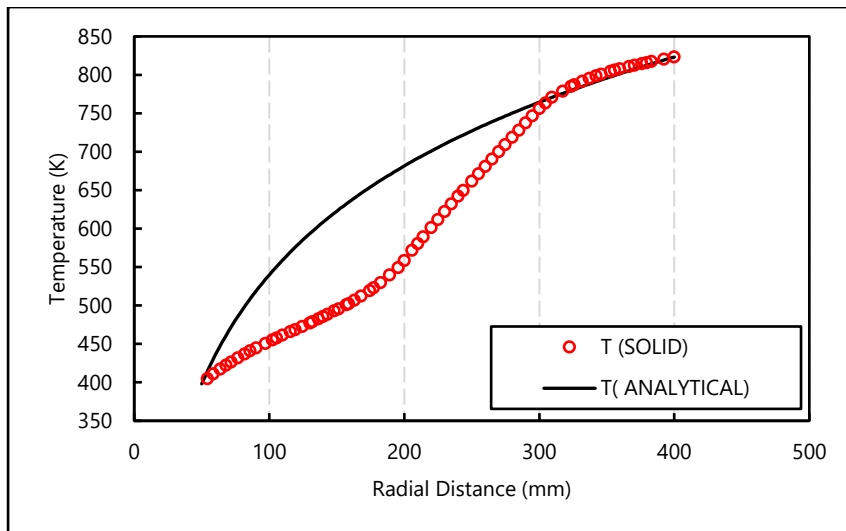
Εικόνα 8: Εικόνα απο τα αποτελέσματα της λύσης του λογισμικού Solidworks

Στο μοντέλο του δίσκου στο Solidworks τοποθετήθηκαν αισθητήρες θερμοκρασίας στο μέσο επίπεδο όπως φαίνεται στην Εικόνα 9 για την απόκτηση του ακτινικού θερμοκρασιακού προφίλ

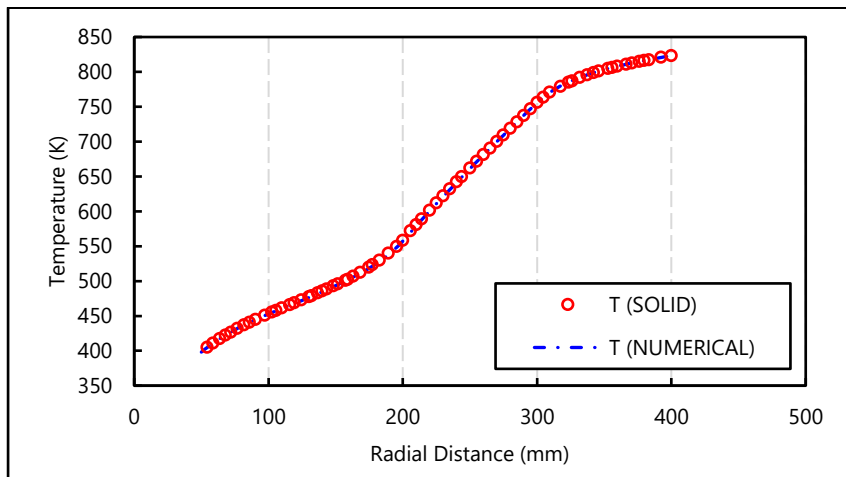


Εικόνα 9: Τα μπλέ σημεία είναι αισθητήρες θερμοκρασίας τοποθετημένοι στο μέσο επίπεδο του δίσκου για την απόκτηση του θερμοκρασιακού προφίλ.

Παρακάτω φαίνεται η σύγκριση των λύσεων που προκύπτουν από τις δυο περιπτώσεις με τη λύση του Solidworks.



Εικόνα 10: Διάγραμμα σύγκρισης της αναλυτικής μονοδιάστατης λύσης και της λύσης του Solidworks



Εικόνα 11: Διάγραμμα σύγκρισης της αριθμητικής λύσης και της λύσης του Solidworks.

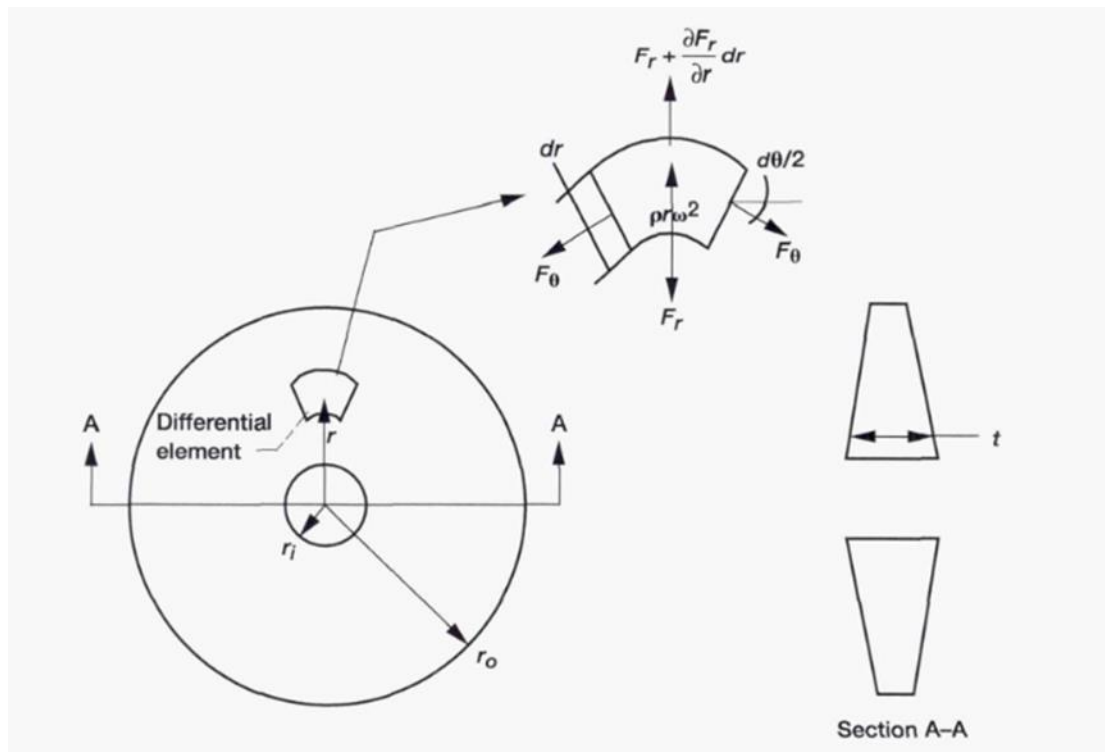
Είναι φανερό ότι η αριθμητική λύση είναι πιο κοντά στην πραγματικότητα και για αυτό χρησιμοποιείται για τον υπολογισμό των τάσεων και κατ'επέκταση για τη βελτιστοποίηση.

## 8.4 Υπολογισμός των τάσεων

Τα σημαντικότερα φορτία για τον σχεδιασμό του δίσκου είναι τα θερμικά, τα φυγοκεντρικά του ίδιου του δίσκου και τα φυγοκεντρικά των πτερυγίων που καλείται να στηρίξει ο δίσκος. [1]. Η μεθοδολογία που αναπτύσσεται θεωρεί επίπεδη εντατική κατάσταση, αμελούνται οι μεταβολές της τάσης και της θερμοκρασίας στην αξονική διεύθυνση, δηλαδή κατά το πάχος του δίσκου. Χρησιμοποιείται η απλοποίηση των μικρών γωνιών λόγω μικρών μετατοπίσεων. Οι δίσκοι συνδέονται με τον άξονα μέσω δακτυλίων ή κώνων οι οποίοι είναι πολύ πιο εύκαμπτοι από τους δίσκους και για αυτό θεωρείται ότι δεν επιβάλλουν κανένα ακτινικό ή περιφερειακό φορτίο. Για αυτό η οριακή συνθήκη ακτινικής τάσης στο bore είναι μηδενική. Το μέσο επίπεδο του δίσκου χωρίζεται σε στοιχεία που ορίζονται από την στοιχειώδη ακτίνα  $dr$ , τη στοιχειώδη γωνία  $d\theta$  και την ακτινική απόσταση του κέντρου τους από το κέντρο



περιστροφής του δίσκου, όπως φαίνεται στην Εικόνα 12. Η ανάλυση που ακολουθείται για τον υπολογισμό των τάσεων αντλείται από τη βιβλιογραφία [2].



Εικόνα 12: Διαχωρισμός του μέσου επιπέδου του δίσκου σε στοιχεία.

Από την ισορροπία των στοιχείων προκύπτει η βασική διαφορική εξίσωση για τις τάσεις του δίσκου:

$$\frac{d}{dr}(tr\sigma_r) - t\sigma_\theta + tpr^2\omega^2 = 0$$

Οι τάσεις προκύπτουν από το συνυπολογισμό θερμικών και μηχανικών τάσεων :

$$\begin{bmatrix} \sigma_r \\ \sigma_\theta \\ \sigma_z \\ \tau_{rz} \\ \tau_{\theta z} \\ \tau_{r\theta} \end{bmatrix} = \begin{bmatrix} \sigma_r^m \\ \sigma_\theta^m \\ \sigma_z^m \\ \tau_{rz}^m \\ \tau_{\theta z}^m \\ \tau_{r\theta}^m \end{bmatrix} + \begin{bmatrix} \sigma_r^T \\ \sigma_\theta^T \\ \sigma_z^T \\ \tau_{rz}^T \\ \tau_{\theta z}^T \\ \tau_{r\theta}^T \end{bmatrix}$$

Σύμφωνα με το γενικευμένο νόμο του Hooke ισχύουν:

$$[\mathbf{C}] = \begin{bmatrix} C_{11} & C_{12} & C_{13} & 0 & 0 & 0 \\ C_{12} & C_{22} & C_{23} & 0 & 0 & 0 \\ C_{13} & C_{23} & C_{33} & 0 & 0 & 0 \\ 0 & 0 & 0 & C_{44} & 0 & 0 \\ 0 & 0 & 0 & 0 & C_{55} & 0 \\ 0 & 0 & 0 & 0 & 0 & C_{66} \end{bmatrix}$$

$$[\sigma^m] = [\mathbf{C}][\varepsilon]$$

$$[\sigma^T] = [\mathbf{C}][\beta]T$$

Όπου  $T$  είναι η διαφορά της θερμοκρασίας από τη θερμοκρασία αναφοράς και οι παραμορφώσεις υπολογίζονται ως εξής:

$$\varepsilon = \begin{bmatrix} \varepsilon_r \\ \varepsilon_\theta \\ \varepsilon_z \\ \gamma_{rz} \\ \gamma_{\theta z} \\ \gamma_{r\theta} \end{bmatrix} = \begin{bmatrix} \frac{du}{dr} \\ \frac{u}{r} \\ -\frac{C_{13}}{C_{33}} \frac{du}{dr} - \frac{C_{23}}{C_{33}} \frac{u}{r} \\ 0 \\ 0 \\ 0 \end{bmatrix}$$

$$\beta = \begin{bmatrix} \beta_r \\ \beta_\theta \\ \beta_z \\ \beta_{rz} \\ \beta_{\theta z} \\ \beta_{r\theta} \end{bmatrix} = \begin{bmatrix} \alpha_r \\ \alpha_\theta \\ -\frac{C_{13}}{C_{33}} \alpha_r - \frac{C_{23}}{C_{33}} \alpha_\theta \\ 0 \\ 0 \\ 0 \end{bmatrix}$$

Με επίλυση ως προς την ακτινική και περιφερειακή τάση προκύπτει:

$$\sigma_r = A \frac{du}{dr} + B \frac{u}{r} - A\alpha_r T - B\alpha_\theta T$$

$$\sigma_\theta = B \frac{du}{dr} + D \frac{u}{r} - B\alpha_r T - D\alpha_\theta T$$

Όπου οι συντελεστές είναι:

$$A = \frac{C_{11}C_{33} - C_{13}^2}{C_{33}}, B = \frac{C_{12}C_{33} - C_{13}C_{23}}{C_{33}}, D = \frac{C_{22}C_{33} - C_{23}^2}{C_{33}}$$

Και τα στοιχεία του πίνακα ελαστικότητας είναι:

$$C_{11} = C_{33} = \frac{E_r(E_\theta - E_r\nu_{\theta r}^2)}{E_\theta - 2E_r\nu_{\theta r}^2}$$

$$C_{22} = \frac{E_{\theta}^2}{E_{\theta} - 2E_r\nu_{\theta r}^2}$$

$$C_{12} = C_{23} = \frac{E_r E_{\theta} \nu_{\theta r}}{E_{\theta} - 2E_r\nu_{\theta r}^2}$$

$$C_{13} = \frac{E_r^2 \nu_{\theta r}^2}{E_{\theta} - 2E_r\nu_{\theta r}^2}$$

Οι εξισώσεις καλύπτουν την περίπτωση του ανισότροπου υλικού

Οι οριακές συνθήκες είναι :

$$\sigma_{r,bore} = A \frac{du}{dr} + B \frac{u}{r} - A\alpha_r T - B\alpha_{\theta} T \Big|_{r_{bore}} = 0$$

$$\sigma_{r,rim} = A \frac{du}{dr} + B \frac{u}{r} - A\alpha_r T - B\alpha_{\theta} T \Big|_{r_{rim}} = \frac{n_b m_b r_{cg}}{2\pi r_{rim} t} \omega^2$$

Οι παραπάνω διαφορικές εξισώσεις και οριακές συνθήκες διακριτοποιούνται και ύστερα συνδυάζονται ώστε να διαμορφωθεί ένας τριδιαγώνιος πίνακας με αγνώστους τις μετατοπίσεις σε κάθε κόμβο. Απο τη λύση του συστήματος υπολογίζεται το διάνυσμα των μετατοπίσεων και κατ'επέκταση οι ακτινικές και περιφερειακές τάσεις. Η von mises τάση δίνεται από τον τύπο

$$\sigma_{von Mises} = \sqrt{\frac{(\sigma_r - \sigma_{\theta})^2 + \sigma_{\theta}^2 + \sigma_r^2}{2}}$$

Ο υπολογισμός των τάσεων γίνεται με την χρήση της συνάρτησης calcDiskS\_FV() που δημιουργήθηκε στο PROOSIS.

## 8.5 Πιστοποίηση των αποτελεσμάτων των τάσεων

Για την πιστοποίηση των αποτελεσμάτων σχεδιάστηκαν στο Solidworks οι δίσκοι των τριών πρώτων βαθμίδων του HPC της μηχανής NASA's E3 η γεωμετρία των οποίων περιγράφεται στον Πίνακα 2 . Κάθε δίσκος προσομοιώθηκε με το Solidworks σε δύο σενάρια φόρτισης, τα Loac case a και b που περιγράφονται στους Πίνακες 3 και 4.

Αριθμός βαθμίδας	1	2	3
Γωνιακή ταχύτητα $\omega$ (rad/s)	1300.3		
Υλικό	Ti-8-1-1	Ti-6Al-4V	Ti-6Al-4V
Πυκνότητα (kg/m <sup>3</sup> )	4370.0	4430.0	4430.0
Τύπος δίσκου	RING	HYPERBOLIC	WEB
R1 (m) ακτίνα στο Bore	0.104071	0.106618	0.106278
R2 (m)	0.114167	0.121019	0.120074
R3 (m)	0.124264	0.140107	0.153574
R4 (m)	0.134361	0.169950	0.198640
R5 (m)	0.144458	0.196733	0.217105
R6 (m) ακτίνα στο Rim	0.154554	0.202010	0.230300
t1 (m)	0.093678	0.032923	0.024693
t2 (m)	0.093678	0.032923	0.024693
t3 (m)	0.093678	0.015273	0.006238
t4 (m)	0.093678	0.007495	0.006238
t5 (m)	0.093678	0.046217	0.028137
t6 (m) Πάχος στο Rim	0.093678	0.046217	0.028137

Πίνακας 2: Πληροφορίες για τους τρεις πρώτους δίσκους του HPC του E3

Περίπτωση φόρτισης	$\alpha$		
Γεωμετρία, Υλικό	Βλ. Πίνακα 2		
Αριθμός βαθμίδας	1	2	3
Θερμοκρασιακή κατανομή	-	-	-
$\sigma_{r,bore}$ (MPa)	0	0	0
$\sigma_{r,rim}$ (MPa)	0	0	0
Υπαρξη φυγοκεντρικών φορτίων λόγω γωνιακής ταχύτητας (rad/s)	1300.3		

Πίνακας 3: Περιγραφή της περίπτωσης φόρτισης  $\alpha$

Περίπτωση φόρτισης	$\beta$		
Γεωμετρία, Υλικό	Βλ. Πίνακα 2		
Αριθμός βαθμίδας	1	2	3
Θερμοκρασιακή κατανομή	-	-	-
$\sigma_{r,bore}$ (MPa)	0	0	0
$\sigma_{r,rim}$ (MPa)	89.7	70.6	61.6
Υπαρξη φυγοκεντρικών φορτίων λόγω γωνιακής ταχύτητας (rad/s)	1300.3		

Πίνακας 4: Περιγραφή της περίπτωσης φόρτισης  $\beta$

Στο τρίτο σενάριο φόρτισης περιλαμβάνεται η θερμοκρασιακή κατανομή και για αυτό η προσομοίωση γίνεται με τον δίσκο στροβίλου με τον οποίο έγινε η πιστοποίηση των θερμοκρασιών.

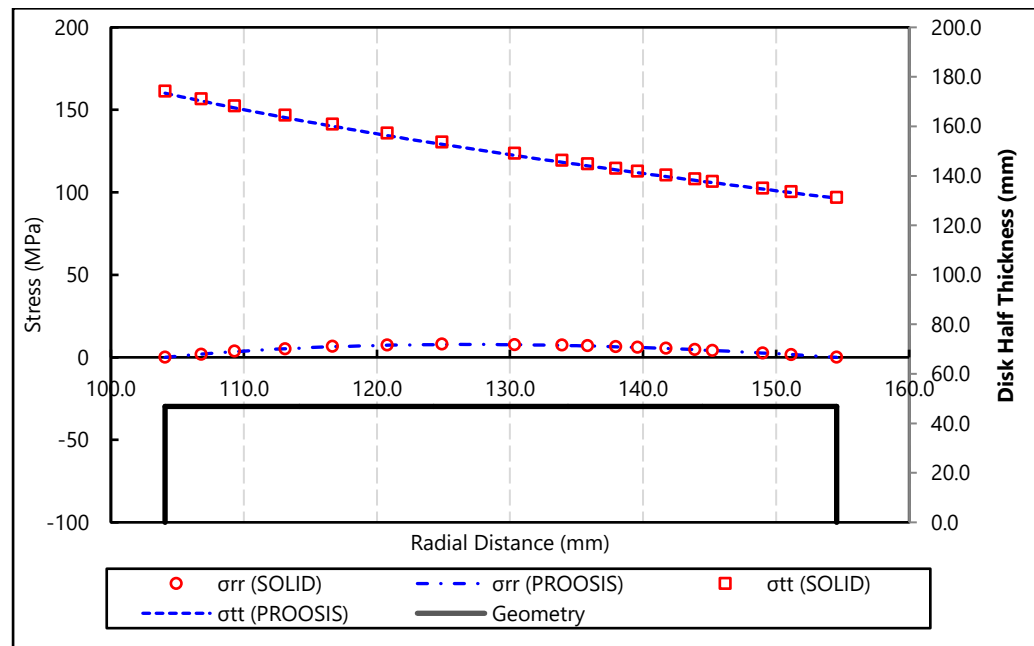
Περίπτωση φόρτισης	$\gamma$	
Γεωμετρία, Υλικό	Βλ. Πίνακα 1	
Θερμοκρασιακή κατανομή	T <sub>bore</sub> (K)	398.15
	T <sub>rim</sub> (K)	823.15
$\sigma_{r,bore}$ (MPa)	0	
$\sigma_{r,rim}$ (MPa)	66.8	
Ύπαρξη φυγοκεντρικών φορτίων λόγω γωνιακής ταχύτητας (rad/s)	392.7	

Πίνακας 5: Περιγραφή της περίπτωσης φόρτισης  $\gamma$

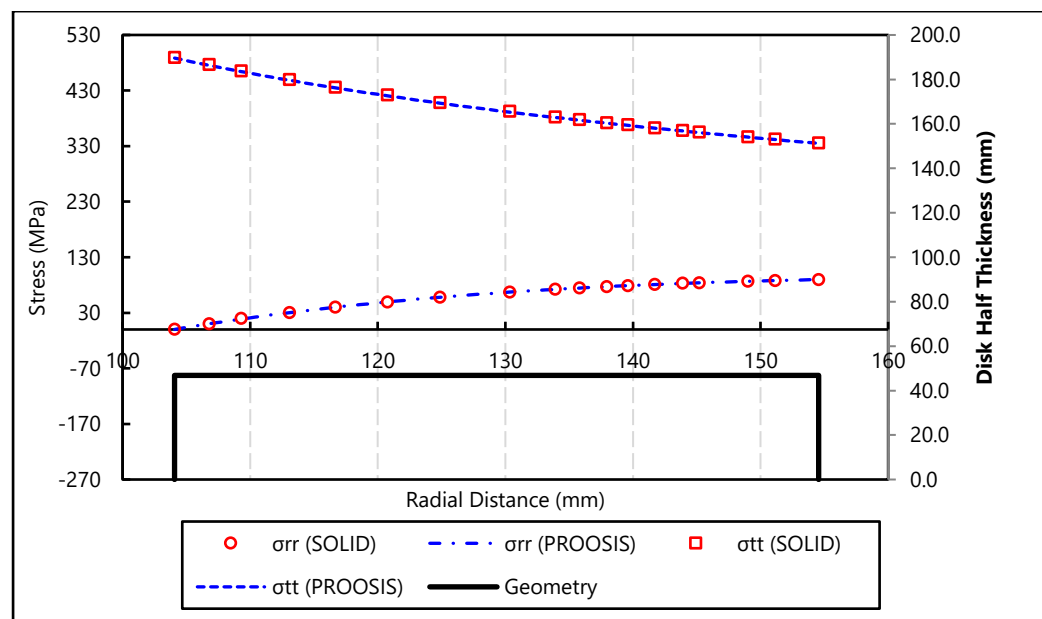
Στα μοντέλα των δίσκων στο Solidworks τοποθετήθηκαν αισθητήρες τάσης ακτινικά στο μέσο επίπεδο του δίσκου για να ληφθεί ένα ακτινικό προφίλ τάσεων. Επιπλέον για να προσομοιωθεί η μηδενική οριακή ακτινική τάση στο bore χρησιμοποιήθηκε το εργαλείο inertial relief που επιβάλλει σε κάθε κόμβο μια αντίθετη αδρανειακή δύναμη με τρόπο που ο δίσκος να ισορροπεί χωρίς να χρειάζονται εδράσεις οι οποίες δεν θα ανταποκρίνονταν στην πραγματικότητα και θα έδιναν λανθασμένα αποτελέσματα. Αυτό συμβαίνει γιατί στην πραγματικότητα κάπου στο σημείο του δίσκου δεν είναι περιορισμένο με μηδενική μετατόπιση καθώς όλα φυγοκεντρίζονται προς τα έξω. Αντίθετα, στο εμπορικό λογισμικό αν κάποια επιφάνεια του δίσκου επιλεγόταν σαν έδραση τότε όλα τα σημεία της θα είχαν μηδενική μετατόπιση τουλάχιστον σε έναν άξονα. Για να θεωρηθεί ο δίσκος πλήρως ισορροπημένος από το λογισμικό και να υλοποιηθεί η ανάλυση θα πρέπει είτε να περιορίζεται με διάφορες εδράσεις η κίνηση του σε όλους τους άξονες είτε να χρησιμοποιηθεί το εργαλείο inertial relief.

Για την περίπτωση φόρτισης  $\gamma$  έτρεξε αρχικά μια θερμική ανάλυση του δίσκου και τα αποτελέσματα αυτής αποτέλεσαν είσοδο για την τασιακή ανάλυση στο Solidworks. Αξίζει να σημειωθεί ότι ο λύτης του Solidworks δεν διαχειριζόταν την ταυτόχρονη αλλαγή των ιδιοτήτων του υλικού σε κάθε κόμβο ανάλογα με την θερμοκρασία. Για αυτό το λόγο, οι ιδιότητες επιλέχθηκαν σε μια σταθερή θερμοκρασία και χρησιμοποιήθηκαν έτσι και στον κώδικα του PROOSIS. Τέλος, έγινε μελέτη ανεξαρτησίας πλέγματος στους δίσκους στο Solidworks. Τα αποτελέσματα παρατίθενται παρακάτω:

Για την Βαθμίδα 1

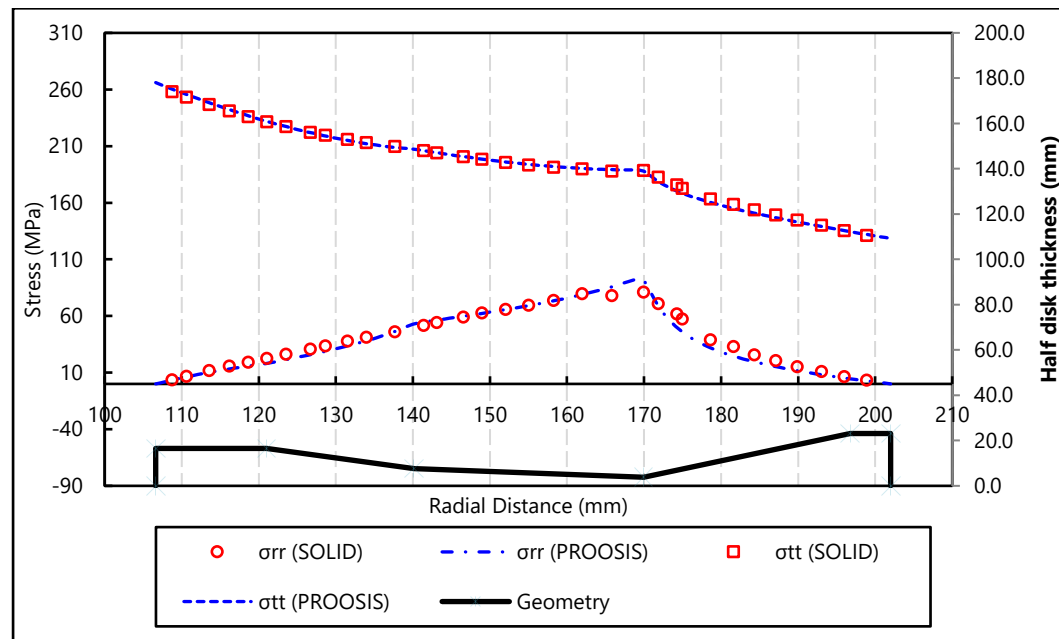


Εικόνα 13: Καμπύλες τάσεων για την 1<sup>η</sup> βαθμίδα του NASA/GE E3 HPC στην περίπτωση φόρτισης α

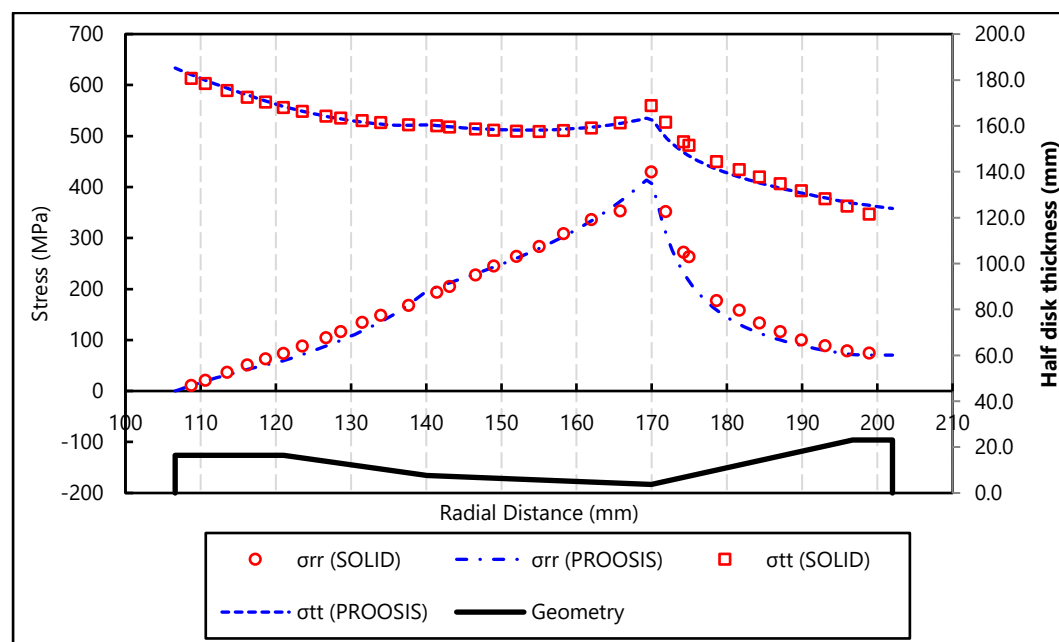


Εικόνα 14: Καμπύλες τάσεων για την 1<sup>η</sup> βαθμίδα του NASA/GE E3 HPC στην περίπτωση φόρτισης β

Για την Βαθμίδα 2:

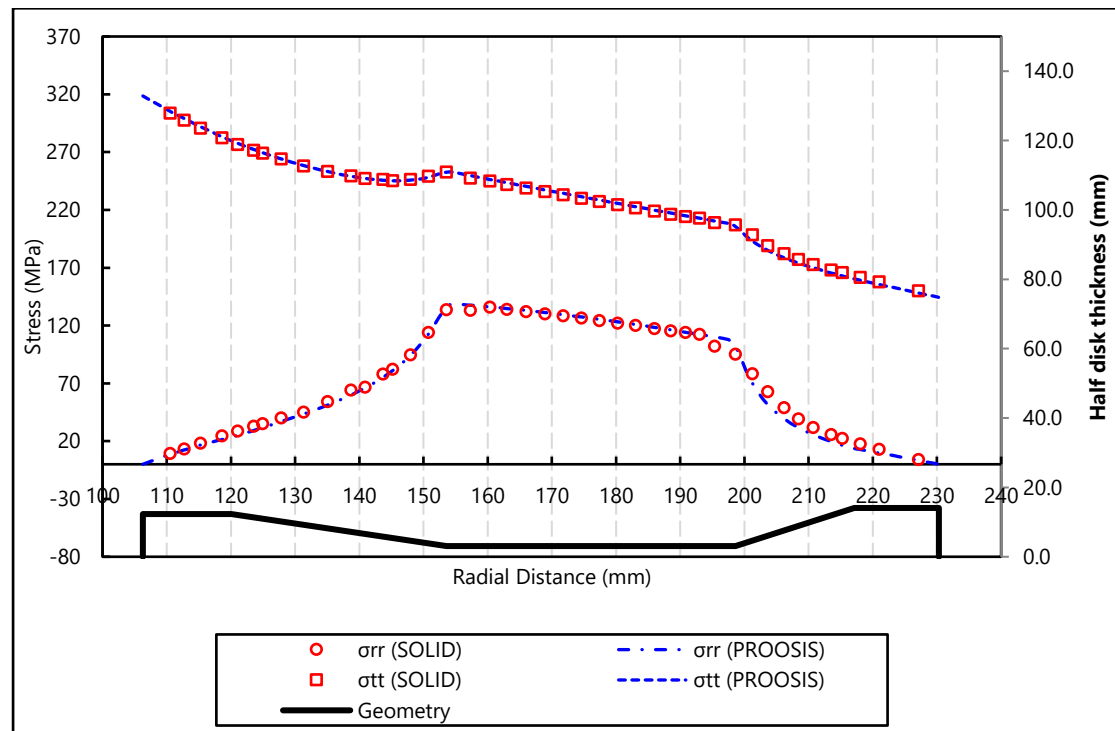


Εικόνα 15: Καμπύλες τάσεων για την 2<sup>η</sup> βαθμίδα του NASA/GE E3 HPC στην περίπτωση φόρτισης α

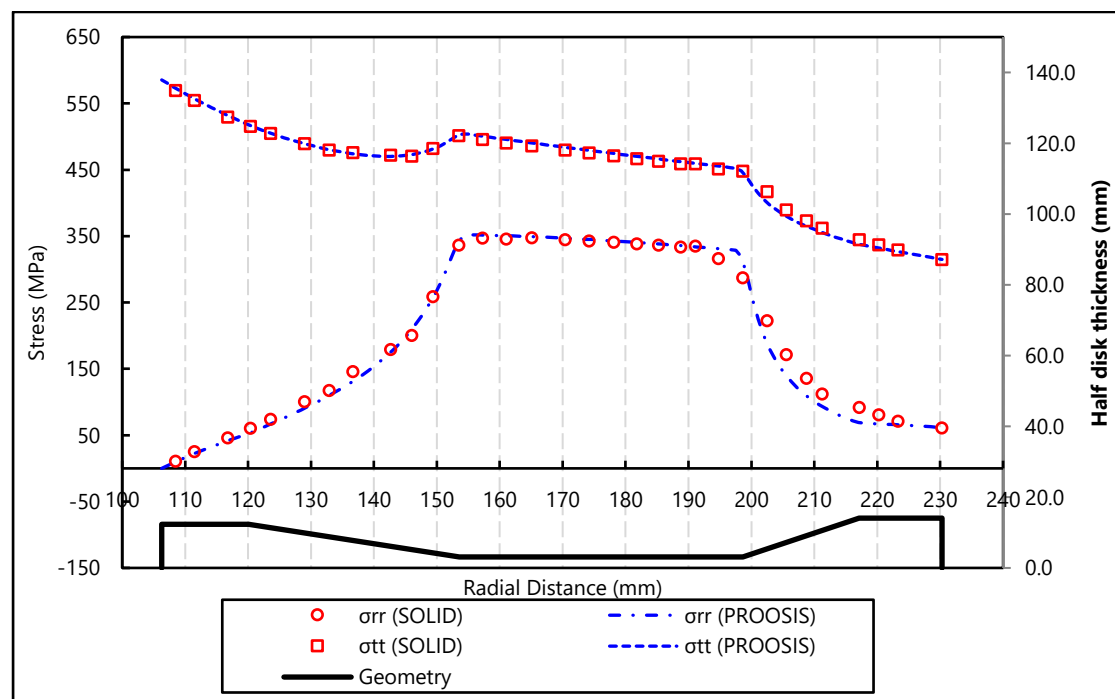


Εικόνα 16: Καμπύλες τάσεων για την 2<sup>η</sup> βαθμίδα του NASA/GE E3 HPC στην περίπτωση φόρτισης β

Για την Βαθμίδα 3:



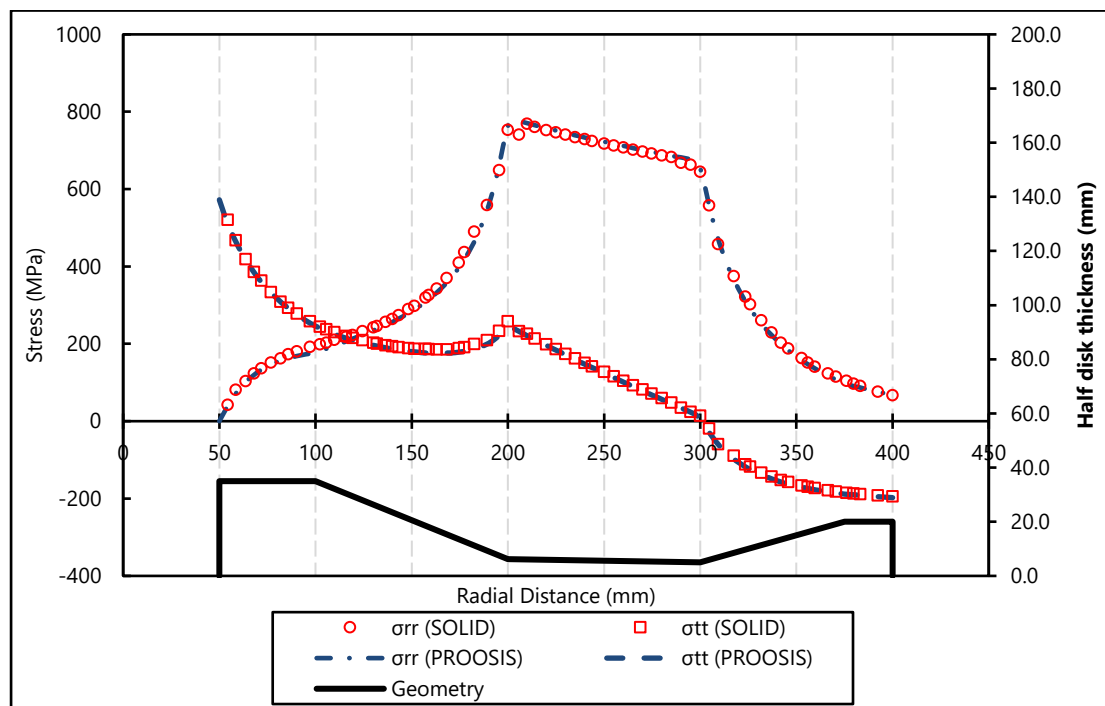
Εικόνα 17: Καμπύλες τάσεων για την 3<sup>η</sup> βαθμίδα του NASA/GE E3 HPC στην περίπτωση φόρτισης α



Εικόνα 18: Καμπύλες τάσεων για την 3<sup>η</sup> βαθμίδα του NASA/GE E3 HPC στην περίπτωση φόρτισης β



Για την τυχαία γεωμετρία δίσκου στροβίλου στην περίπτωση φόρτισης  $\gamma$  :



Εικόνα 19: Καμπύλες τάσεων για τον δίσκο στροβίλου και την περίπτωση φόρτισης  $\gamma$

Συμπεραίνουμε ότι οι δύο μέθοδοι έχουν πολύ κοντινά αποτελέσματα και έτσι το μοντέλο που αναπτύχθηκε στο PROOSIS μπορεί να αντικαταστήσει την μέθοδο των πεπερασμένων στοιχείων που είναι πολύ πιο χρονοβόρα καθώς απαιτεί πολύ περισσότερους κόμβους. Αυτό το κάνει ιδιαίτερα χρήσιμο για το πρόβλημα της βελτιστοποίησης όπου ο υπολογισμός των τάσεων γίνεται πολλές φορές.

## 8.6 Βελτιστοποίηση

Σε αυτό το κεφάλαιο περιγράφεται η μέθοδος για την βελτιστοποίηση των δίσκων. Για αυτό το λόγο αναπτύσσεται συνάρτηση υπολογισμού του βάρους του δίσκου με είσοδο την γεωμετρία του. Στη συνέχεια δημιουργείται ένα experiment στο PROOSIS όπου βελτιστοποιούνται οι δίσκοι των τριών πρώτων βαθμίδων του HPC NASA's/GE E3. Κάθε δίσκος βελτιστοποιείται κατά τρεις διαφορετικές προσεγγίσεις :Lolis [9], Gasturb [5], Armand [1]. Ενώ η αντικειμενική συνάρτηση και τα τασικά κριτήρια θεωρούνται κοινά, κάθε περίπτωση επιβάλλει τις δικές της μεταβλητές σχεδιασμού, περιορισμούς και συσχετίσεις μεταξύ μεταβλητών. Οι διαστάσεις του δίσκου που δεν είναι μεταβλητές σχεδιασμού ή δεν συσχετίζονται με άλλες παραμένουν ίσες με την αρχική τιμή τους. Η μέθοδος Simplex των Nelder Mead χρησιμοποιείται για την βελτιστοποίηση.

Η εξίσωση υπολογισμού της μάζας ενός δίσκου είναι η [1]:

$$M = 2\pi\rho \sum_{j=1}^{j=5} [\frac{m_j}{3}(r_{j+1}^3 - r_j^3) + \frac{n_j}{2}(r_{j+1}^2 - r_j^2)]$$

Ενας δίσκος τύπου web χωρίζεται σε πέντε περιοχές όπως φαίνεται στην Εικόνα 4. Σε καθεμία από αυτές ισχύει

$$t = m \cdot r + n$$

Επομένως οι συντελεστές που χρησιμοποιούνται για τον υπολογισμό του βάρους βρίσκονται από τις σχέσεις:

$$m_j = \frac{t_{j+1} - t_j}{r_{j+1} - r_j}$$

$$n_j = t_j - \frac{t_{j+1} - t_j}{r_{j+1} - r_j} r_j$$

For j=1,...,5

Για την μελέτη της βελτιστοποίησης θεωρούμε ότι για όλους τους τύπους δίσκου, όλα τα σημεία που ορίζουν τη γεωμετρία ενώνονται με ευθείες, επομένως η εξίσωση υπολογισμού του βάρους εφαρμόζεται αυτούσια σε όλες τις βαθμίδες.

Οι μεταβλητές που πρέπει να μένουν σταθερές είναι εκείνες που σχετίζονται με τη ροή του εργαζόμενου μέσου, δηλαδή οι  $r_6$  και  $t_6$ . Το πάχος στο rim είναι ίσο με την αξονική συνιστώσα της χορδής του περυγίου και η ακτίνα στο rim είναι ίσο με την ακτίνα ποδός της αεροτομής μείον το ύψος της ρίζας του περυγίου.

$$t_6 = c_{bl,ax}$$

$$r_6 = r_{airfoil\ hub} - h_{blade\ root}$$

Τα βασικά κριτήρια για την μηχανική αντοχή του δίσκου απαιτούν η μέση περιφερειακή τάση υπολογισμένη στο 120% των στροφών να είναι μικρότερη ή ίση με το 0.9 του ορίου μέγιστης αντοχής σε εφελκυσμό επιλεγμένο στην μέση θερμοκρασία δίσκου. Επιπλέον, επιβάλλουν η μέγιστη τάση von Mises να είναι μικρότερη ή ίση του ορίου διαρροής στην μέγιστη θερμοκρασία δίσκου διαιρεμένο με τον συντελεστή ασφαλείας 1.1

$$\sigma_{\theta,avg\_120} \leq 0.9\sigma_{UTS,at\ avg T} \Rightarrow RBM_{120} = \frac{\sigma_{\theta,avg\_120}}{0.9\sigma_{UTS}} \leq 1$$

$$\sigma_{vonMises,max} \leq \frac{\sigma_{Y,min}}{1.1} \Rightarrow RDM = \frac{\sigma_{vonMises,max}}{\frac{\sigma_y}{1.1}} \leq 1$$

Για να καλυφθεί η περίπτωση στην οποία κάποιες τάσεις είναι αρνητικές η μέση περιφερειακή τάση υπολογίζεται από τον τύπο:

$$\sigma_{\theta,avg} = \sqrt{\frac{1}{N} \sum_{i=1}^N \sigma_{\theta i}^2}$$

Όπου N το πλήθος των κόμβων.

Στα προβλήματα μηχανικής αντοχής η μείωση του βάρους είναι ισοδύναμη με την αύξηση των τάσεων. Επομένως, η αντικειμενική συνάρτηση επιλέγεται με τρόπο που η ελαχιστοποίηση της οδηγεί στην μεγιστοποίηση των τάσεων. Εφόσον η μέθοδος Simplex δεν απαιτεί τον υπολογισμό παραγώγων και διαχειρίζεται και ασυνεχείς συναρτήσεις η αντικειμενική συνάρτηση επιλέγεται ως:

$$F = \frac{1}{2} (\max[RDM, RBM] - 1)^2$$

Οι περιορισμοί που επιβάλλονται σε όλες τις περιπτώσεις είναι το βάρος να μην είναι αρνητικό και η μικρότερη ακτίνα του δίσκου να είναι μεγαλύτερη από 1.1 φορές την μέγιστη ακτίνα άξονα

$$M > 0$$

$$r_1 > 1.1 r_{shaft,max}$$

### 8.6.1 Βελτιστοποίηση 1<sup>ης</sup> βαθμίδας HPC E3

Ο δίσκος είναι τύπου ring. Λόγω της απλότητας του προβλήματος όλες οι περιπτώσεις βελτιστοποίησης είναι ίδιες. Η γεωμετρία περιγράφεται από την εσωτερική και εξωτερική ακτίνα και το πάχος δίσκου. Εφόσον η εξωτερική ακτίνα και το πάχος είναι προκαθορισμένα η μοναδική μεταβλητή σχεδιασμού είναι η:  $r_1$

Ισχύουν οι παρακάτω συσχετίσεις:

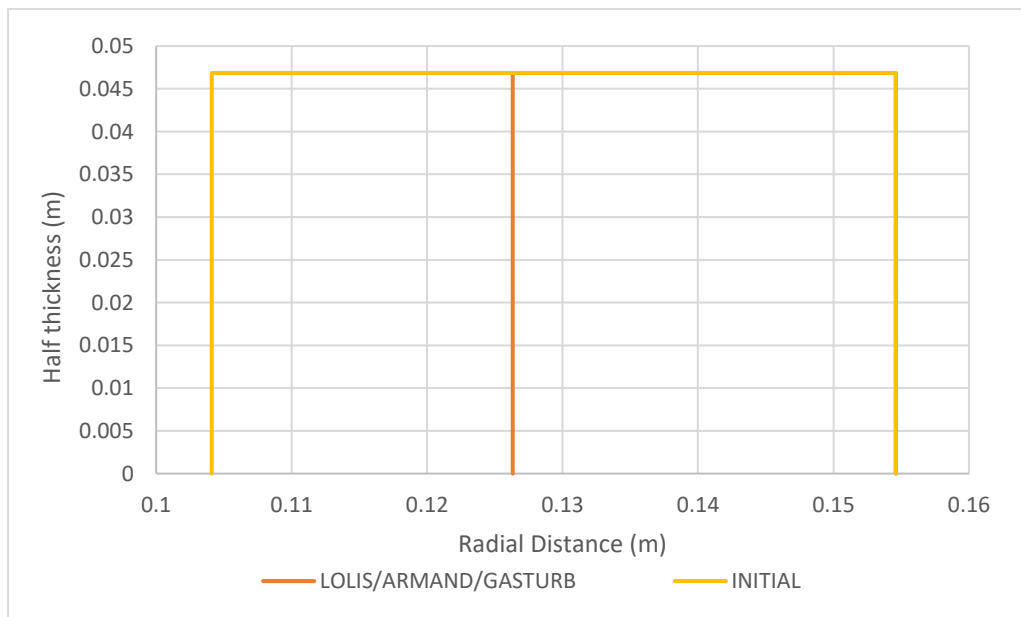
$$t_1 = t_2 = t_3 = t_4 = t_5 = t_6 = c_{bl,ax}$$

$$r_i = r_1 + (i - 1) \cdot \frac{r_6 - r_1}{5} \text{ for } i = 2, \dots, 5$$

Τα αποτελέσματα φαίνονται στον Πίνακα 6:

Μάζες		
Αρχική μάζα (kg)	Βέλτιστη μάζα (kg)	Διαφορά (%)
16.806	10.218	-39.2
Αρχική γεωμετρία		
	Bore	Rim
r(m)	0.1041	0.1546
t(m)	0.0937	0.0937
Τελική γεωμετρία		
	Bore	Rim
r(m)	0.1263	0.1546
t(m)	0.0937	0.0937
Λόγοι τάσεων		
	Initial	Optimum
RBM_120	0.630805	1
RDM	0.596673	0.862939

Πίνακας 6: Αποτελέσματα βελτιστοποίησης 1<sup>ης</sup> βαθμίδας του HPC E3



Εικόνα 20: Σύγκριση μεταξύ αρχικής και τελικής γεωμετρίας δίσκου της 1<sup>ης</sup> βαθμίδας του HPC E3.

### 8.6.2 Βελτιστοποίηση 2<sup>ης</sup> βαθμίδας HPC E3

Ο τύπος δίσκου είναι hyperbolic. Οι σταθερές μεταβλητές και οι κοινές συσχετίσεις μεταξύ μεταβλητών είναι:

$$r_6 = r_{rim}$$

$$t_6 = t_{rim}$$

$$t_5 = t_6$$

$$t_1 = t_2$$

Κατά Lolis:

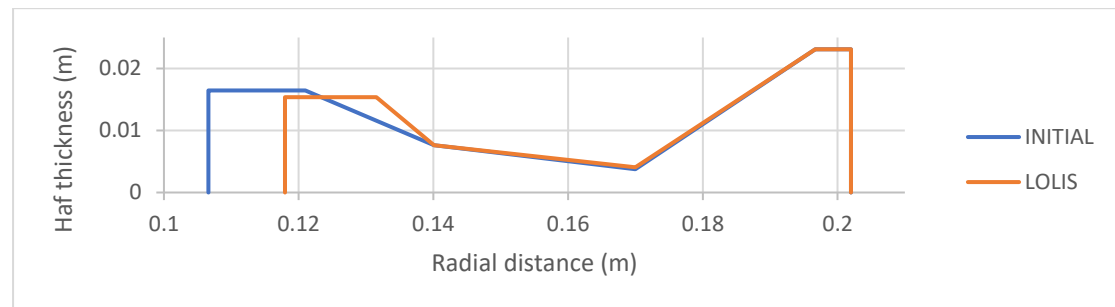
Επιλέγονται ως μεταβλητές σχεδιασμού οι:  $r_1, r_2, t_2, t_4$

Και επιβάλλονται οι παρακάτω γεωμετρικοί περιορισμοί

$$r_2 \geq 1.1 \cdot r_1$$

$$r_4 \geq 1.1 \cdot r_3$$

$$1.5 \cdot t_4 \leq t_2 \leq 2 \cdot t_6$$



Εικόνα 21: Σύγκριση μεταξύ αρχικής και τελικής γεωμετρίας δίσκου της 2<sup>ης</sup> βαθμίδας του HPC E3 για βελτιστοποίηση κατά Lolis

Κατά Gasturb:

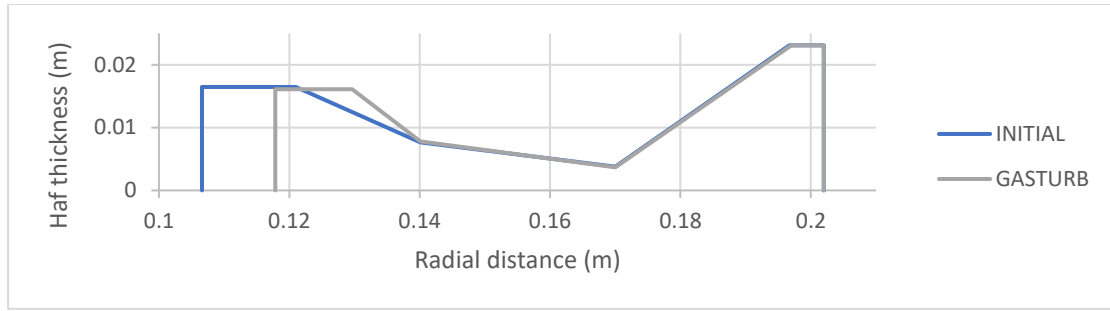
Επιλέγονται ως μεταβλητές σχεδιασμού οι :  $r_1, r_2, r_5, t_1, t_3, t_4$

Οι γεωμετρικοί περιορισμοί είναι:

$$0.1 \leq \frac{r_6 - r_5}{t_6} \leq 1$$

$$0.15 \leq \frac{t_3}{t_6} \leq 1$$

$$0.2 \leq \frac{r_2 - r_1}{t_6} \leq 1$$



Εικόνα 22: Σύγκριση μεταξύ αρχικής και τελικής γεωμετρίας δίσκου της 2<sup>ης</sup> βαθμίδας του HPC E3 για βελτιστοποίηση κατά Gasturb

### Κατά Armand:

Μεταβλητές σχεδιασμού :  $r_1, r_2, r_3, r_4, t_1, t_3, t_4$

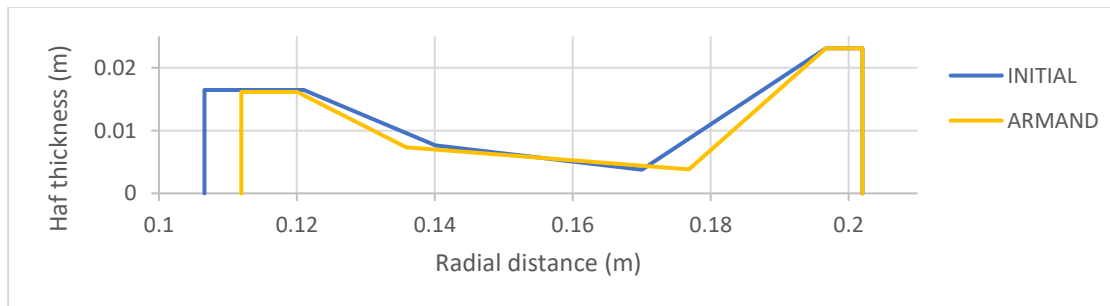
Γεωμετρικοί περιορισμοί:

$$r_2 - r_1 > 0$$

$$r_3 - r_2 > 0$$

$$r_4 - r_3 > 0$$

$$r_5 - r_4 > 0$$



Εικόνα 23: Σύγκριση μεταξύ αρχικής και τελικής γεωμετρίας δίσκου της 2<sup>ης</sup> βαθμίδας του HPC E3 για βελτιστοποίηση κατά Armand.

Βαθμίδα 2					Αρχικό βάρος (kg) : 9.695				
Αποτελέσματα βάρους									
Προσέγγιση			Βέλτιστο βάρος (kg)				Διαφορές(%)		
Lolis			8.815				-9.08		
Gasturb			8.738				-9.87		
Armand			8.289				-14.5		
Γεωμετρία									
Αρχική			Lolis		Gasturb		Armand		
	r(m)	t(m)	r(m)	t(m)	r(m)	t(m)	r(m)	t(m)	
1	0.1066	0.0329	0.1180	0.0307	0.1179	0.0322	0.1119	0.0323	
2	0.1210	0.0329	0.1316	0.0307	0.1296	0.0322	0.1200	0.0323	
3	0.1401	0.0153	0.1401	0.0153	0.1401	0.0156	0.1359	0.0146	
4	0.1700	0.0075	0.1700	0.0082	0.1700	0.0073	0.1768	0.0076	
5	0.1967	0.0462	0.1967	0.0462	0.1970	0.0462	0.1967	0.0462	
6	0.202	0.0462	0.2020	0.0462	0.2020	0.0462	0.2020	0.0462	
Λόγοι τάσεων στο βέλτιστο									
		Lolis			Gasturb		Armand		
RBM_120		1			1		1		
RDM		0.9364			0.9304		0.9372		

Πίνακας 7: Αποτελέσματα βελτιστοποίησης δεύτερης βαθμίδας.

### 8.6.3 Βελτιστοποίηση 3<sup>ης</sup> βαθμίδας HPC E3

Ο τύπος δίσκου είναι web, επομένως ισχύουν τα παρακάτω

$$r_6 = r_{rim}$$

$$t_6 = t_{rim}$$

$$t_5 = t_6$$

$$t_1 = t_2$$

$$t_3 = t_4$$

Κατά Lolis:

Μεταβλητές σχεδιασμού:  $r_1, r_2, t_1, t_3$

Συσχετίσεις μεταβλητών:

$$r_3 = r_2 + \frac{t_2 - t_3}{2 \tan\left(\frac{\pi}{5}\right)}$$

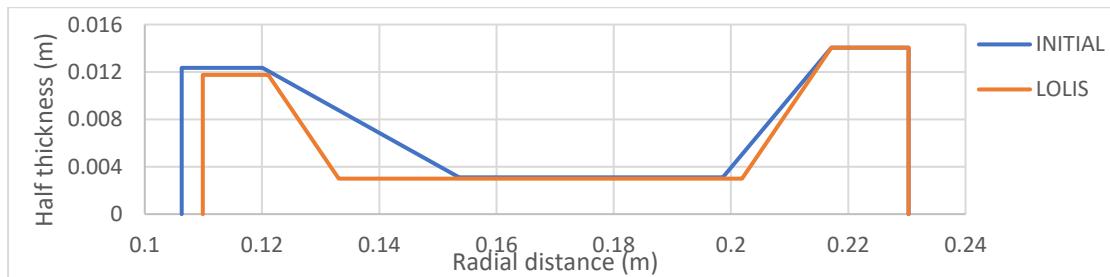
$$r_4 = r_5 - \frac{t_5 - t_4}{2 \tan\left(\frac{\pi}{5}\right)}$$

Γεωμετρικοί περιορισμοί:

$$r_2 \geq 1.1 \cdot r_1$$

$$r_4 \geq 1.1 \cdot r_3$$

$$1.5 \cdot t_4 \leq t_2 \leq 2 \cdot t_6$$



Εικόνα 24: Σύγκριση μεταξύ αρχικής και τελικής γεωμετρίας δίσκου της 3ης βαθμίδας του HPC E3 για βελτιστοποίηση κατά Lolis.

Κατά Gasturb:

Μεταβλητές σχεδιασμού :  $r_1, r_2, r_5, t_1, t_3$

Συσχετίσεις:

$$r_3 = r_2 + \frac{t_2 - t_3}{2 \tan\left(\frac{\pi}{6}\right)}$$

$$r_4 = r_5 - \frac{t_5 - t_4}{2 \tan\left(\frac{\pi}{3}\right)}$$

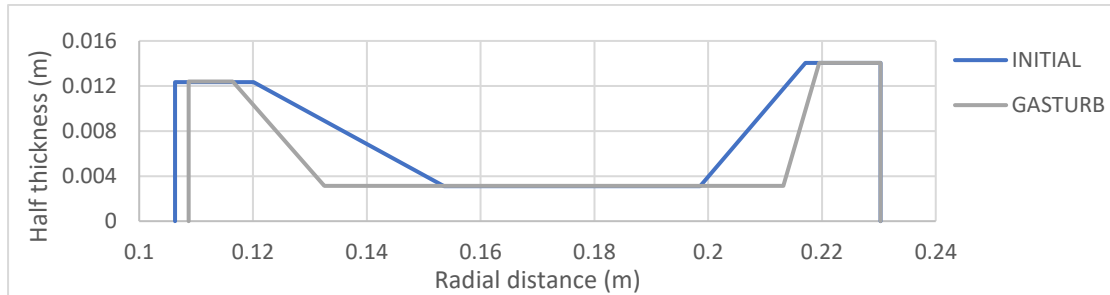


Γεωμετρικοί περιορισμοί:

$$0.1 \leq \frac{r_6 - r_5}{t_6} \leq 1$$

$$0.15 \leq \frac{t_3}{t_6} \leq 1$$

$$0.2 \leq \frac{r_2 - r_1}{t_6} \leq 1$$



Εικόνα 25: Σύγκριση μεταξύ αρχικής και τελικής γεωμετρίας δίσκου της 3<sup>ης</sup> βαθμίδας του HPC E3 για βελτιστοποίηση κατά Gasturb.

Κατά Armand:

Μεταβλητές σχεδιασμού:  $r_1, r_2, r_3, r_4, t_1, t_3$

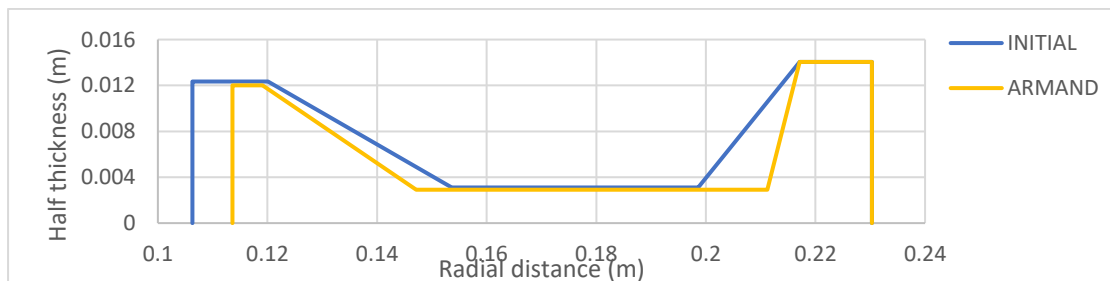
Γεωμετρικοί περιορισμοί:

$$r_2 - r_1 > 0$$

$$r_3 - r_2 > 0$$

$$r_4 - r_3 > 0$$

$$r_5 - r_4 > 0$$



Εικόνα 26: Σύγκριση μεταξύ αρχικής και τελικής γεωμετρίας δίσκου της 3<sup>ης</sup> βαθμίδας του HPC E3 για βελτιστοποίηση κατά Armand.

Βαθμίδα 3					Αρχικό βάρος (kg) : 8.527			
Αποτελέσματα βάρους								
Προσέγγιση			Βέλτιστο βάρος (kg)				Διαφορές (%)	
Lolis			7.222				-15.3	
Gasturb			6.429				-24.6	
Armand			6.72				-21.2	
Γεωμετρία								
Αρχική			Lolis		Gasturb		Armand	
	r(m)	t(m)	r(m)	t(m)	r(m)	t(m)	r(m)	t(m)
1	0.1063	0.0247	0.1099	0.0235	0.1087	0.0248	0.1136	0.0240
2	0.1201	0.0247	0.1211	0.0235	0.1165	0.0248	0.1191	0.0240
3	0.1536	0.0062	0.1331	0.0060	0.1325	0.0062	0.1471	0.0058
4	0.1986	0.0062	0.2019	0.0060	0.2132	0.0062	0.2112	0.0058
5	0.2171	0.0281	0.2171	0.0281	0.2195	0.0281	0.2171	0.0281
6	0.2303	0.0281	0.2303	0.0281	0.2303	0.0281	0.2303	0.0281
Λόγοι τάσεων στο βέλτιστο								
		Lolis			Gasturb		Armand	
RBM_120		1			1		1	
RDM		0.9643			0.9610		0.9534	

Πίνακας 8: Αποτελέσματα βελτιστοποίησης 3<sup>ης</sup> βαθμίδας του HPC E3

Τέλος σημειώνεται ότι έτρεξε μια περίπτωση βελτιστοποίησης με το λογισμικό Gasturb Details 5 και με τον κώδικα που αναπτύχθηκε στο PROOSIS για να πιστοποιηθούν τα αποτελέσματα. Πράγματι η βέλτιστη λύση που προέκυπτε ήταν κοντινή.

## 8.7 Ανακεφαλαίωση ,συμπεράσματα και προτάσεις

Σε αυτή τη διπλωματική εργασία, αφού έγινε εκτενής μελετή των βιβλιογραφικών πηγών, αναπτύχθηκαν εργαλεία στο PROOSIS για το σχεδιασμό και τη βελτιστοποίηση δίσκων θερμικών στροβιλομηχανών. Δύο βασικές συναρτήσεις χρησιμοποιούνται: η συνάρτηση υπολογισμού του θερμοκρασιακού προφίλ και η συνάρτηση υπολογισμού των τάσεων που έχει ως είσοδο τα αποτελέσματα της θερμικής ανάλυσης. Τα αποτελέσματα των δύο αυτών συναρτήσεων πιστοποιήθηκαν μέσω της σύγκρισης τους με τα αποτελέσματα που προκύπτουν από το Solidworks. Έπειτα, οι συναρτήσεις αυτές χρησιμοποιήθηκαν για την βελτιστοποίηση. Η μείωση του βάρους επιτεύχθηκε με την μεγιστοποίηση των τάσεων. Ως αρχικές γεωμετρικές χρησιμοποιήθηκαν οι τρεις πρώτοι δίσκοι του HPC NASA/GE E3. Η Simplex των Nelder-Mead χρησιμοποιήθηκε για την ανανέωση της γεωμετρίας του δίσκου και σε κάθε επανάληψη οι συναρτήσεις υπολογισμού της θερμοκρασίας και των τάσεων καλούνταν για να επαναυπολογιστεί η τιμή της αντικειμενικής συνάρτησης. Εξετάστηκαν τρεις περιπτώσεις βελτιστοποίησης, κάθε μία με μεταβλητές και περιορισμούς κατά Lolis, Gasturb και Armand.

Συμπεραίνεται ότι η μονοδιάστατη μοντελοποίηση της κατανομής των θερμοκρασιών και των τάσεων δίνει πολύ κοντινά αποτελέσματα με την μέθοδο των πεπερασμένων στοιχείων με πολύ λιγότερους κόμβους και σε πολύ λιγότερο χρόνο. Αυτό κάνει την βελτιστοποίηση ταχύτερη. Επιπλέον, αποδεικνύεται ότι η μεγιστοποίηση των τάσεων με χρήση της Simplex μπορεί να οδηγήσει σε ελαφρύτερη γεωμετρία ακόμη και με 7 μεταβλητές σχεδιασμού. Τέλος, η εγγύτητα της βέλτιστης λύσης του PROOSIS με τη λύση που δίνεται από το «Gasturb Details 5» πιστοποιεί την αποτελεσματικότητα του προγράμματος.

Τα χρησιμοποιούμενα εργαλεία είναι ευέλικτα καθώς πολλές επιλογές μπορούν να καθοριστούν από την χρήση και να εισέλθουν σαν είσοδο στις συναρτήσεις. Αυτό τα κάνει κατάλληλα για ενσωμάτωση σε μεγαλύτερα προβλήματα όπως είναι ο σχεδιασμός μιας ολόκληρης μηχανής. Έπειτα από την ανάλυση της ροής η προκύπτουσα γεωμετρία πτερυγίου μπορεί να χρησιμοποιηθεί για να αποκτηθεί μια βελτιστοποιημένη γεωμετρία δίσκου που θα στηρίζει τα πτερύγια. Η ίδια διαδικασία μπορεί να εφαρμοστεί διαδοχικά σε κάθε βαθμίδα ώστε να σχεδιαστούν οι δίσκοι ολόκληρου του κινητήρα. Εναλλακτικά, η μέθοδος βελτιστοποίησης που αναπτύχθηκε μπορεί να συνδυαστεί με άλλες μεθόδους όπως είναι οι γενετικοί αλγόριθμοι.